Université de Montréal

Vector Flow Mapping Using Plane-Wave Ultrasound Imaging

par
Sarah Dort

Institut de génie biomédical
Faculté de Médecine

Mémoire présenté à la Faculté des études supérieures
en vue de l'obtention du grade de Maître ès sciences appliquées (M.Sc.A)
en génie biomédical
option : Instrumentation et imagerie biomédicale

December 31, 2013

Université de Montréal
Faculté des études supérieures et postdoctorales

Ce mémoire intitulé :

Vector Flow Mapping Using Plane-Wave Ultrasound Imaging

Présenté par :
Sarah Dort

a été évalué par un jury composé des personnes suivantes :

Frédéric Leblond, Ph.D., Ing., président-rapporteur
Damien Garcia, Ph.D., Ing., directeur de recherche
Guy Cloutier, Ph.D., Ing., co-directeur
Frédéric Lesage, Ph.D., Ing., membre du jury

Résumé

Les diagnostics cliniques des maladies cardio-vasculaires sont principalement effectués à l'aide d'échographies Doppler-couleur malgré ses restrictions : mesures de vélocité dépendantes de l'angle ainsi qu'une fréquence d'images plus faible à cause de focalisation traditionnelle. Deux études, utilisant des approches différentes, adressent ces restrictions en utilisant l'imagerie à onde-plane, post-traitée avec des méthodes de délai et sommation et d'autocorrélation. L'objectif de la présente étude est de ré-implémenté ces méthodes pour analyser certains paramètres qui affecte la précision des estimations de la vélocité du flux sanguin en utilisant le Doppler vectoriel 2D.

À l'aide d'expériences in vitro sur des flux paraboliques stationnaires effectuées avec un système Verasonics, l'impact de quatre paramètres sur la précision de la cartographie a été évalué : le nombre d'inclinaisons par orientation, la longueur d'ensemble pour les images à orientation unique, le nombre de cycles par pulsation, ainsi que l'angle de l'orientation pour différents flux. Les valeurs optimales sont de 7 inclinaisons par orientation, une orientation de ±15° avec 6 cycles par pulsation. La précision de la reconstruction est comparable à l'échographie Doppler conventionnelle, tout en ayant une fréquence d'image 10 à 20 fois supérieure, permettant une meilleure caractérisation des transitions rapides qui requiert une résolution temporelle élevée.

Mots-clés : flux sanguin, onde plane, cartographie vectorielle, échographie ultrarapide

Abstract

Clinical diagnosis of cardiovascular disease is dominated by colour-Doppler ultrasound despite its limitations: angle-dependent velocity measurements and low frame-rate from conventional focusing. Two studies, varying in their approach, address these limitations using plane-wave imaging, post-processed with the delay-and-sum and autocorrelation methods. The aim of this study is to re-implement these methods, investigating some parameters which affect blood velocity estimation accuracy using 2D vector-Doppler.

Through *in vitro* experimentation on stationary parabolic flow, using a Verasonics system, four parameters were tested on mapping accuracy: number of tilts per orientation, ensemble length for single titled images, cycles per transmit pulse, and orientation angle at various flow-rates. The optimal estimates were found for 7 compounded tilts per image, oriented at ±15° with 6 cycles per pulse. Reconstruction accuracies were comparable to conventional Doppler; however, maintaining frame-rates more than 10 to 20 times faster, allowing better characterization of fast transient events requiring higher temporal resolution.

Keywords : blood flow, plane-wave, vector flow, ultrafast ultrasound

Table of Contents

List of Figures

List of Tables

List of Abbreviations

CD :	colour-Doppler
CVD :	cardiovascular disease
CW :	continuous-wave
DAS :	delay-and-sum
fps :	frames per second
IQ :	in-phase quadrature
MLA :	multi-line acquisition
NRMSE :	normalized root-mean-squared error
PRF :	pulse repetition frequency
PW :	pulse-wave
PZT :	piezo-electric
RF :	radio-frequency
SLA :	single-line acquisition
SNR :	signal-to-noise ratio
STD :	standard deviation
US :	ultrasound
VD :	vector-Doppler
1D :	one-dimensional
2D :	two-dimensional
3D :	three-dimensional

List of Symbols

A :	amplitude of receive signal
a_p :	amplitude fluctuation in filter pass-band
a_s :	amplitude in filter stop-band
A_0 :	initial amplitude of signal at emission
α :	angle of emission
β :	angle of reception
c :	speed of acoustic propagation
d :	distance between scatterers
D_{ap} :	aperture diameter
D_b :	beam width
D_f :	focal distance
D_t :	transducer diameter
$\Delta\tau$:	change in fast-time time delay
$\Delta\tau_{max}$:	maximum detectable change in fast-time time delay
δV :	change in velocity over threshold
Δz :	depth change in displacement
ξ :	attenuation coefficient
f_c :	cut-off frequency
f_d :	Doppler frequency
f_p :	frequency at start of pass-band
f_{prf} :	pulse repetition frequency
f_r :	central frequency of received signal
f_s :	sampling frequency
f_{slow} :	slow-time frequency
f_0 :	central frequency of emitted signal
$F^{\#}$:	F-number
I :	intensity of an incident wave
$I(t)$:	real in-phase signal
IQ :	in-phase quadrature signal
K :	number of pulse transmissions, i.e. ensemble length
K_L :	interval between packets
κ :	compressibility
l :	dimension of gate/window in cross-correlation
L :	number of beams acquired per multi-line acquisition

λ :	wavelength
μ_s :	mean of signal
n :	shape factor for Poiseuille flow
N :	number of tilted plane-waves per orient image
N_l :	number of lines per image
N_s :	range gate size in samples
N_0 :	start sample of window
ω_{slow} :	angular frequency of slow-time signal
Ω :	solid angle
φ :	scattering angle
ϕ_c :	constant phase component
ϕ_t :	variable phase component
$Q(t)$:	imaginary quadrature signal
r :	radius
R :	coefficient of reflection
$R(t)$:	autocorrelation function
$RF(t)$:	radio-frequency signal
r_{max} :	maximum radius
ρ :	density
s :	lag
S :	scattering power
s_{int} :	interpolated lag
σ :	differential cross-section area of scattering
σ_s :	standard deviation of signal
t :	fast-time time duration
T :	coefficient of refraction
T_{FR} :	frame-rate period
T_{prf} :	pulse repetition period
τ :	fast-time travel-time
τ_{RX} :	travel-time in reception
τ_{TX} :	travel-time in emission
θ :	beam to flow angle
θ_i :	incident angle
θ_r :	angle of reflection
θ_t :	angle of refraction
v :	velocity profile
V :	velocity of source or observer, i.e. scatterer

V_{int} :	interpolated velocity
v_{max} :	maximum velocity
V_n :	Doppler velocity projections from negatively oriented acquisition
V_p :	Doppler velocity projections from positively oriented acquisition
V_z :	axial velocity of scatterer
Vz_{max} :	maximum detectable axial velocity
Vz_{min} :	minimum detectable axial velocity
x :	lateral position
x_1' :	lateral position of a transducer element in an oriented coordinate system
x' :	lateral position in an oriented coordinate system
z :	depth in tissue, axial position
Z :	acoustic impedance
z_{max} :	maximum depth of scan
z' :	axial position in an oriented coordinate system
$*$:	complex conjugate
$*^T$:	conjugate transpose

To my parents and husband for their support.

Acknowledgements

I would like to express my gratitude to Damien Garcia for his incessant enthusiasm, resolute focus, and of course, knowledgeable direction. In addition, thank you to Guy Cloutier for his seasoned advice and candour. Your support and combined efforts to bring this project to completion have been much appreciated. I would also like to extend my courtesy to my team at RUBIC and LBUM for creating an amicable environment and providing social relief, as well as for each of their individual expertise.

Subsequently, I would like to thank Abigail Swillens and Patrick Segers from the Institute of Biomedical Technologies at the University of Ghent in Belgium. They generously welcomed me to their team and hosted me for three months. I am grateful for their kind encouragement and guidance.

Finally, I would like to acknowledge the biomedical training program MEDITIS funded by the National Sciences and Engineering Research Council of Canada. This award has provided financial support and afforded me the opportunity to take part in an international internship, form strong collaborations, and expand my competence.

Introduction

Motivation

Cardiovascular disease (CVD) is the leading cause of death worldwide and among the most prominent causes of death in Canada. The mortality rate associated with CVD has been estimated at 17.3 million people per year globally [1], 80 percent of these deaths occur in the developed world [2]; roughly 69.5 thousand of these deaths occur in Canada [3]. Furthermore, in Canada, over 1.6 million people have been reported to live with heart diseases or suffer from the effects of strokes. Nationally, CVD accounts for approximately 16.9 percent of all hospitalizations [4] and is responsible for a total economic burden of roughly 20.9 billion dollars per annum [5]. The ability to provide inexpensive screening for early detection of CVD is a propitious way to approach this dilemma, in order to decrease the mortality rate and financial burden of health care.

The major underlying cause of CVD is atherosclerotic development. Atherosclerosis is a pathological condition characterized by gradual thickening and stiffening of the inner wall of blood vessels due to the accrual of fatty deposits [1]. In progressed cases, occurrence of lesions in the vessel wall may lead to plaque development and stenosis without presenting prognostic symptoms. Vulnerable plaque rupture is contingent, which may impede flow to areas such as the brain or heart causing stroke or cardiac infarction [1]. Due to this outcome, much research has been devoted to understanding the development of atherosclerosis before such devastating manifestations occur.

There has been a recognized association between atherosclerotic development and the presence of changes in the mechanical behaviour of the vessel wall and the dynamics of blood flow. For the purposes of this work, focus is drawn to the study of hemodynamics. Hemodynamic forces play a major role in the development of vascular pathologies, such as atherosclerosis, and may also influence blood vessel mechanical properties [6]. Blood flow exhibits shear stresses, a frictional force per

unit area, on vessel walls and as such has been implicated in vascular patho-biological changes [6].

Although atherosclerotic development has a variety of risk factors such as genetic predisposition, hypertension, smoking, poor diet and sedentary lifestyle, among others [2], it has also been recognized as a geometrically susceptible disease highly correlated to areas with complex geometries containing turbulent flow patterns such as flow separations and flow reversals, as well as strongly pulsatile behaviour [6-8]. In figure I, for example, zones of bifurcation consistent with the carotid arteries are highly susceptible to atherosclerosis, which tends to affect the outer edges of the blood vessel divide where shear rates are lower due to the geometry [6, 8].

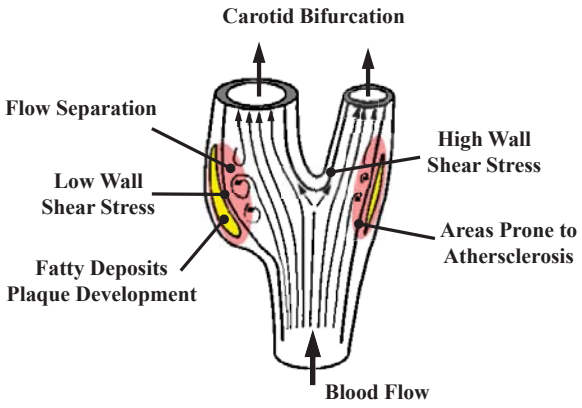

Figure I: Illustration of the carotid artery at the level of the bifurcation, demonstrating the geometric susceptibility of atherosclerotic development due to complex flow behaviour. The zones emphasized in red are liable to artherogenesis. Adapted from [6].

Methods for determining the wall shear stress exhibited by blood flow using ultrasound (US) imaging have been proposed, however they have not yet been applied in clinical routine [9, 10]. Similarly, multidimensional blood velocity estimation methods have been proposed in the context of providing early signs of abnormal flow patterns in high risk areas susceptible to atherosclerosis, but are not yet clinically accepted [11-14]. Clinical practice is still dominated by one-dimensional (1D) US flow estimations, namely colour-Doppler (CD).

CD possesses some well-known limitations; these limitations are the 1D nature of the measurements, and the frame-rate restriction. To elaborate, conventional flow velocity estimation is based on the correlation of a series of radio-frequency signals, applied along the beam direction. Therefore orthogonal components of the flow are unattainable [15]. As blood vessels have complex geometries which vary in direction, it is infeasible to align the axis of acquisition with the flow direction; thus there exists an error in the velocity measurements [15]. Quantification of the flow in CD images is simply a colour coded scheme representing the magnitude of the velocity projection in-line with the beam, often making these images difficult to interpret.

Furthermore, conventional CD imaging relies on multiple focused beams for the creation of one particular frame. The acquisition rate or time to acquire each beam depends on the speed of acoustic propagation as well as the desired depth. Indeed, this means that the frame-rate of conventional scans depends on the acquisition rate and the number of focused emissions (typically in the range of 64 to 256 beams per image) necessary to cover an adequate region of interest, in some instances, constraining the CD imaging rate to five frames per second [16]. For imaging fast flow profiles and transitory events this frame-rate is insufficient due to low temporal resolution which may result in aliasing or lack in detectability of important flow structures [17].

The ability to provide full and accurate quantification of the hemodynamics in major blood vessels, namely the carotid arteries, in a clinical context is significant. Proper quantification may help identify high risk flow patterns associated with atherosclerotic development before morbid manifestation, to mitigate the related mortality rate and health care expenditures associated with CVD.

Contribution (Objective)

Plane-imaging is of growing interest to the medical ultrasound domain, as an alternative to focused imaging, because full-image datasets are obtainable with a single pulse transmission rather than a multitude of amalgamated focused beams

(see section 3.3.3). Although plane-wave imaging suffers from reduced resolution and penetration depth, it provides a vast improvement on the temporal resolution. Recently, two configurations of plane-wave imaging have been proposed (see section 4.2) and applied to blood velocity estimation using conventional Doppler post-processing [18, 19].

The purpose of this work is to implement and compare the two existing scanning configurations of plane wave imaging, which have been proposed to address the aforementioned frame-rate limitation of CD (refer to section 3.1.2). Additionally, the vector-Doppler technique will be used to provide two-dimensional velocity maps through triangulation of overlapping planar images, which addresses the angle dependence of Doppler ultrasound (refer to section 3.1.1). More specifically, an investigation of certain parameters which affect the accuracy of the vector maps will be examined with the intention of providing insight into the optimal scanning configurations necessary for clinical implementation.

Structure

This dissertation is organized in six chapters.

Chapter 1 begins with the fundamental physics involved in medical ultrasound, particularly the interaction between acoustic waves and blood. Conventional imaging is then presented, stressing factors which affect image quality. A foundation is laid for later discourse on blood velocity estimation using ultrasound.

Chapter 2 imparts knowledge on the conventional use of ultrasound for blood flow quantification, referred to as colour-Doppler. The steps involved in blood velocity estimation and some of the inherent limitations involved in the process are given.

Chapter 3 acknowledges two major shortcomings of colour-Doppler ultrasound: one-dimensional nature of the blood velocity estimation, and limited frame-rate due to the focused beam approach. A review of literature is then devoted to overcoming said limitations. Finally, the objectives of this project are provided.

Chapter 4 provides details concerning the materials and methods employed to meet the objectives of this dissertation. Globally, this includes descriptions of the *in vitro* setup, acquisition protocol and post-processing procedure for one-dimensional blood velocity estimation and vector flow mapping.

Chapter 5 allows visualization of the results obtained using the proposed methods and the velocity vector maps obtained. This chapter is divided into four main sections representing the four main parameters investigated.

Chapter 6, the final chapter, provides a brief discussion to recapitulate the discoveries made during this project and provide and explanation for trends seen in the data.

Chapter 1 : Overview of Medical Ultrasound

In this chapter, a brief overview of medical ultrasound (US) is provided. A description of acoustic wave propagation and wave-tissue interaction is made. As this project involves quantification of blood flow using US, special attention is paid to the interaction between US waves and blood. The rudiments of conventional imaging are provided, including the aspects involved in the acquisition of US data for conventional imaging and some factors which affect image quality.

1.1 Basic Principles of Ultrasound

Typically, a longitudinal pressure wave is emitted into the tissue medium or region of interest by an acoustic source, whereby the wave begins to propagate [15]. This propagation creates an oscillating motion of the tissue particles parallel to the wave direction, as shown in figure 1.1.

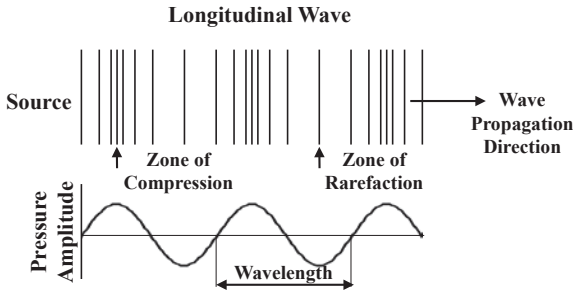

Figure 1.1: Zones of compression and rarefaction created in a medium due to the propagation of a longitudinal acoustic wave. Based on [20].

Note that as the wave passes through the medium, zones of compression and rarefaction are created which correspond to the peaks and troughs of the pressure wave. Alike zones are separated by a wavelength. The speed of acoustic propagation, c, of the longitudinal wave is dependent on the density, ρ, and compressibility, κ, of the medium as follows, $c = \sqrt{1/\rho\kappa}$ [21]. By observing this expression, it is clear that less compressible mediums have higher propagation speeds. Human soft tissue has an acoustic speed, adapted by the majority of US

devices, of roughly 1540 $m \cdot s^{-1}$ [16]. Blood has a density and compressibility of roughly 1055 $kg \cdot m^{-3}$ and 0.38 GPa^{-1}, respectively, resulting in an acoustic propagation speed of about 1570 $m \cdot s^{-1}$ [16]. Care must be taken to avoid regions which differ significantly from the generalized 1540 $m \cdot s^{-1}$ as image degradation is a consequence.

Naturally, as the US wave propagates, some of the acoustic energy scatters within the medium in response to changes in acoustic impedance, i.e. density and/or compressibility of the medium. This scattering is essential to imaging because it is the backscattered signals received from the scattering which yield the amplitude, phase and frequency information required to provide blood velocity estimates [15].

1.1.1 Acoustic Impedance

Acoustic impedance is the resistance of a material to the passage of an incident pressure wave. The degree of impedance, *Z*, of an object or medium is determined by the product of the speed of acoustic propagation, *c*, and the density of the medium, ρ, given by, $Z = c \cdot \rho$ [16]. The scattering involved at the interface between two mediums or objects of distinct acoustic impedance is a function of the size of the scattering object in comparison to the wavelength of the incident wave, as well as the difference in acoustic impedance across the boundary [22].

1.1.1.a Scattering

As previously stated, the size of the impeding object in the medium compared with the incident wavelength affects scattering. There are three major modes of scattering: specular reflection, diffusive scattering and diffractive scattering. These scattering types are discussed here.

Specular reflection, occurs when the US wavelength is smaller than the dimensions of the object in the medium. Examples of such scattering in relation to this work, can be seen in the case of blood vessel walls, more significantly in calcified vasculature with plaque deposition [22]. Specular reflection, demonstrated in figure 1.2A, results in part of the incident beam being reflected

and another part which is refracted at a boundary of differing acoustic impedance. Equations 1.1 and 1.2 depict the reflection (R) and refraction (T) coefficients [22],

$$R = \frac{Z_t \cos\theta_i - Z_i \cos\theta_t}{Z_t \cos\theta_i + Z_i \cos\theta_t} \qquad 1.1$$

$$T = \frac{2Z_t \cos\theta_i}{Z_t \cos\theta_i + Z_i \cos\theta_t} \qquad 1.2$$

where, Z_i and Z_t are the impedance measures of the tissue medium before (incident to) and after (refracted by) the tissue boundary, θ_i is the angle at which the incident wave approaches the tissue boundary, and θ_t and θ_r are the angles at which the refracted and reflected waves departs from the boundary, respectively.

Furthermore, the refracted portion of the beam deviates as it crosses the boundary [21]. In the case of colour-Doppler (CD) flow measurements (see chapter 2), this distortion contributes to a velocity bias. This velocity bias can be, for the most part, dealt with using clutter filtering (see section 2.3.4) [15].

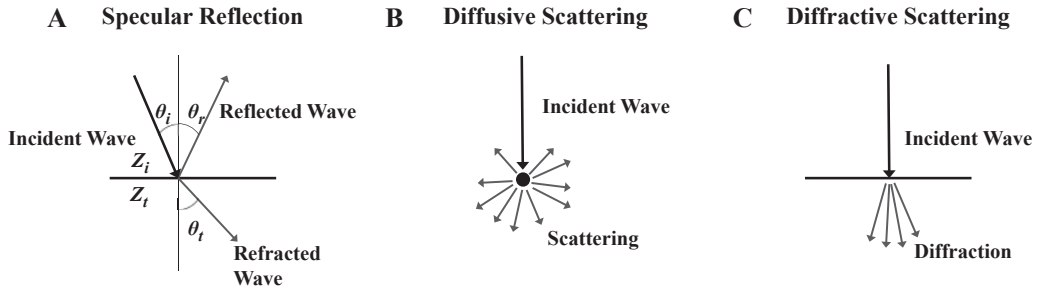

Figure 1.2: Illustration of the three major modes of scattering in tissue: A. Specular reflection, B. diffusive scattering, and C. diffractive scattering. Modified from [23].

Diffusive scattering is a result of emitting US wavelengths which are longer than the dimensions of the inhomogeneity in the tissue. The reflection then spreads out in all directions as shown in figure 1.2B, for which a portion of the signal returns to the transducer [22]. A common way to characterize the intensity of the returning backscattered signal from a contributing scatterer is the radiated intensity or power, S. The radiated power is the product of the incident wave intensity, I, and the differential cross-sectional area of scattering, σ, shown here, $S(\Omega) = I \cdot \sigma(\Omega)$ [22]. The symbol Ω indicates a solid angle measured in steradian, a three-

dimensional (3D) analogy to the radian. The cross-sectional area is shown in figure 1.3A. At 180 degrees from incident, the cross-sectional area which returns to the transducer, and indicates the strength of the signal, is demonstrated [22].

Although blood scattering is described in more detail below, it is worth mentioning here that the scattering power produced from blood is not uniform for all scattering angles, φ. Indeed, as shown in figure 1.3B, the scattering power is maximal for scattering at φ equal to 180 degrees, in other words the signal returning to the transducer, and minimal at zero degrees, for the signal which continues further into the medium [22].

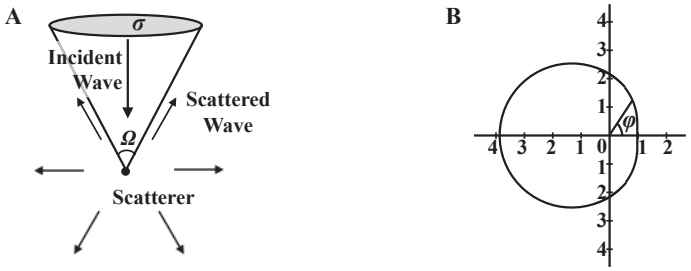

Figure 1.3: Strength of a diffusively scattered signal. A. Scattering strength represented by the differential cross-section, σ, over a solid angle, Ω. Adapted from [21]. B. The polar diagram depicting the normalized scattering power in decibels (dB) of blood scattering with respect to scattering angle, φ. Adapted from [22].

Additionally, diffusive scattering is most prominent in medical images. Soft tissue can be generalized as a collection of densely organized point scatterers with a random distribution [22].

Finally, diffractive scattering occurs when the scattering object is of a size roughly equal to the wavelength. For the most part, the result of this case is the continuation of the US in a continuous direction while fanning out [21]. Diffractive scattering is shown in figure 1.2C.

1.1.1.b Blood Scattering

Blood is comprised of fluid called plasma in which red blood cells, white blood cells and platelets are suspended with a blood volume composition of 45, 0.8 and 0.2 percent, respectively [16]. Due to these proportions the effect of scattering by the platelets and white blood cells can be neglected. Red blood cells are described

as biconcave discs with a thickness and diameter of roughly 2 μm and 7 μm [16]. Blood is assumed to cause diffusive scattering when imaging in the normal diagnostic range of frequencies because the cells are of a dimension smaller than the characteristic wavelength [16]. For example, in this work, a 5 MHz transducer is used which, in soft tissue, has a wavelength of roughly 308 μm.

Blood scattering has been dubbed *Rayleigh scattering* [16]. Rayleigh scattering manifests as the interference between the wavelets of multiple point scatterers. One characteristic of Rayleigh scattering is that the returning signal intensity depends on the central frequency to the fourth power [16]. Using higher central frequencies for an emitted pulse will provide significantly stronger reflections from blood compared with the tissue.

Additionally, received signals from blood scattering have been generalized as Gaussian random processes. This is because the signals are composed of many Gaussian modulated echoes which are assumed to arise from many independent blood cells [16]. Contrarily, it should be recognized that the locations of the red blood cells are correlated as the distance of separation is quite small. In slow moving flow conditions with low shear rates, blood tends to organize in multi-cellular conglomerated formations called *rouleaux* [16]. Rouleaux are larger formations and result in increased echo strength. Similarly, turbulent flow has been associated with density variations in the blood as the red blood cells are pulled away from one another. Thus, turbulence also affects the signal by increasing backscattering [16].

1.1.2 Attenuation

Energy loss is inherent in acoustic wave propagation through a heterogeneous medium. Two major determinants can be held accountable for attenuation, namely scattering and absorption, among other minor factors [21]. Scattering encompasses a loss of energy from a wave due to scattering, prefatorily described as the deviation of a wave from the original direction of transmission. Absorption is the

conversion of motion energy of the acoustic wave into thermal energy, most notably due to a relaxation process of insonified tissue [21].

The acoustic energy loss in the received signal is revealed through attenuation as a function of distance travelled or depth in the medium as well as emitted central frequency. The relationship $A(z, f_0) = A_0 e^{-\alpha f_0 z}$ describes the characteristic attenuation in tissues; where, A is the amplitude or intensity of the propagating wave, z and f_0 are the depth travelled and emitted central frequency, A_0 is the initial intensity of the wave at emission, and α represents the attenuation coefficient [21]. Here it is clear that there is an exponential decrease in the initial signal amplitude as a wave propagates further into the tissue. The attenuation coefficient of soft tissue and blood is about 0.7 $dB \cdot MHz^{-1} \cdot cm^{-1}$ and 0.2 $dB \cdot MHz^{-1} \cdot cm^{-1}$, respectively [16]. Attenuation is rectified by applying amplification to the receive signal called time gain compensation [22].

However, as a consequence of the frequency dependent nature of attenuation, higher frequency components of the backscattered signal will be subject to more attenuation than the lower frequency components [15]. In this way, the returned signal will have a lower center frequency than the emitted pulse and can effectuate an under-estimation bias when calculating Doppler velocities which worsens with increasing depth, frequency, and emitted bandwidth [15]. Typically, acquisitions of deep anatomy use central frequencies in the range of 1 to 3 MHz and more superficial structures are illuminated with 5 to 10 MHz, to avoid the frequency dependent effects of attenuation [16].

1.2 Rudiments of Conventional Imaging

Conventional acquisitions start from a transducer which emits a pressure wave into a targeted tissue medium using a pulse-echo technique. The characteristics of the transducer structure and the beam it creates have an effect on the resulting images, whether for visualization of the anatomy or velocity information. These characteristics are described here with reference to their effect on image quality.

1.2.1 Ultrasound Transducer

The purpose of an US transducer is to emit and receive acoustic waves. The principle component is then the piezo-electric (PZT) elements contained within the transducer housing. PZT materials have the capacity to act as a bridge between electrical and mechanical energy [24]. By imposing a source of vibration on a PZT material the result will be the production of an electrical signal, also known as the direct effect employed during US reception. The reverse effect is achieved by applying a transient electrical signal to elicit a vibration or ultrasonic pressure wave employed during transmission [21].

A disadvantage of PZT material for this application is that its acoustic impedance differs greatly from that of soft tissue. Consequently, the majority of the transmitted energy is immediately reflected back into the transducer at the transducer-tissue interface [15]. To avoid strong echoes within the transducer, called ringing, a backing layer is placed behind the element which dampens or eliminates the reverberation by absorbing the prematurely reflected waves. Conjointly, the energy transmitted into the tissue is constrained; hence the placement of a matching layer which offers an intermediate zone of impedance to help deal with reverberation and gradually ease the wave transmission [15, 24].

Although a transducer may emit a signal at a particular central frequency, due to the aforementioned housing design considerations, it is a range of frequencies which leaves the transducer to enter the tissue. This frequency range is called the transducer bandwidth [23]. The transducer bandwidth has important implications for imaging as it affects the resolution (refer to section 1.2.3.b). For example, one way to improve the image resolution is to transmit shorter pulses, meaning larger pulse bandwidths; however, the pulse bandwidth is constrained to the limits of the transducer bandwidth [23].

1.2.1.a Transducer Configuration

As previously mentioned, each transducer holds multiple elements. Commonly used terminology to describe the configuration of these elements is provided here

and depicted in figure 1.4. The PZT elements are separated by a distance referred to as the *kerf* and the distance between element centers is referred to as *pitch*. These dimensions are significant in this work, as they provide the lateral distances necessary to calculate the delays required for beam-forming (see section 1.2.1.b) [21].

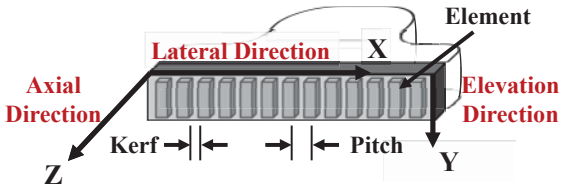

Figure 1.4: Orientation and configuration of a transducer array. Adapted from [21] and [25]

To define the orientation of the two-dimensional (2D) imaging plane with respect to the transducer the terms *axial* and *lateral* are used. The axial direction is in-line with the beam direction and orthogonal to the surface of the transducer. The lateral direction runs along the length of the probe over all elements, perpendicular to the beam direction. Lastly, the *elevation* direction identifies the width of the probe; orthogonal to the image plane [21].

The two most common types of multi-element probes are the linear array and phased array transducers. Both types of transducers excite the medium with multiple focused beams corresponding to scan-lines of echo data. The main difference between the two types is the active region excited to produce each beam [15], shown in figure 1.5.

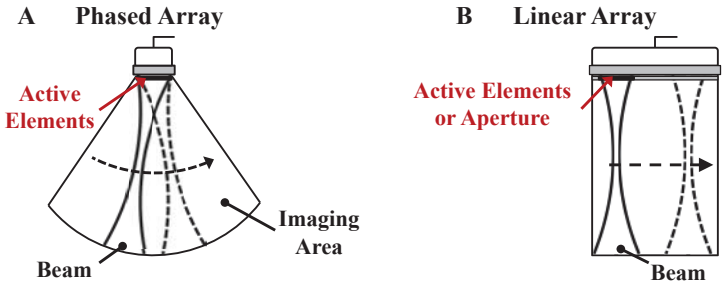

Figure 1.5: Conventional scanning method of two common transducer formats; A. the phased array transducer and B. the linear array transducer. The dashed arrows in both panels show the course of scan. Adapted from [26]

All phased array elements are activated for each beam and subsequent beams are emitted using steering to cover the region of interest which results in a sector scan. Contrarily, linear array elements are stimulated in groups called an aperture; subsequent beams are formed by moving the aperture across the transducer [15]. Only the linear array transducer has been applied in this work, due to this difference, which is more practical for viewing superficial structures and vascular imaging [16].

1.2.1.b Beam-Forming

The comportment of an US beam is related to the geometry of the transducer elements and the wavelength of the emitted acoustic wave. The phenomenon which shapes a beam is diffraction [21]. For an unfocused or plane-wave multi-element beam, it is more specifically the interaction and interference patterns between the diffracted waves of each transducer element; the wave field can be found by collectively combining the diffracted wave pattern of each of the elements [23].

The acoustic field has two notable regions separated by a zone for which the beam has a minimum cross-section due to inherent convergence referred to as diffractive focusing. Just after the diffractive focal zone, the beam then diverges. These two regions are the near field (or *Fresnel zone*) and the far field (or *Fraunhofer zone*) [23].

Although diffractive focusing exists, in general, it occurs beyond the desired depth for medical imaging. Thus, standard imaging involves the application of electronic delays prescribed to each element, which act to focus the beam more sharply at a desired depth within closer proximity to the transducer; curved apertures or lenses may also be used. The concept of electronic delay focusing is illustrated in figure 1.6. By applying transmit pulses at variable time delays each element will emit a pulse at differing times [23].

When discussing focused beam-forming (refer to figure 1.7), an important parameter to mention is the F-number. The F-number is the ratio of focal distance,

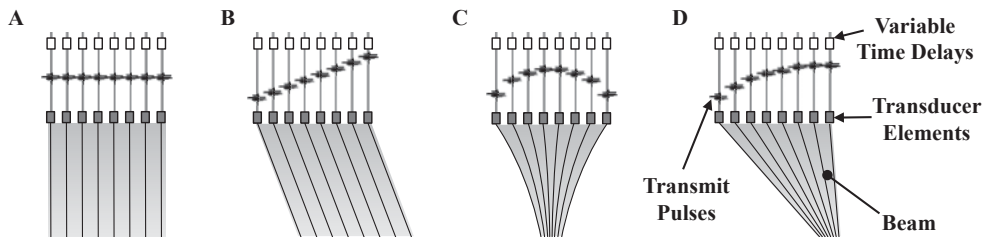

Figure 1.6: Beam-forming using electronic delays to produce A. a flat plane-wave, B. an oriented plane-wave, C. a focused beam, and D. an oriented focused beam. Based on [27].

D_f, to aperture diameter, D_{ap}, as expressed here, $F_{\#} = D_f / D_{ap}$. For a certain F-number, the beam width, D_b, can be computed as $D_b = \lambda F_{\#}$ [21]. From this formulation, the F-number is implicated in the image quality by means of the lateral resolution (see section 1.2.3.b).

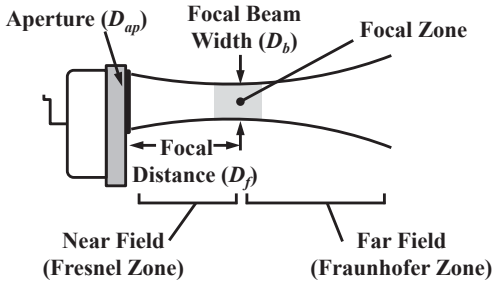

Figure 1.7: Profile of a conventionally focused US beam showing the focal zone at the division between the near and far field. Based on [26].

Another term which arises frequently when dealing with beam-forming is apodization. Although one central beam is depicted in the former diagrams, side-lobes are also present in the acoustic field and adversely affect the quality of the images through adjacent echoes, which interfere with the imaging area [22]. Apodization describes the act of separately weighting each transducer element in transmit and receive with prescribed amplitudes, in an attempt to decrease the effect of side-lobes [21].

Intense side-lobes referred to as grating-lobes may also be of concern. The root of the problem comes from a kind of under-sampling of the array [21]. If the elements are spaced too far apart, rather than emitting one beam, multiple separate beams will develop. Indeed, in order to avoid this artefact, the elements of the transducer should be spaced with a pitch equal to or lesser than a half wavelength,

which for a 5 MHz array, used in this study, means a pitch of less than 0.154 mm. It should be noted that grating-lobes worsen with transmit angle; angled Doppler acquisitions and phased array images are more susceptible [21].

1.2.2 Pulse-Echo Scanning

As previously mentioned, the US scanning sequence will be discussed solely with respect to linear array transducers, employed in this project. First, the linear transducer emits a pulse from a number of active elements called an aperture which forms the beam [23]. Due to the small area covered by each beam, the region of interest is acquired by emitting multiple consecutively formed beams starting from one side of the array and moving sequentially to the other (shown in figure 1.5 and later in figure 3.2). The center-line of each beam corresponds to one scan-line of the resultant image [23].

Another aspect that should be mentioned is that standard 2D diagnostic US is based on a pulse-echo technique. The emitted wave propagates and the backscattered echoes are received by the transducer before the subsequent pulse is excited [23]. Knowing the speed of sound, c, and the time duration, t, the depth, z, at which the echoes arise, describing the spatial structure in the medium, can be determined by

$$z = \frac{c\,t}{2} \quad , \qquad 1.3$$

where the factor of two refers to the two-way travel distance to the scatterers depth and back to the transducer. The rapidity of the transmitted and received wave speed allows for real-time implementation, which is an advantage over other medical imaging modalities [15].

However, due to the necessity to acquire multiple focused beams to cover a sufficient region of interest, there exists a compromise between the spatial and temporal resolution of a series of images. The spatial quality is dependent on the number of excited beams [23]; the more beams used to cover the imaging plane

the better the spatial resolution, consequently at the expense of loss in temporal resolution, i.e. lower frame-rate.

1.2.3 Image Quality

Two major ways in which image quality is quantitatively assessed are through the signal-to-noise ratio (SNR) and image resolution. These two imaging aspects are discussed here.

1.2.3.a Signal-to-Noise Ratio

Noise originates from the transducer, system, and also as an artefact produced by the randomness of the medium itself. The SNR is calculated by comparing the maximum power of the received signal to the power of the noise in the signal,

$$SNR(z) = \frac{\mu_s}{\sigma_s} \quad , \qquad 1.4$$

where μ_s indicates the mean of the signal and σ_s is the standard deviation of the signal, representing the noise [16].

From (1.4), the SNR improves with increasing signal power. This also implies that the SNR worsens with distance travelled, z, because the signal is subject to attenuation which varies with depth, and on the other hand can be improved by increasing the emitted signal energy, within safe limits. As an alternate solution, the length of the transmit pulse may also be increased to provide more energy, as is typically used for CD imaging [22]; however, increasing the transmit pulse comes at the expense of decreasing the bandwidth, in other words, lowering the quality of the image resolution [15].

1.2.3.b Image Resolution

The image resolution specifies the minimum distance for which objects are independently discernible, and can be characterized particularly in 2D: axial and lateral. Axial resolution reflects the minimum gap between two scatterers in the axial direction and is dictated by the product of the number of emitted cycles per pulse and pulse wavelength, also referred to as the spatial pulse length. For a

certain distance, d, between two scatterers, an echoed wave will travel $2d$ before returning to the position of the first scatterer; thus the smallest distinguishable spacing between points is half the spatial pulse length [23]. By decreasing the number of cycles per pulse, providing a shorter pulse length, the axial resolution will be improved. Likewise, emitting higher frequency pulses will also improve the axial resolution because the wavelength is decreased [21]. In as much as the axial resolution is only dependent on the emitted pulse, it is thus uniform in depth. In the case of CD imaging, longer pulses are employed which provide a narrower bandwidth to provide better velocity estimates using the conventional phase-shift estimation (see section 2.3.2) [22]. Consequently Doppler imaging has lower axial resolution compared with anatomical B-mode imaging.

Contrarily, the lateral resolution varies with depth. The ability to distinguish between two adjacent scatterers at equal depth defines the lateral resolution and depends on the width of the beam [22]. Inherently, for focused imaging, the lateral resolution is best in the focal zone at which the beam width is at a minimum and degrades with increased axial distance from this zone, both in the near and far fields. To improve the lateral resolution, multifocal imaging has been introduced. Multifocal imaging is performed using multiple consecutive beams covering the same target area, each of which have been beam-formed to focus on different locations [21]. Although multifocal imaging provides improved resolution, again it comes at a compromise to the temporal resolution, effectively lowering the frame-rate by the number of focal zones acquire for each image line [21].

Chapter 2 : Blood Flow Imaging

In the previous chapter the basic physical principles involved in medical ultrasound (US) imaging were provided, placing emphasis on blood related interaction. In this chapter, we use those principles as a foundation to provide a more in depth explanation on the use of US for blood flow quantification. Here we discuss how blood velocity estimation is performed, what steps are involved in the process and some of the limits imposed on the velocity estimate.

2.1 Introduction

Initially, blood flow measurement was based on a continuous transmission scheme; however, due to practical limitations, blood flow imaging evolved to a pulsed-wave (PW) technique, which is employed in colour-Doppler (CD) imaging.

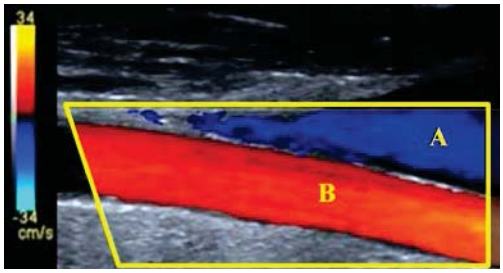

Figure 2.1: A typical CD image of the jugular vein (A) and carotid artery (B) demonstrating blood visualization. This image depicts the 1D projection of velocity magnitude in-line with the beam (oriented by the yellow trapezoid). Adapted from [28].

CD imaging is currently the most widely used clinical imaging modality to diagnose cardiovascular integrity. It does so by providing 1D velocity estimates of flow, at gridded spatial locations, for a 2D planar region of interest as shown in figure 2.1. Figure 2.1 depicts a typical CD image, which divulges two important pieces of information; relative direction, and magnitude of the projected flow velocity. Typically, the colour coded scale ranges from blue (flow away from the transducer) to red (flow toward the transducer); hence, the direction of the flow in-line with the beam. The magnitude of the velocity is given by the hue of the colour scale.

2.2 Continuous-Wave Doppler

Blood velocity estimation began as a simple scheme called continuous-wave (CW) Doppler, based on the Doppler Effect which specifies the change in frequency perceived by an observer moving relative to a wave source. An observer moving toward (away from) a signal source, will detect a frequency higher (lower) than that which was emitted [16, 21]. Likewise, if the source moves toward (away from) a stationary observer, the observed wavelengths are shorter (longer) than that which was emitted. In blood imaging, during emission the probe acts like a fixed source and blood behaves like the moving observer. In reception, the blood is a moving echo source to the receiving transducer, in a fixed position [16, 21].

The Doppler frequency, i.e. the frequency shift between the transmitted and received signals, can be stated as,

$$f_d = f_r - f_0 = 2 f_0 \frac{V \cos\theta}{c} \quad , \qquad 2.1$$

where f_0 is the frequency of the transducer, f_r is the received frequency of the returning signal, V is the velocity of the blood at angle θ to the axis of transmission, and c is the acoustic speed. A positive frequency shift indicates a scatterer advancing toward the probe. Vice versa, a negative frequency shift indicates a scatterer moving away from the probe. From the term $V\cos\theta$, which indicates the axial velocity, it is clear that only the projections of the velocity parallel to the beam direction can be fully ascertained [16, 21].

2.2.1 Scanning

CW Doppler makes use of a relatively constant sinusoidal signal with a very narrow bandwidth. The signal is generally emitted and received from two separate apertures contained in the same probe housing [22]. Again, central frequencies of 1 to 10 MHz are typically used for medical US. The deeper the structure the lower the frequency should be. Due to the narrow bandwidth, broadening (see section 2.2.2) of the Doppler frequency and frequency dependent attenuation will be relatively small [22].

The Doppler shifts are considerably small, hence the receive frequencies will not stray significantly from the central frequency. Then, to properly sample the signal, Nyquist theorem should be heeded; a sampling frequency two times the maximum frequency content should be used. Finally, demodulation (see section 2.2.3) is used to determine the Doppler frequencies [22].

2.2.2 Spectral Broadening

Certainly not just one value of frequency shift is measured from a scan but a spectrum of frequencies. This creates a broad spectral bandwidth which in general remains centered about the received central frequency [22]. The amount of broadening depends on a few factors which may be related to the method of acquisition (intrinsic) or to the character of the field in view (extrinsic).

A predominant factor causing intrinsic spectral broadening is called *geometrical broadening*. Geometrical spectral broadening is due to the variant angles at which the emitted wave will contact different scatterers in a sample volume, and the different angles for which the backscattered echoes are received [22, 29].

The chief modes of extrinsic spectral broadening are attributed to the character of the flow. Broader spectrums are produced for sample volumes containing scatterers with differing velocities. For example, areas of turbulent flow with seemingly more erratic behaviour have broader Doppler frequency spectrums [22].

2.2.3 In-Phase Quadrature Demodulation

To extract the Doppler frequency, the received signal is demodulated. Demodulation is also referred to as down-mixing. Using the central frequency, f_0, the spectrum can be shifted to baseband [22, 30]. This step helps reduce the amount of data for post-processing as the highest frequency will be reduced; further implying that the sampling frequency may also be reduced without loss of information, according to the Nyquist theorem [22, 30]. All necessary information is maintained in the demodulated signal, despite the elimination of the higher frequencies out of the transducer bandwidth, using simple low-pass filtering [22].

In-phase quadrature (IQ) demodulation is performed by multiplying the real radio-frequency (RF) signal, *RF(t)*, by a complex exponential function,

$$IQ(t) = RF(t) \cdot e^{-2\pi i f_0 t} \quad , \qquad 2.2$$

where *IQ(t)* is the complex demodulated IQ signal, *t* is time in samples along the received beam, and f_0 is the central frequency of the emitted signal. Using trigonometric identities the complex exponential function can be broken down into the cosine and sine functions demonstrated by $e^{-2\pi i f_0 t} = \cos(2\pi f_0 t) - i\sin(2\pi f_0 t)$, which yields two sinusoidal signals separated by a 90 degree phase difference [30]. In simplified notation, the complex signal can be represented by the real in-phase signal, *I(t)*, and the imaginary quadrature signal, *Q(t)*,

$$IQ(t) = I(t) + iQ(t) \ . \qquad 2.3$$

The complex IQ signal contains phase, frequency and amplitude information.

That the original receive signal is real, indicates that the signal possesses a symmetry between the positive and negative ends of the frequency domain as shown in figure 2.2, before IQ demodulation. A basic property of the Fourier transform is that multiplying a function by an exponential of frequency f_0 in the time domain is equivalent to a downward translation of the signal by f_0 in the frequency domain: $h(t)e^{-2\pi i f_0 t} \leftrightarrow H(f - f_0)$. This shift is demonstrated by the Doppler frequency, f_d, in figure 2.2, after IQ demodulation.

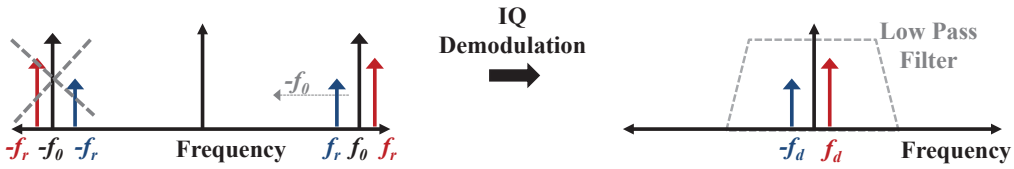

Figure 2.2: Complex IQ demodulation. The frequency spectrum, f_r, of the received RF signal is shifted to baseband and the symmetry is broken using low-pass filtering, allowing unambiguous determination of the flow direction. Adapted from [21, 25].

Complex IQ demodulation allows detection of the velocity direction by discarding the negative end of the spectrum using a low pass filter. IQ demodulation allows the signal to maintain the same frequency and amplitude contents; however, the

symmetry in the positive and negative ends of the frequency spectrum is eliminated. [15].

2.3 Pulse-Wave Doppler

The main drawback of CW Doppler is the inability to discriminate the depth at which the echoes arise because the transmission and reception occur simultaneously and in close proximity. Vague speculation can be made to determine the depth based on the depth attenuation of the echoes; however PW Doppler was introduced to address this limitation [15, 22]. As suggested in section 1.2.2, US pulses are emitted intermittently at a pulse repetition frequency (PRF) of f_{prf}. The time period between the wave transmissions is reserved for reception of the returning echoes. Depth can be established from the travel-time between transmission and reception of the signal with the simple relationship given in (1.3) of section 1.2.2. [15, 22].

PW transmit bursts can be distinguished from CW emissions based on bandwidth. Short-pulsed emissions result in broader bandwidths compared with the nearly monochromatic narrow bandwidths of CW Doppler [15, 22]. On account of this, it is not feasible to detect the ordinary Doppler shift which may be concealed by overlapping bandwidths. As another consequence of larger bandwidths, the frequency spectrum is more susceptible to a downshift in the receive center frequency due to attenuation [22]. The character of the PW bandwidth means that despite its name, standard CD has been adapted and is not based on the Doppler Effect. Rather, after IQ demodulation (refer to section 2.2.3), the signals are subjected to a method of correlation applied to consecutively received RF lines [15, 22]. The two main methods of correlation are presented in sections 2.3.2 and 2.3.3.

Before continuing further, to avoid incertitude, a distinction is made in relation to ‘time’: fast-time and slow-time (see figure 2.3). The echoes received by the transducer between emitted pulses are discretized at a rate equal to the sampling frequency, f_s. Each individual waveform produced is a fast-time waveform. A

series of fast-time waveforms can be sampled at the same spatial location to produce a slow-time waveform, which is defined by the PRF [21, 26].

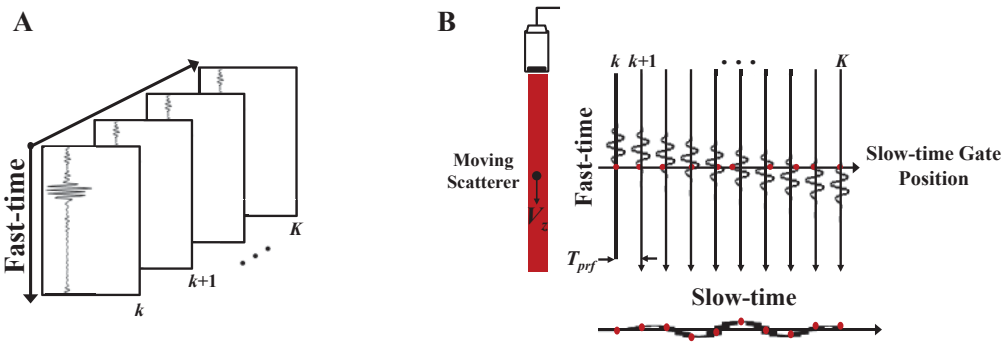

Figure 2.3: The fast-time and slow-time dimensions are shown in part A. The fast-time signal is the waveform produced by sampling the receive signal of one beam, pertaining to the depth scan. The slow-time signal is the waveform produced by sampling a packet of pulses at the same location. In part B, a packet of receive pulses from a point scatterer is moving away from the transducer in the axial direction. The slow-time signal is sampled (shown with red points) at a gated position producing the slow-time waveform. Based on figures from [31] and [15].

The principle behind CD can be simplified by observing a brief sinusoidal pulse, $z_t(t)$, given by,

$$z_t(t) = g(t)\sin(2\pi f_0 t)$$
$$g(t) = \begin{cases} 1, & 0 < t < \frac{M}{f_0} \\ 0, & else \end{cases}, \qquad 2.4$$

emitted into a sample volume containing one point scatterer, where f_0 is the center frequency, t is time, $g(t)$ is a step function indicating that the emitted pulse is a short burst over a certain number of sine periods, M, and zero otherwise.

If we disregard attenuation, the returning echo should possess the same form as the emitted pulse but with a certain delay corresponding to a travel-time, τ, to and from the scatterer [15]. Furthermore, if a single scatterer is moving within the region of interest at an axial velocity V_z, over a pulse repetition period of T_{prf}, then its change in displacement would be equal to $\Delta z = V_z T_{prf}$. Thus, consecutively received signals would differ only by a time-shift or difference in fast-time flight time equivalent to

$$\Delta\tau = \frac{2\Delta z}{c} = \frac{2V_z T_{prf}}{c}, \qquad 2.5$$

also shown in figure 2.3 [21, 32]. A noteworthy remark is that, in figure 2.3B, the travel-time required to encounter the scatterer, along the fast-time waveform, increases in each subsequent line causing a shift away from the transducer, meaning the scatterer is moving in the negative velocity direction. Shifting toward the transducer would indicate positive velocity.

If a single sinusoidal pulse, given by (2.4) is periodically emitted to a moving scatterer, as shown in figure 2.3B, the received slow-time signal will be,

$$z_r(k) = \sin\left(2\pi \frac{2V_z}{c} f_0 \; k\, T_{prf}\right) \quad , \qquad 2.6$$

where k is the line number, and the product of k and T_{prf} represents time. The center frequency of the slow-time signal can then be approximated as,

$$f_{slow} = \frac{2V_z}{c} f_0 \quad . \qquad 2.7$$

So, the slow-time signal will also share the same waveform as that which was emitted; however, with a scaled frequency axis, expanded by a factor of $2V/c$ [15, 21].

Although the former discourse was given in a simplified context for one point scatterer moving in a sample volume, neglecting attenuation, tissue is composed of a multitude of scattering objects with variable motion [32]. Therefore, the waveforms, both in fast and slow-time, will be an aggregation of many complex scattering signals also subject to frequency dependent attenuation. Again, as was expressed in section 1.1.1.b on blood scattering, each waveform is then considered a Gaussian random process [22].

It is also worth mentioning, of course, that the Doppler Effect still occurs; however, it presents a negligible artefact in the velocity estimation. If the displacement is slight, and the scatterer moves little within the width of the beam, estimation may be valid [22].

2.3.1 Pulse-Wave Velocity Limitations

The detectable velocity limits using CD are preordained by the PRF. The PRF imposes restrictions on both the maximum and minimum velocities. Therefore, selection of the PRF can be consequential.

2.3.1.a Maximum Velocity Criteria

The Nyquist theorem dictates that a signal should be sampled at a rate of at least two times the maximum frequency content in the signal to avoid signal artefacts referred to as aliasing [15]. Aliasing arises when a signal is not adequately sampled, whereby the discretized waveform will not yield a faithful representation of the true continuous signal being sampled. The maximum attainable velocity is then dependent on the signal sampling [15].

As expressed in (2.5), the fast-time delay between two consecutive signals can be found directly from the change in position or axial velocity of the scatterer. If the Nyquist theorem is respected, the maximum detectable fast-time delay should be less than twice the emitted central frequency, $\Delta\tau_{\max} \leq {}^{1}\!/_{2f_0}$ [15]. Therefore, the maximum axial velocity can be written as,

$$Vz_{\max} = \frac{c\, f_{prf}}{4 f_0} \quad . \qquad 2.8$$

To accommodate for higher velocities the PRF can be increase; however, at a certain point, increasing the PRF compromises the maximum depth of scan. To be certain that precedent echoes are not contributing to the signal of interrogation, the PRF should correspond to the correct depth, ensuring that $f_{prf} \leq {}^{c}\!/_{2z_{\max}}$ [15].

2.3.1.b Minimum Velocity Criteria

Although acquiring too many slow-time samples may compromise the acquisition time, taking too few limits the minimum detectable velocity. As the pulse repetition frequency (slow-time sampling frequency) is fixed, insufficient sampling means signal truncation, equivalent to the application of a rectangular window to the slow-time signal, in the time domain. This is problematic in that the

frequency domain incurs spectral broadening and can pose a challenge when trying to distinguish slow moving targets from the strong signals of near-stationary objects [15].

To preclude this dilemma, at least one full period of the waveform should be sampled to improve lower velocity estimates. If K acquisitions (pulse transmissions) are acquired at a PRF of f_{prf}, then the lowest frequency obtainable is $f_{slow,\min} = f_{prf} / K$ [15]. Then, the minimum detectable velocity is given by,

$$Vz_{\min} = \frac{c\, f_{slow,\min}}{2\, f_0} = \frac{c\, f_{prf}}{2K\, f_0} \quad . \tag{2.9}$$

where, again c and f_0 are the acoustic wave speed and central frequency, respectively.

2.3.2 Phase-Shift Estimation

The advent of real-time blood flow imaging was driven by the development of phase-shift estimations. Today, the phase-shift autocorrelation estimation technique, introduced by Kasai *et al.* [33], is predominantly implemented on commercial US scanners. This method enables the estimation of the axial shift in the position of the target scatterer, indicating the motion of the blood between subsequent slow-time RF signals, while maintaining an acceptable frame-rate. Although previous methods existed, to provide velocity estimates on two consecutive lines, Kasai *et al.* developed a method which allows the consideration of multiple lines to improve the estimate [15]. Since the phase-shift autocorrelation method is used in this work, a brief description is provided in the following subsections.

2.3.2.a Axial Velocity Estimation

From (2.7), the velocity of the moving target is related to the center frequency of the slow-time signal, acquired by sampling a series of RF signals at a gated position (refer to figure 2.3B). Furthermore, for a number of closely packed

scatterers, the mean axial velocity, $\overline{V}_z$, at the slow-time gated position can be attained from the mean angular frequency, $\overline{\omega}_{slow}$, as follows,

$$\overline{V}_z = \frac{c\overline{\omega}_{slow}}{2\omega_0} \qquad 2.10$$

where, ω_0, is the angular center frequency equal to $2\pi f_0$ and c is the acoustic speed. The mean angular frequency can be calculated using the power density spectrum $P(\omega)$ of the demodulated received signal shown in (2.11).

$$\overline{\omega} = \frac{\int_{-\infty}^{\infty} \omega P(\omega) d\omega}{\int_{-\infty}^{\infty} P(\omega) d\omega} \qquad 2.11$$

Estimation of the power density spectrum is challenging; however, the solution may be facilitated using the autocorrelation function, given by (2.12), which is the inverse Fourier transform of the power density spectrum.

$$R(\tau) = \int_{-\infty}^{\infty} P(\omega) \exp(i\omega\tau) d\omega \qquad 2.12$$

The autocorrelation function represents the similarity between two observations, of a process, as a function of the lag in time, τ, separating them. From this relationship, the mean angular frequency can be re-expressed as,

$$\overline{\omega} = \frac{\dot{R}(0)}{i\, R(0)} \quad . \qquad 2.13$$

where $\dot{R}(0)$ is the derivative of the autocorrelation function with respect to τ, evaluated at τ equal to zero.

Since the autocorrelation function of the complex IQ signal will also be complex, we can rewrite it in polar form as follows

$$R(\tau) = A(\tau) \exp(i\phi(\tau)) \quad . \qquad 2.14$$

Using (2.14), the mean angular frequency from (2.13) can be shown to equal

$$\overline{\omega} = \dot{\phi}(0) \quad , \qquad 2.15$$

where $\dot{\phi}(0)$ is the derivative of the phase of the autocorrelation function with respect to τ, evaluated at τ equal to zero. Using a first order Taylor series

expansion, whereby $\phi(\tau) = \phi(0) + \dot{\phi}(0)\tau$, the mean angular frequency can be estimated by equation 2.16. Since the phase is a real and odd function, then $\phi(\tau = 0) = 0$.

$$\overline{\omega} = \frac{\phi(\tau) - \phi(0)}{\tau} \approx \frac{\phi(\tau)}{\tau} \quad . \tag{2.16}$$

In our case, we have a series of *K* received time-dependent demodulated complex IQ signals separated by a pulse repetition period of τ equal to T_{prf} over the same location. Thus the discrete autocorrelation for consecutive observations can be stated as

$$R(T_{prf}) = \frac{1}{K-1}\sum_{k=1}^{K-1} IQ^{*}(k)IQ(k+1) \tag{2.17}$$

where the variable *k* represents the k^{th} line of a series of the *K* demodulated signals and the symbol * represents the complex conjugate. The phase $\phi(T_{prf})$ of the complex autocorrelation function *R* is given by,

$$\phi(T_{prf}) = \arctan\left(\frac{\mathrm{Im}\{R(T_{prf})\}}{\mathrm{Re}\{R(T_{prf})\}}\right) \quad . \tag{2.18}$$

Consequently, the final form describing the axial velocity estimate, using (2.10), can be stated as follows,

$$V_z = \frac{c}{4\pi f_0 T_{prf}} \arctan\left(\frac{\sum_{k=1}^{K} Q(k)I(k-1) - Q(k-1)I(k)}{\sum_{k=1}^{K} I(k)I(k-1) - Q(k-1)Q(k)}\right) \quad . \tag{2.19}$$

where, given in (2.3), *I* and *Q* are the in-phase and quadrature components of the complex signal.

2.3.2.b Velocity Limits

The velocity limits particular to the phase-shift estimation based on autocorrelation are set by the inverse tangent trigonometric function, in (2.19). Both the real and imaginary parts of the signal are used so the phase can be determined. In this case the phase is limited to the range of ±π. As a consequence the range of velocities is from $\pm Vz_{max}$ calculated by,

$$Vz_{\max} = \frac{c}{4 f_0 T_{prf}} \quad . \qquad 2.20$$

Measured velocities which lie outside the detectable velocity range will result in aliasing. Cyclometric functions like the inverse tangent have a particular range which will repeat over an extended domain [15]. For this reason, velocities of $Vz_{max}+\delta V$ which exceed the velocity range will be wrapped to the other end of the cycle at $-Vz_{max}+\delta V$, and vice versa for velocities which exceed the minimum velocity conditions. Conventional CD imaging, allows limited control over the maximum attainable velocity by adjusting the PRF [15], as mentioned in section 2.3.1.a.

2.3.3 Time-Shift Estimation

The time-shift estimation was introduced for motion detection to resolve the velocity limitations imposed by the trigonometric function in the phase-shift estimation. Although the time-shift estimation eliminates the concern for aliasing, the computation is significantly more cumbersome. The estimate may also be more susceptible to errors due to false detection for lower SNR [15, 34]. The main principles of the time-shift estimation are described in the following sections.

2.3.3.a Axial Velocity Estimation

In essence, the time-shift estimation calculates the axial velocity in the time domain based on a delay between progressively collected RF signals. Supposing that a scatterer moves within a medium a distance of Δz, with respect to the beam direction, it should produce the same echoed pattern or impulse response in consecutive RF lines; however, with a certain fast-time time delay, $\Delta\tau$, corresponding to the distance travelled by the scatterer between pulses [15]. Equation 2.21 depicts the axial velocity for a certain pulse repetition period, T_{prf}.

$$V_z = \frac{\Delta z}{T_{prf}} = \frac{c\Delta\tau}{2T_{prf}} \qquad 2.21$$

To determine the delay between signal patterns in a particular window or range-gate, the cross-correlation is applied. The cross-correlation function compares the

likeness between the initial signal, $z_k(t)$, and a subsequent signal, $z_{k+1}(t)$, shifted by variable lag. The cross-correlation shifts the second signal along the first signal calculating the integral of their product for each shift [15, 34]. The best match between the two signals will yield a maximum in the cross-correlation function; to which the maximum value corresponds to the correct shift, in other words, time delay. The equation demonstrating the discrete cross-correlation function is given here,

$$R(s, N_0) = \frac{1}{N_s} \sum_{l=0}^{N_s-1} z_k(N_0 + l) z_{k+1}(N_0 + l + s) \qquad 2.22$$

where R is a function of the lag, s, between signals, and the location of the window designated by N_0, which refers to the starting sample of the initial signal. The size of the window or range gate, in samples, is allotted by the variable N_s, for which each sample is represented by l [15, 34].

Similar to the phase-shift estimation, the velocity can be improved by averaging multiple line estimates. Additionally, to obtain a decent estimation, the sampling frequency should be at least four times the central frequency of the transducer, which improves the velocity resolution [15].

2.3.3.b Velocity Limits

The velocity limits of the time-shift estimation depend on the size of the range-gate to which the cross-correlation is applied. Since the velocity is directly proportional to the lag in the second signal, the highest velocity which can be detected is then directly proportional to the range gate [15, 34]. If the gate length N_s is only a few time samples, it may not be long enough to account for the motion of the scatterer. The maximum attainable velocity is described in the following equation,

$$Vz_{\max} = \frac{c\, N_s}{2\, T_{prf}\, f_s} \quad . \qquad 2.23$$

Again, where c is the acoustic speed, T_{prf} is the pulse repetition period, and f_s is the sampling frequency. The minimum velocity is then determined simply by

$$Vz_{\min} = \frac{c}{2\,T_{prf}\,f_s} \quad . \tag{2.24}$$

To improve the velocity resolution without increasing the sampling frequency excessively, at the expense of computation time, interpolation can be utilized. One commonly used method of interpolation is parabolic peak fitting of the cross-correlation function [15, 34]. Parabolic peak fitting works by plying a polynomial of second order to the apparent correlation peak and to the two surrounding points; the interpolated peak then corresponds to the peak of the conformed parabola. The determination of the lag at the interpolated peak, s_{int}, is given by,

$$s_{\text{int}} = s + \frac{R(s+1) - R(s-1)}{2\big(R(s+1) - 2R(s) + R(s-1)\big)} \tag{2.25}$$

where s is the original non-interpolated lag determined using regular cross-correlation, $R(s)$ indicates the value of the correlation at lag s, and $R(s\pm1)$ gives the correlation values surrounding the peak. The interpolated velocity becomes [15],

$$Vz_{\text{int}} = \frac{c\,s_{\text{int}}}{2\,T_{prf}\,f_s} \quad . \tag{2.26}$$

2.3.4 Clutter Filtering

Clutter filters are high-pass filters applied to improve blood flow estimations. Such a filter is applied to remove motion detected from near stationary tissues surrounding the lumen of the vessel and may also be helpful in removing signal from side-lobes and reverberations which may manifest as artefacts within the blood signal [21, 22]. These low-frequency tissue signals have higher amplitudes, typically in the range of 40 to 100 dB higher, than the faint signal produced from blood scattering [35], shown in the schematic of figure 2.4A. For example, vessel walls produce a notable reflection and move comparatively slowly when considering blood flow. The motion of the vessel wall adds to the frequency spectrum a component lesser than 1 kHz [22].

Creating a suitable clutter filter is a complex feat because of the nature of the data. First, filtering occurs just before velocity estimation, thus the data used is based on a limited slow-time sample size and poses limitations on the type of filter which

can be employed [22]. Furthermore, clutter filters must possess some key features necessary for effective design, outlined in figure 2.4B. There are three major zones of a clutter filter: stop-band, transition zone, and pass-band [35].

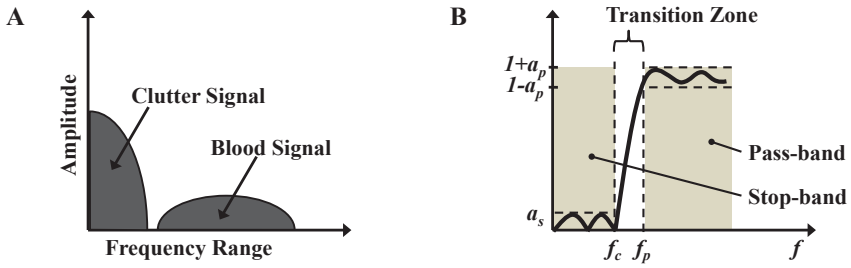

Figure 2.4: A. Doppler frequency range showing blood and clutter signal. Adapted from [26]. B. Features of a high-pass clutter filter. Adapted from [35]

The stop-band is the range of frequencies, from zero to the cut-off frequency, f_c, for which the signal is attenuated. Ideally the frequency response in the stop-band should be zero; small oscillations of amplitude a_s may exist and should be minimized [35]. The transition zone describes the region between the stop-band and pass-band, defined between f_c and the pass-band frequency, f_p, where the frequency response goes from zero to one. Narrow transition zones are more desirable to maximize the clutter attenuation without impeding crucial blood signal at lower frequencies [35]. Finally the pass-band allows frequencies above f_p to pass unhampered. Again, oscillations of amplitude a_p should be minimized for optimal filtering. Many clutter filters have been proposed in literature, the most common types of filters used for this application are finite impulse response filters, infinite impulse response filters and polynomial regression filters. These filters are well described and compared in [35].

Chapter 3 : Improving Blood Velocity Estimation

3.1 Drawbacks of Conventional Blood Velocity Estimation

Although conventional colour-Doppler (CD) ultrasound (US) is an effective technique for qualitative and limited quantitative analysis of blood flow, it possesses two major constraints. These constraints are the angle dependence of US measurements, and the low frame-rate of the standard focused beam approach. The following sub-sections outline these two limitations.

3.1.1 Angle Dependence

Conventional CD provides a 2D planar image superimposed with estimated projections of blood velocity in-line with the incident beam. In other words, CD detects the movement of blood in a 1D manner parallel to the beam direction. Although blood possesses a 3D flow dynamic, all orthogonal components of the blood to the beam go undetected [16]. This indeed yields an error in the estimate as a result of the unknown angle existing between the beam and vessel, as depicted in figure 3.1.

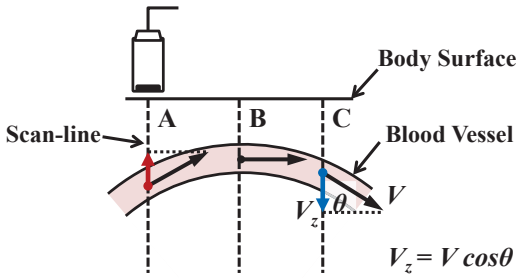

Figure 3.1: Effect of beam to flow angle, θ, on CD measurements. As θ increases toward 90 degrees (from scan-line A to B), the measured velocity magnitude, V_z, goes to zero. Scan-lines A and C differ in direction with respect to the transducer (toward or away), depicted by the red and blue colour scale. Based on figures from [36].

Figure 3.1 demonstrates the Doppler velocities measured from three separate cases of variable beam to flow angle, θ. Although the magnitude of the flow velocity, V, may remain constant, the components obtained will vary with angle. For vessels with complex geometries which run almost parallel to the surface of the body,

acquiring accurate velocity measurements is infeasible with conventional methods. As a solution to this limitation, multidimensional blood velocity estimation techniques have been introduced. These techniques are discussed in section 3.2.

3.1.2 Frame-Rate

Up until this point, blood velocity estimation has been discussed with regards to the slow-time correlation of a packet of K pulsed signals separated by a pulse repetition period of T_{prf} (refer to figure 2.3). CD images are indeed formed in this way; however, each packet contains full images rather than single-line signals. Since conventional US relies on focused beam acquisitions in order to cover a particular lateral region of interest, multiple consecutively fired beams are swept across the medium, for sufficient spatial resolution, depicted in figure 3.2.

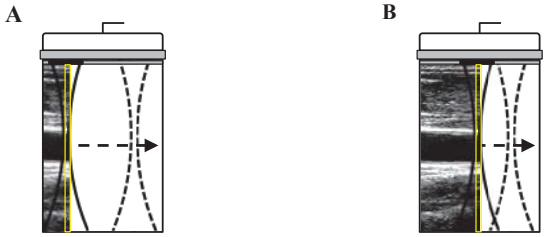

Figure 3.2: Demonstration of the scanning convention of US imaging. The left to right sequence of subsequently fired beams to cover the region of interest in image formation, the yellow box shows the image information acquired for the current beam. Panel A shows the early stage of an image moving toward panel B demonstrating midway through a scan. Based on figures from [37].

Each image will then have the dimensions N_r by N_c, where N_r is the number of rows indicating the sample size of the pulsed signal and N_c is the number of columns indicating the number of pulses necessary to create one image (typically between 64 and 256). The correlation will then be enacted over the packet of images for each column, to compose a CD frame. This means the effective pulse repetition period, $T_{eff,prf}$, for the CD imaging velocity estimate becomes,

$$T_{eff,prf} = T_{prf} \cdot N_c = \frac{2z}{c} \cdot N_c \quad , \qquad 3.1$$

where, c is the speed of sound and z is depth of scan. To have large effective pulse repetition periods, means that the velocity measurements are susceptible to aliasing artefacts due to under-sampling of the slow-time signal, i.e. the Doppler

frequencies. As a second consequence, fast transient events occurring during a brief cardiac cycle may go undetected with such low temporal resolution.

The total time required to obtain the first CD image can then be expressed by

$$T_{FR_0} = T_{eff,prf} \cdot K = \frac{2z}{c} \cdot N_c \cdot K \quad , \tag{3.2}$$

where, the packet size K is useful for decreasing the variance in the estimate [15]. A conventional packet size, K, ranges between 8 and 16 [19]. The protocol for scanning is to use overlapping shown in figure 3.3, which means that after acquiring the initial frame the subsequent time per frame will then be

$$T_{FR} = T_{eff,prf} \cdot K_L = \frac{2z}{c} \cdot N_c \cdot K_L \quad , \tag{3.3}$$

where K_L is interval between packets. The frame-rate is then $f_{FR} = 1/T_{FR}$.

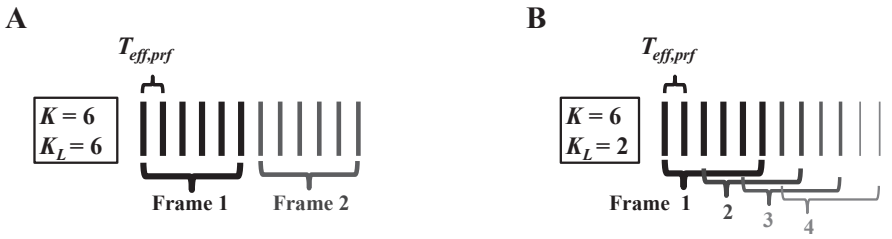

Figure 3.3: Panel A shows an example of image formation with six images per packet and no overlapping which yeilds a frame-rate given by T_{FRo} in (3.2). Panel B demonstrates a typical imaging convention with overlapping. An interval of two images between each consecutive packet will then correspond to a frame-rate equal to T_{FR} in (3.3).

3.2 Two-Dimensional Blood Velocity Estimation

To address the angle dependence constraint, various schemes have been introduced to provide multidimensional blood velocity estimation. Over the years, research has gone into approaches using different hardware configurations, and more commonly, different processing techniques. The ensuing sub-sections describe the more popular post-processing approaches to 2D estimation: speckle tracking, transverse oscillation, and vector-Doppler.

3.2.1 Speckle Tracking

The grainy character in an US image is referred to as speckle. Speckle arises from the interference of the acoustic echoes of closely packed scatterers in a medium and is dependent on the resolution of the imaging system; higher resolution systems will consequently have less speckle as the scatterers will be more distinguishable when densely distributed [38]. Speckle can be desirable or undesirable depending on the application. In the case of B-mode imaging, speckle is disadvantageous. Methods have been introduced to eliminate speckle; predominately, compounding a set of images to produce one image will improve the resolution [38]. Contrarily, speckle can be used advantageously; for example, in blood flow estimation speckle patterns are observed and tracked to determine changes which indicate the movement of blood flow [39-42].

Speckle tracking was introduced by Trahey *et al.* [43] and makes use of a 2D cross-correlation. The 2D cross-correlation works by acquiring two images at times t_0 and t_1, and seeking the maximum semblance between a windowed region or kernel, W_0, from the initial image, and a similarly sized window, W_1, displaced by Δx and Δz within a larger search region of the subsequent image, shown in figure 3.4. The best match corresponds to the displacement of the blood. Finally, the lateral and axial velocities of the blood can be found knowing that the time between acquisitions, Δt, which is equal to $t_0 - t_1$ [40].

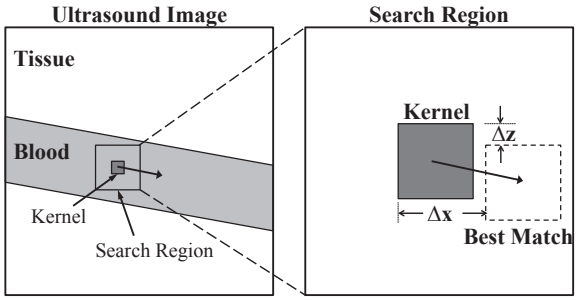

Figure 3.4: Speckle tracking using a 2D cross-correlation. With a pre-selected kernel from image one, a search is performed to find an equally sized window, in a larger search region of the subsequent image, which possess the most similarity to a pre-selected kernel. Adapted from [39].

It should be noted that speckle tracking is computationally expensive when compared with other techniques for 2D blood velocity estimation. In response,

adaptations of this method have been used to decrease the computational load such as the sum-of-absolute differences introduced by Bohs *et al.* [44]. Additionally, speckle tracking requires sufficiently high frame-rates to avoid decorrelation. A nice review of the advancements made in speckle tracking is provided in [40].

3.2.2 Transverse Oscillation

The transverse oscillation method was introduced by Jensen *et al.* [32] and has been investigated in depth by Udesen *et al.* [45]. This method can provide estimates of both axial and lateral components of velocity using US.

As previously discussed, longitudinally oscillating waves enable the estimation of the axial velocity in a medium. The transverse oscillation method uses the same foundation by suggesting that oscillations in the transverse direction can provide lateral velocity components [32]. The creation of a doubly-oscillating pulse echo field can be done by altering the receive aperture apodization. In essence, the apodization is controlled in order to mimic an aperture with two separated point sources [46]. The grating lobes of the two point sources will then yield the transverse oscillations required for lateral velocity estimation [45]. Figure 3.5 shows a simplified demonstration of a pulse-echo field created by two point sources exhibiting longitudinal and transverse oscillations.

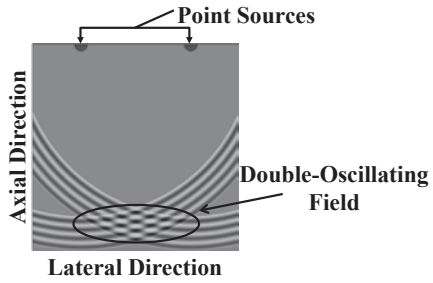

Figure 3.5: Basic depiction of two point sources creating both longitudinal and transverse oscillations, clear in the encircled region. Adapted from [46].

Akin to the conventional phase-shift autocorrelation method by Kasai *et al*., [33] based on the axial in-phase quadrature signal, the axial and lateral velocities from the transverse oscillation method are found with a slightly more involved methodology. The transverse oscillation method uses a spatial quadrature

approach; two 90 degree phase-shifted signals for each spatial direction are used [45, 46]. The phase-shifted signals in the transverse direction are acquired with a pair of parallel beam-formers in reception, enabling the beams to be spatially separated by one quarter of a transverse-wavelength, equivalent to a 90 degree phase-shift. A slightly modified complex autocorrelation is then used to find the axial and lateral velocity components, as described in [32, 45].

The validity of transverse oscillations has been tested using ultrasound simulations and *in vitro* flow phantoms [45, 47]. An *in vivo* study was made with comparison to magnetic resonance imaging (MIR) angiography [48]. However, this technique still relies on focused beam techniques.

3.2.3 Vector-Doppler

Since the inception of CD US, several methods combining Doppler measurements have been introduced to deal with the 1D nature of US velocity estimates. Vector-Doppler (VD) is a natural extension of colour-Doppler and relies on the triangulation of classical Doppler measurements from different angled perspectives. Variant proposals using hardware modifications have been introduced. Early techniques involve one, single or multi-element, probe which is displaced between angled acquisitions to obtain multiple perspectives [49-51]. Other techniques used setups with more than one, single or multi-element, probe in a fixed configuration [51].

Such approaches involve spatial alignment and temporal matching to ensure that the triangulated measures coincide with the same location and identical moments of the cardiac cycle. These techniques are vulnerable to mismatching errors [52]. Additionally, such methods are not practical for imaging areas of the body with complex surface geometries, such as the carotid arteries, as they necessitate the placement of multiple probes or displacement of a single probe in a limited area of interrogation [52].

It is then logical that VD techniques were adapted using beam-steering with a single multi-element transducer [13, 53, 54] as demonstrated in figure 3.6. One

stationary transducer is placed, on the skin, above the region of interest to attain dual co-planar acquisitions. The common area between the two illuminated zones can be used for triangulation, as the projected velocity components, V_p and V_n, from positively and negatively oriented acquisition, of angle $\pm\beta$, are known.

An all-encompassing review of various VD approaches is given by Dunmire *et al.* [52]. Finally, some groups have used VD coupled with regularization to improve the 2D velocity estimates by alleviating the data set from noisy, missing and outlying data [14, 55]. Since VD is employed in this work, more details describing this technique will ensue in section 4.3.3.

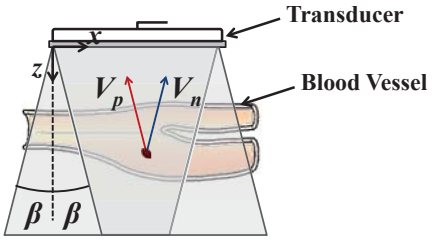

Figure 3.6: Exemplification of the VD scanning configuration using a stationary linear probe. Two β-angled images (marked by overlapping parallelograms), created by beam-steering, which encompass a blood vessel. Moving blood produces a signal arising at any (x,z) position which will yield velocity projections, V_n and V_p (from the negatively and positively oriented angled images). Based on [19].

3.3 High Frame-Rate Imaging

Due to the large effect that frame-rate has on the performance of blood velocity estimation, many groups have strived to better characterize flow using high frame-rate imaging. By appreciably increasing the frame-rate, the dynamics of fast moving blood can be capture more readily. The more commonly known methods to overcome the frame-rate limitation, which are subsequently discussed, are beam-interleaving, parallel beam-forming, and plane-wave imaging.

3.3.1 Beam-Interleaving

Beam-interleaving is a technique used to increase the effective pulse repetition frequency (PRF) by dividing the scanning plane into sub-regions or interleave groups in the lateral direction. Although beam-interleaving does not affect the

overall frame-rate, it is placed in the high frame-rate category as it can provide better temporal resolution within each interleave group. Thus, beam-interleaving has the ability to capture higher velocity motion than conventional Doppler methods.

This concept is depicted in figure 3.7. Each of the three simplified scenarios in panels A, B and C, are comprised of 24 beam scans in total; six scans are used to cover the region of interest in the lateral direction, and each sequence is composed of a packet of four images for the velocity estimation. The difference between each panel lies in the beam sequence order, indicated by the pulse number. In panel A, the conventional CD scheme is presented; all six beams are fired for the first image in the packet before continuing on to the next image in the packet (refer to section 3.1.2).

In panel B, beam-interleaving is shown. The region of interest (ROI) is divided into two interleave groups with an interleave group size equal to three. This means three beams are fired to acquire part of the first image in the packet before continuing on to fire three beams for part of the next image, in the packet of the same interleave group. Once the full packet is acquired for the first interleave group, the same sequence is followed for the subsequent interleave group. The effective PRF increase achieved by interleaving (over the conventional scheme) is by a factor equal to the number of interleave groups per image.

Finally, panel C shows a scheme where the maximum effective PRF can be satisfied. Each beam is repeated K-times to fill the packet size requirement, then the sequence is repeated after each laterally displaced beam.

In a study by Jensen *et al.* [56], beam-interleaving was used in conjunction with a 2D cross correlation. Lateral and axial velocities were extracted from Field II [57] simulated data of stationary parabolic flows at an increased effective PRF of 3500 Hz. In [58], vector maps were obtained *in vitro* from a spinning disc model through triangulation of dual-angle Doppler measurements using a split-aperture (two interleave groups), with which they doubled the effective PRF.

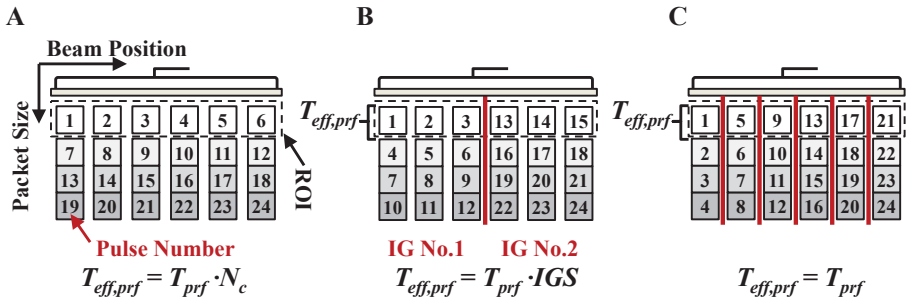

Figure 3.7: The beam sequence, indicated by the pulse number, for three types of acquisitions: panel A shows the conventional CD scheme where the effective pulse repetition period, $T_{eff,prf}$, is equal to T_{prf} by N_c; panel B shows beam-interleaving where $T_{eff,prf}$ is equal to T_{prf} by the interleave group size (equal to three); and panel C depicts an interleaved scheme where $T_{eff,prf}$ is equal to T_{prf}. Interleaved groups are separated by red lines. Modified from [25].

A few years later, Azar *et al.* [59], demonstrated the capacity of beam-interleaving, to improve high velocity motion detection. In their method, they obtained Doppler projections at alternating interleaved dual angles. Using triangulation they obtained lateral and axial displacements necessary to calculate velocity. Their method was tested on an *in vitro* steady pipe flow phantom and *in vivo* on a healthy carotid artery. Azar *et al.* were able to achieve effective PRFs of between 833 to 1667 Hz for interleave group sizes of twelve and six, respectively.

A major disadvantage of beam-interleaving, which Azar *et al.* [59] tried to address using delay compensation, is the temporal mismatch which exists in each image between interleave groups. By increasing the interleave group size and/or the packet size, K, the temporal mismatch worsens. This temporal delay means that the velocity information acquired in adjacent interleave groups does not correspond to the same moment in the cardiac cycle. Thus, the overall frame-rate is still a major limitation.

3.3.2 Parallel Receive Beam-Forming

Parallel receive beam-forming is also known as multi-line acquisition (MLA). The concept behind parallel receive beam-forming is to acquire more than one scan-line from a single transmit event, depicted in figure 3.8. In the figure, two separate scanning conventions are demonstrated. In the first, scenario A, single-line

acquisition (SLA) is shown, one emission yields one received beam corresponding to a single scan-line. Scenario B shows MLA; one broad transmission allows many beams to be received in parallel, supplying an equal number of scan-lines. The frame-rate increase is equal to the number of beams received in parallel per transmit.

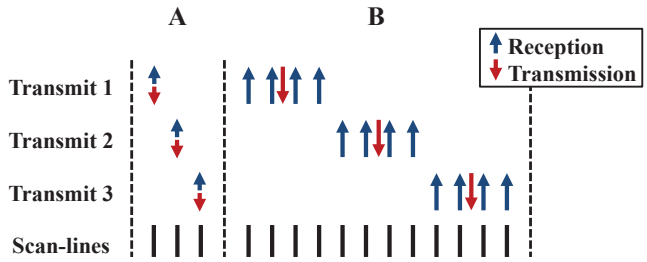

Figure 3.8: Comparison between A. single-line acquisition (SLA) and B. multi-line acqusition (MLA). In SLA, for each transmit event there will be one receive event yeilding one scan-line per receive event. Contrarily, in MLA, for each transmit event there may be many receive events (in this case four), resulting in four scan-lines per transmit. Adapted from [60].

Many proposals have been made using parallel receive beam-forming to improve the frame-rate of conventional US. Shattuck *et al.* [61] produced a device capable of obtaining four scan-lines for every transmit, effectively quadrupling the frame-rate and thus the effective PRF. Their product was validated on B-mode scans.

In [62], a four to one receive-transmit ratio was used with 2D speckle tracking to acquire the tissue motion of an *in vitro* speckle phantom and flow motion for *in vivo* scans of healthy carotid arteries. In a latter study, Bohs *et al.* [63] modified the aforementioned speckle tracking method to be more compatible with reduced hardware systems with a two to one receive-transmit ratio. They also implemented a 1D pattern matching scheme to reduce the computational load of the 2D technique.

Likewise, in [42] a broad plane-wave was emitted and two parallel apertures were recuperated and beam-formed in receive to obtain two angled perspectives for triangulation of motion components found with 1D speckle tracking for transient elastography. Similarly, Hansen *et al.* [41] use the same procedure on blood flow, with the exception of a modified transmit pulse, in which a 13 bit Barker code is

used to improve the transmit energy. Their methodology was tested *in vivo* on the bifurcated vessels of patients.

Another investigation conducted by Swillens *et al.* [39] used beam-interleaving coupled with MLA, to obtain high frame-rate 2D vector maps. In their work, effective PRFs of 2 and 4 kHz were achieved by varying the interleave group size using the formulation

$$IGS = \frac{T_{eff,prf}}{T_{prf}} \cdot L \qquad 3.4$$

where, L gives the number of beams received in parallel during MLA, which was set to two for their study. This formula suggests that, compared with regular beam-interleaving, the effective PRF is L-times higher for the same interleave group size when using MLA. Standard cross-beam VD was used to procure a 2D vector map using data collected from *in silico* validation using simulated scans of patient specific flow profiles. It was concluded that their method yielded acceptable lateral and axial velocity estimates; however, the highest velocities were still prone to aliasing.

3.3.3 Plane-Wave Ultrasound

Plane-wave US imaging is of rising interest due to its ability to provide elevated frame-rates which exceed those of other high frame-rate techniques. It is an extension of the previously describe parallel beam-forming scheme in which all elements have the ability to transmit and receive simultaneously. Over the past few years, due to technological advances, ultrasound systems have been geared with plane-wave capabilities, as processing and manipulation of large datasets can be done more quickly and efficiently. The plane-wave approach, which is addressed in the subsequent paragraphs, has been aptly labeled ultrafast imaging.

By exciting all of the transducer elements simultaneously with an identically shaped pulse, a planar wave-front is produced (see figure 3.9A). Alternately, transducer elements may be stimulated with a linear delay to tilt the planar wave-front, which allows for an angled acquisition (see figure 3.9B).

As the wave-front meets a point scatterer, the point scatterer acts as a secondary source in that it engenders a spherical echo, which returns to the transducer (figure 3.10A). The received diffraction pattern from a single scatterer takes on a hyperbolic shape. Each hyperbolic shape has a measure of eccentricity, ε, ascribed to the depth of the scatterer in the medium; the closer the scatterer is to the surface the higher the degree of declivity.

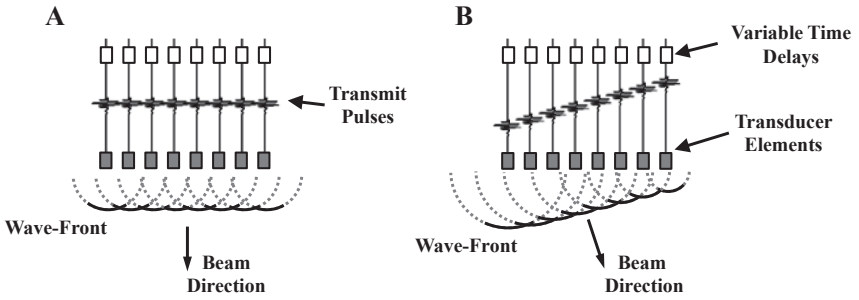

Figure 3.9: Two examples of plane-wave wave-fronts. Panel A shows the interference pattern of transmit pulses emitted simultaneous. Panel B illustrates the interference pattern of transmit pulses emitted with a linear time delay sequence to create an angled acquisition.

The raw radio-frequency (RF) data received will present an image composed of a multitude of hyperbolic echo patterns produced from a collection of randomly distributed point scatterers, simplified in figure 3.10B. In order to visualize the underlying medium correctly, each of the hyperbolic shapes must be collapsed or reconvened at their apexes (figure 3.10C).

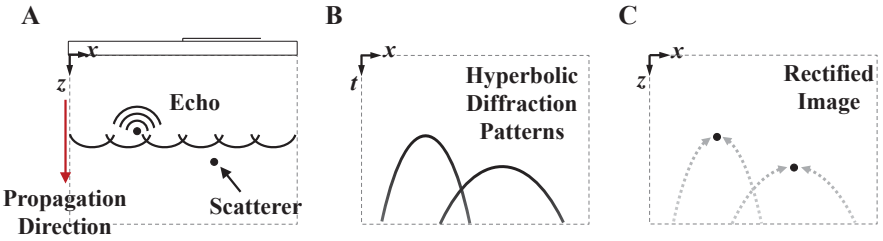

Figure 3.10: Panel A shows a plane-wave acquisitions in which a wave-front propagates into a tissue medium. The first scattering point causes an echo to return to the transducer. Panel B shows the received signal obtained by the transducers for a given travel-time. The two scattering points in panel A, produce hyperbolic diffraction patterns in panel B. Applying a method of *migration* to the data in panel B we obtain a proper representative image of the scattering medium in panel C. Adapted from figures of [64].

This post-processing step has been dubbed *migration* in the field of Seismology, and a few methods exist to fulfill the requirement [64-66]. For the purposes of this

work, we focus on the simplest approach called the *Delay-and-Sum* (DAS) method (for more details see section 4.3.1 and appendix 1), as its validity in medical ultrasound has been verified by [17, 19, 67] and it is easily implemented for reconstruction in an angled coordinate system in both transmit and receive for oriented Doppler images [19].

The DAS method is a time-space based approach which consists in convening the hyperbolic diffraction patterns to their correct position using computed travel-times set out for a wave to go to a particular scattering point and back to each of the transducer elements. This method was applied in [67], whereby the performance of the plane-wave imaging using the DAS method was evaluated based on SNR and contrast-to-noise ratio (CNR). This was done by comparing compounded plane-wave B-mode acquisitions with conventionally obtained mono-focal and multi-focal imaging. A number of tilted flash transmits received at zero degrees were coherently compounded. The number of tilts varied from 11 to 71 in order to improve the image quality. It was found that *in vitro* plane-wave imaging, using the DAS method, was able to provide frame-rates roughly ten times faster than conventional imaging while maintaining the same quality. The feasibility of detecting tissue motion, for the assessment of viscoelastic properties of *in vivo* breast tissue, was demonstrated. A related study [68] also validated the applicability of the DAS method combined with an adaptive minimum variance beam-former to improve the resolution and contrast of plane-wave B-mode images *in silico* using the Field II software.

In a study by Udesen *et al*. [17], plane-wave transmits were conducted and received at zero degrees whereby the DAS method was applied. In this method, velocity maps were found using a 2D cross correlation, for which the mean of forty maps was taken to improve the estimate. This approach was tested *in silico* and compared with a theoretical Poiseuille flow profile with realistic flow conditions. Using simulations, they compared the effect of different parameters on the standard deviation and bias of their estimates. Validation was also made using an *in vitro* Poiseuille flow phantom with two interleaved groups, i.e. two plane-

wave emissions were made, each with 64 elements, to create a full 128 element image. Finally, *in vivo* volume flow measures were compared with MRI angiography along one cardiac cycle of one healthy patient's common carotid artery.

A latter investigation [18], similar to [67], showed that indeed tilted plane-waves in transmit can be coherently summed to improve velocity estimations using the traditional phase-shift autocorrelation by Kasai *et al.* [33], compared with a series of flat non-compounded images, both received with zero angle. Results were acquired *in vitro* on a stationary flow phantom which contained an angled vessel at 18 degrees, for which angle correction was used to improve the estimate. However, it is impractical to perform angle correction for *in vivo* studies; thus, none was applied for the simple common carotid case over the cardiac cycle and conclusions were drawn based on inspection. They resolve that the same Doppler information can be exploited while achieving acquisition up to 16 times faster.

More recently, Ekroll *et al.* [19] used the DAS method on dual-angled plane-wave data (for which the angle in transmit equalled the angle in reception). In their study, blood velocity was calculated using the VD technique on dual angle acquisitions with variable ensemble lengths for the phase-shift autocorrelation method [33] ranging from eight to 50. Using *in silico* Field II data of patient specific carotid bifurcations, they found that by increasing the ensemble size there was a significant decrement in error. Ekroll *et al*. further examined Couette flow *in vitr*o to observe a slow moving tissue target. They then imaged patients with diseased carotid arteries *in vivo*. However, this study does not compare the performance of their single-angle imaging convention with the previously mentioned tilted-compound imaging method proposed by Bercoff *et al*. [18].

3.4 Project Objective

The goal of this project is to implement and investigate vector flow mapping using plane-wave ultrasound imaging. Since plane-wave acquisitions are known to

provide poor penetration depth and resolution compared with conventional colour-Doppler imaging [67], it is of interest to use a robust method of reconstruction.

The phase-shift autocorrelation estimation method with dual angle triangulation, used in this study and otherwise known as vector-Doppler (see section 3.2.3), was demonstrated to perform more consistently under low signal-to-noise ratio and at variable depths compared with time-shift estimation methods (refer to section 2.3.3) [39]. Vector-Doppler is also less computationally demanding. Of the aforementioned studies, two employ plane-wave imaging post-processed using the delay-and-sum method and the conventional phase-shift autocorrelation estimation method; those studies were done by Bercoff *et al*. [18] and Ekroll *et al*. [19].

More specifically, Bercoff *et al*. [18] used a coherently-compounded scanning convention, shown later in figure 4.4B. They obtained images at a single orientation of $\beta = 0°$, with a variable number of tilted angles (N), which they then compared with conventional focused Doppler imaging to evaluate their method. The other study, by Ekroll *et al*. [19], used the scheme later demonstrated in figure 4.4A. They used the full vector-Doppler technique by obtaining oriented ensembles with no tilted compounding. Each beam corresponded to one image in the Doppler ensemble (K), which was varied in length. Since these two studies differ in their methodology, this project applies both methods to allow for a basis of comparison.

Furthermore, of consequence to the phase-shift autocorrelation estimation method is the emitted pulse length (mentioned in section 1.2.3.b). The autocorrelation method is a narrowband estimator which works ideally for comparably longer pulse lengths to broadband estimators (see section 2.3.3). Conventional Doppler imaging uses pulses with 5 to 20 cycles (typically 8) at the central frequency [22, 69]. Contrary to preference given to longer pulse when employing the autocorrelation technique, these two studies have used 2.5 [19] and 3 [18] cycles per transmit pulse without justification. This parameter will also be tested in this project.

Lastly, the Doppler angle is investigated at different flow-rates to see the effect of various angles on the reconstruction accuracy. In the study by Bercoff *et al*. [18], a single beam-steering angle (β = 0°) was tested with a vessel oriented at 18°. Inasmuch as the orientation of the blood vessel cannot be predicted and may lie parallel to the scanning surface, beam-steering is a more logical solution and is employed here to test the results of different Doppler angles.

In summary the objectives of this project are to acquire plane-wave data using *in vitro* experimentation, and to test different parameters on the velocity field reconstruction, which employs the delay-and-sum method and vector-Doppler. The specific objectives are to investigate the effects of four parameters on the accuracy of the velocity vector maps: number of tilts per oriented compound image (N), Doppler ensemble length (K) using a single tilted imaging scheme, number of cycles per pulse transmission, and reconstruction angle (β) for various flow-rates. The intention of this project is to improve blood velocity estimation by determining the optimal conditions under which velocity imaging, using plane-wave ultrasound, should be implemented.

Chapter 4 : Materials and Methodology

To meet the proposed objectives, results were obtained through *in vitro* experimentation as described below. Plane-wave ultrasound acquisitions were taken following the protocol provided in later sub-sections, followed by post-processing, including rectification of plane-wave diffraction patterns, velocity estimation and vector flow mapping.

4.1 *In Vitro* Steady Pipe Flow Experimental Setup

The experimental pipe flow setup, subsequently described, was constructed as shown in figure 4.1.

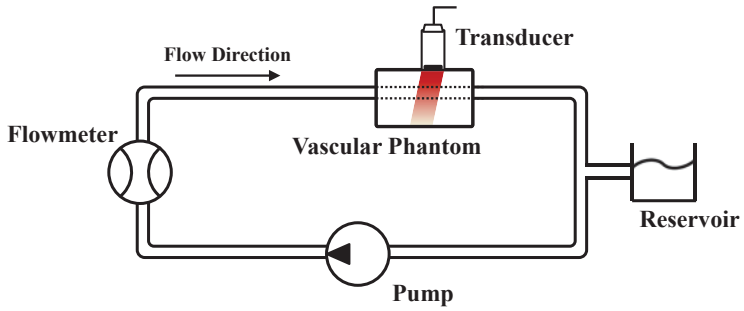

Figure 4.1: Hydrodynamic stationary flow experimental setup.

A variable speed pump (Cole-Parmer, Inc., Canada) was used to circulate blood mimicking fluid through the system. The blood mimicking fluid was custom made using glycerol and water to produce a solution with a dynamic viscosity of roughly 3.5 mPa·s (see figure 4.2), similar to that of blood [70-72], as measured by means of a low shear viscometer (LS300, proRheo GmbH, Germany).

Cellulose (Sigmacell, Sigma Chemical Co., St. Louis, U.S.A) was added to simulated blood scatterers at 1 $g \cdot L^{-1}$. To ensure that the blood mimicking solution was indeed a Newtonian fluid, which conforms to the characteristics Poiseuille flow, the shear stress was measured in response to variable shear rate (see figure 4.3) demonstrating a constant rate of change.

The flow-rate of the circulating flow was measured with a low-flow magnetic flow-meter (Omega Engineering, Inc., Canada) before entering a straight cylindrical passage to a tissue mimicking phantom (model 525, ATS Laboratories, Inc.) specifically designed for ultrasound flow measurements. The ultrasound flow phantom included a tube of 3.8 mm radius at a depth of roughly 15 mm.

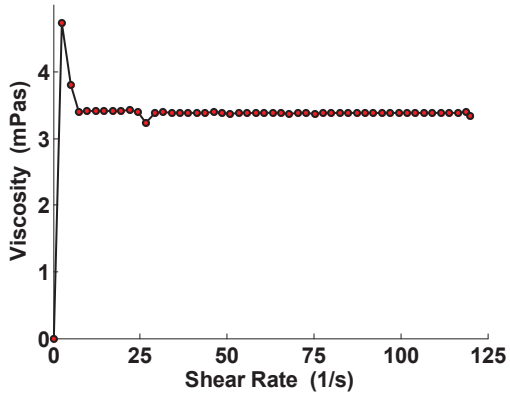

Figure 4.2: Dynamic viscosity of the blood mimicking fluid for variable shear rate. Apart from the anomalous data due to instrumentation at very low shear rates, the viscosity remains constant at 3.5 mPa·s.

The flow introduced to the phantom for measurement was first passed through a straight equi-diameter entrance length of approximately 120 cm to ensure fully developed laminar flow (Re<2000) within physiological conditions. Upon exiting the phantom the flow was returned to a fluid reservoir.

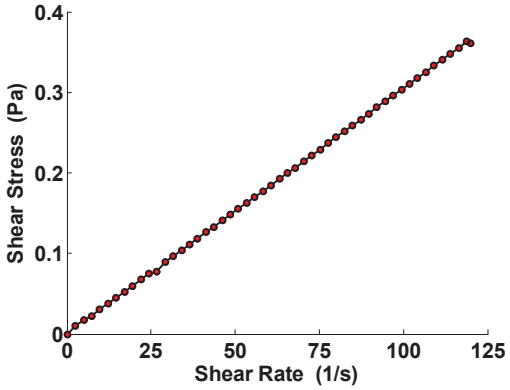

Figure 4.3: Proportional rise in shear stress of the blood mimicking fluid with increasing shear rate indicative of a Newtonian fluid.

During experimentation, three different volumetric flow-rates were used: 0.55, 0.80 and 1.00 $L \cdot min^{-1}$, which fit in the range of possible flow-rates experienced in

the human common carotid arteries. In one study [73], a mix of 43 healthy and unhealthy (symptomatic or asymptomatic) patients from 42 to 80 years of age had their common carotid artery volumetric flow-rates measured using Doppler ultrasound. A range of flow-rates between 0.338 and 0.942 $L \cdot min^{-1}$ were found with a mean of 0.636 ± 0.154 $L \cdot min^{-1}$. In another study [74], volumetric flow-rates were measure using phase sensitive MR imaging on 6 volunteers, 2 normal and 4 abnormal, a larger range of 0.171 to 1.182 ± 0.040 $L \cdot min^{-1}$ was found. Other studies show similar results [75, 76].

To acquire ultrasound measurements, the transducer probe was aligned longitudinally and fixed at the center of the tube to obtain the centerline velocity profile which theoretically corresponds to the Poiseuille flow velocity profile shown here,

$$v(r) = v_{\max}(1 - (r / r_{\max})^n) \qquad 4.1$$

where, v denotes the velocity with respect to radial position, r, r_{max} is the radius of the phantom vessel, v_{max} is the maximum velocity dictated by the measured flow-rate, and n is the shape factor of the profile which is equal to two for parabolic flow.

Since the mock vessel ran parallel to the surface of the phantom, the probe was aligned perpendicular to the flow. As demonstrated in case B of figure 3.1, this transducer-flow alignment is the worst case scenario for velocity estimation. Furthermore, this configuration resembles conditions which may be encountered in clinical practice, as the carotid arteries are aligned approximately parallel to the body surface.

4.2 Acquisition Protocol

Acquisition of the data was done using a customized sequences programmed using a Verasonics ultrasound scanner (V-1-128, Verasonics Inc., Redmond, WA). These scans were performed using one of two plane-wave conventions (expounded for each case in chapter 5): a consecutive series of K constant β-angled acquisitions both in transmit and reception (shown in figure 4.4A and used

by Ekroll *et al*. [19]); and a repetitive series of *K* images each composed of *N* α-tilted acquisitions in transmit with a constant angle of reception β, where the angle α varies about β in incremental tilts of 1° (shown in figure 4.4B and employed by Bercoff *et al*. [18]). The rate of acquisition of these two approaches differ in that the imaging rate of the first scheme is equal to the pulse repetition frequency, whereas the second scheme has an imaging rate of the pulse repetition frequency divided by the number of *N* tilts. Despite the Verasonics reception at zero degrees, adjustment was done in post-processing (refer to section 4.3.1) to reconstruct the data in a β-oriented coordinate system.

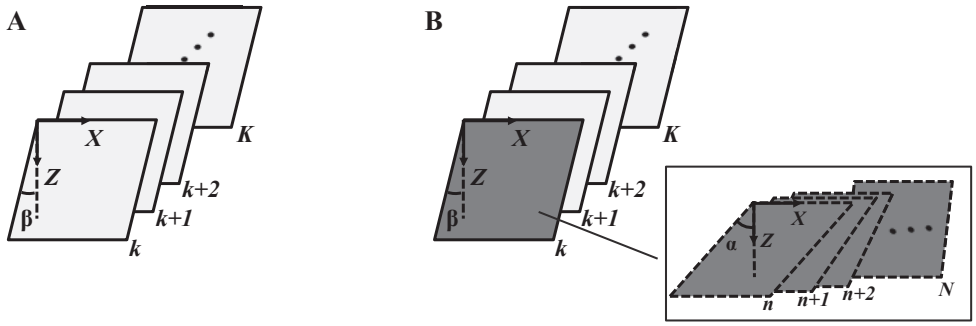

Figure 4.4: Two conventions of plane-wave acquisition. Panel A. without tilted compounding (used by Ekroll *et al*. [19]) and panel B. with tilted compounding (used by Bercoff *et al*. [18]).

Using a linear transducer with a 3 MHz bandwidth from 4 to 7 MHz (L7-4), emitting at a central frequency of 5 MHz and acoustic propagation speed of 1540 $m \cdot s^{-1}$, plane-wave emissions were created. In transmit, linear time delays were prescribed to each element of the transducer, using the programmed sequences, to accommodate for the corresponding plane-wave beam angle. In reception, four samples per wave were collected yielding a sampling frequency of 20 MHz.

The pulse repetition frequency was adjusted to adapt for various flow conditions, maintaining detectability of an optimal velocity range according to (2.8) and (2.9). Other acquisition parameters were also varied such as the number of tilts (*N*) per oriented image, the number of pulse cycles per emission, the length of the ensemble (*K*) from which the Doppler velocities were calculated, as well as Doppler angle (β).

The acquisition protocol was repeated for alternating positively and negatively oriented sequences (demonstrated in figure 4.5), in order to obtain two velocity components at each spatial location in the target velocity field. This is described in more detail in section 4.3.3.

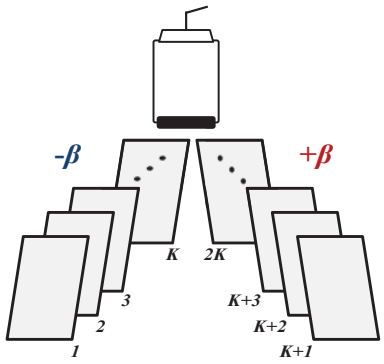

Figure 4.5: Alternating dual angle acquisition protocol. A series of K negative β-angled acquisitions are obtained, directly followed by K positive β-angled acqusitions to provide two oriented 1D components of the flow.

4.3 Post-Processing

After procuring a time series of plane-wave acquisitions as described in the previous section, three major veins of post-processing were performed offline using custom-made scripts programmed in MATLAB (MathWorks, Inc.): rectification of the unfocused plane-wave images using the delay-and-sum (DAS) method and compounding if necessary; correlation between successive images using a phase-shift autocorrelation; and finally vector flow mapping. These three steps are described in the following sub-sections.

4.3.1 Rectification of Plane-Wave Images

In this work, the DAS method was used to correct the hyperbolic echoes in plane-wave images. This method was chosen due to its demonstrated functionality [67] and ease of implementation for angled acquisitions in transmit and reception [19].

The DAS method uses calculated travel times to correct the hyperbolic diffraction patterns of raw plane-wave data, in order to create a proper image. These travel-times, in transmit and receive, correspond to the time taken for the plane-wave

wave-front to reach a scatterer at location (x', z'), and then, for the spherical echo to return to the transducer (see figure 4.6).

Each adjacent element of the transducer receives the echo with a given delay, with respect to the initial arrival, creating the hyperbolic form. By looking to the schematic in figure 4.6, the travel-times in emission and reception are displayed. A full derivation of the resulting equations, (4.2) and (4.3), is provided in appendix 1.

Using trigonometric identities, the travel-time in transmit, τ_{TX}, can be obtained from panel A, and expressed in the following way,

$$\tau_{TX} = \frac{x' \cdot \sin\alpha + z' \cdot \cos(\alpha - \beta)}{c} \quad . \qquad 4.2$$

where x' and z' represent the lateral and axial location in an oriented coordinate system, α and β are the angles in emission and reception, and c is the wave propagation speed.

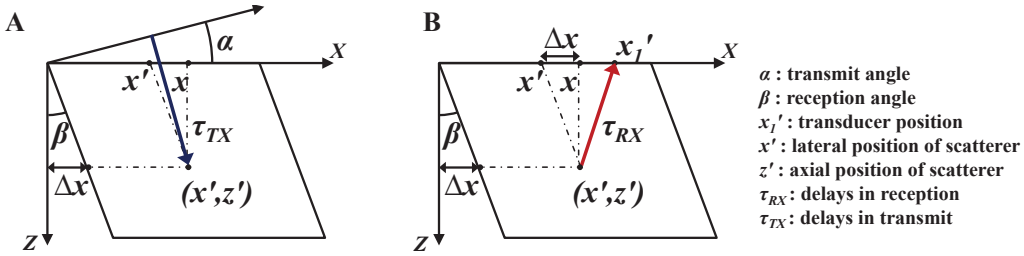

Figure 4.6: The travel times in transmit (panel A) and receive (panel B) for plane-wave imaging in an oriented coordinate system. The blue arrow represents the travel time required in transmission, τ_{TX}, to reach a particular point (x', z') for a given transmit angle, α. The red arrow represents the time required in reception, τ_{RX}, to return from that point to a transducer position x_1' for a given receive angle β . Modified from [67].

From panel B (figure 4.6), the travel-times in reception, τ_{RX}, can be expressed as a function of the oriented coordinates and receive angle as follows,

$$\tau_{RX} = \frac{\sqrt{z'^2 + (x_1' - x')^2} - z' \cdot (x_1' - x') \cdot 2\sin\beta}{c} \quad . \qquad 4.3$$

where x_1' defines the lateral location of a particular receiving element. The total travel-time τ in transmission and reception is given by $\tau = \tau_{TX} + \tau_{RX}$.

4.3.2 One-Dimensional Doppler Velocities

A two part procedure is undertaken to determine the one-dimensional Doppler velocities from the rectified radio-frequency ultrasound data. The first part involves in-phase quadrature demodulation, and the second part makes use of clutter filtering and a phase-shift autocorrelation method proposed by Kasai *et al.* [33].

4.3.2.a Radio-Frequency to In-phase Quadrature Data

In-phase quadrature demodulation, in itself, requires three main steps: down-mixing, low-pass filtering and decimation. Figure 4.7 depicts these steps.

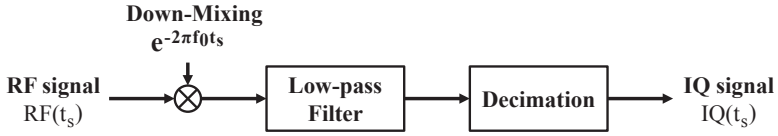

Figure 4.7: Conversion of a radio-frequency (RF) signal, acquired with respect to the sample time t_s, to in-phase quadrature (IQ) data. Modified from [30].

Down-mixing (for more details refer to section 2.2.3) is enacted through multiplication of the lines of received radio-frequency data by a complex exponential function, with a frequency equal to the central frequency of the emitted signal, in this case 5 MHz. In doing so, the entire spectrum is shifted down so that the positive end of the frequency spectrum is brought to baseband (refer to figure 2.2). The resultant signal becomes complex and asymmetric about zero.

Since the positive spectrum has been shifted to baseband, a low-pass filter is then applied. Low-pass filtering allows the removal of the negative portion of the original radio-frequency spectrum, as well as undesirable frequencies barring those which lie within the bandwidth limits. The L7-4 transducer used in this work, has a bandwidth which ranges from 4 to 7 MHz, which when shifted to baseband has an asymmetric spectrum range from -1 MHz to 2 MHz. A cut-off frequency of half of the bandwidth (1.5 MHz) was used to maintain the important frequency content in the signal.

Finally, because the frequency content has been shifted to baseband and filtered, according to the Nyquist theorem, the sampling frequency may also be reduced to twice the cut-off frequency of the low-pass filter, i.e. the highest frequency content. In this case, the sampling frequency maybe reduced from 20 MHz to 3 MHz. In order to do this, the signals were decimated by keeping every sixth sample.

4.3.2.b In-phase Quadrature to One-Dimensional Velocity Data

In this part, two tasks were undertaken: clutter filtering and the phase-shift estimation introduced by Kasai *et al.* [33]. Clutter filtering (refer to section 2.3.4) is a high-pass filter applied to the slow-time IQ signal (defined in section 2.3) to remove high amplitude low frequency content attributed to near stationary tissue which may suppress the blood velocity during estimation. Clutter filtering was done using a third order high-pass Butterworth digital filter as in [71, 77, 78] with a 70 Hz cut-off frequency [79].

Thereafter, the phase-shift estimation was used to provide an axial velocity estimate for each spatial sample over the series of complex IQ signals. Details concerning this method of estimation are furnished in section 2.3.2.a. In summary, the following expression was applied,

$$V_z = \frac{c}{4\pi f_0 T_{prf}} \arctan\left(\frac{\sum_{k=1}^{K} Q(k)I(k-1) - Q(k-1)I(k)}{\sum_{k=1}^{K} I(k)I(k-1) - Q(k-1)Q(k)} \right) \quad . \qquad 4.4$$

where c is the speed of acoustic propagation, f_0 is the emitted central frequency, T_{prf} is the pulse repetition period, $I(k)$ and $Q(k)$ represent the in-phase and quadrature components of the k^{th} signal in a series of K signals.

4.3.3 Two-Dimensional Vector Flow Mapping

A 2D vector flow map was performed by reconstructing 1D velocity projections from two sets of coplanar alternating-angled Doppler measurements. Figure 4.8A shows the alternating course of scan which produces the 1D projections, V_p and V_n obtained from positive and negative β-angled scans.

Using the two 1D Doppler velocity images, i.e. the positive and negative angle projections in the oriented Doppler basis (figure 4.8B), one 2D velocity image was recomposed to a common Cartesian coordinate system (figure 4.8C) using the VD technique. A full derivation of the lateral and axial velocities, V_x and V_z, is provided in appendix 2. In summary, the lateral and axial velocity components were calculated using (4.5) and (4.6), respectively.

$$V_x = \frac{V_n - V_p}{2\sin\beta} \qquad 4.5$$

$$V_z = \frac{V_n + V_p}{2\cos\beta} \qquad 4.6$$

Thereafter, regularization was applied to alleviate the dataset of incongruous contributions such as noise or outlying vectors. Expressly, an user-independent, discrete cosine transformed based penalized least squares approach, proposed by Garcia [80], was used.

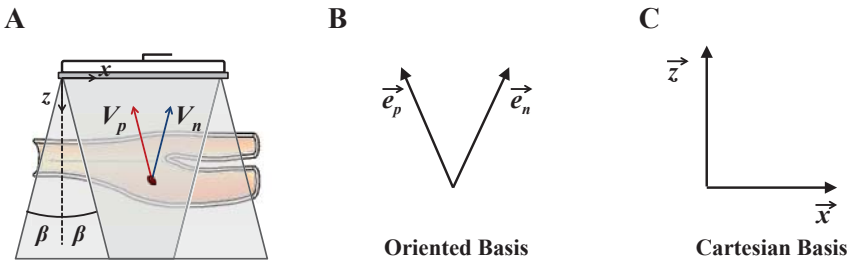

Figure 4.8: A. Two coplanar β-oriented acqusitions with positive and negative velocity projections. B. Oriented basis for the two 1D measured Doppler velocities. C. Cartesian basis in which the velocity projections are resolved.

Chapter 5 : Results

This chapter consists of four sections, which present the results reaped from the methodology, described in the antecedent chapter. The four sections examine the effects of variations in the number of tilts per oriented image (N), length of the Doppler ensemble (K), number of cycles per transmit pulse, and the reconstruction angle (β) for different flow-rates, on the accuracy of velocity vector map.

5.1 Variation in the Number of Tilts per Orientation

Using the acquisition protocol depicted in figure 4.4B (with tilted compounding), the number of tilts (N) used to create each oriented image was varied from 1 to 9 in increments of 2. The acquisition parameters are summarized in table 5.1. The frame rate is given by the effective pulse repetition frequency divided by two, where two represents the dual angle (positive and negative) acquisition required for 2D vector mapping.

Table 5.1: Acquisition parameters used to compare the results of velocity vector mapping subject to a variable number of compounded tilted images per orientation.

Parameter	Value
Flow rate (L/min)	0.8
f_0 (MHz)	5
f_s (MHz)	20
c (m/sec)	1540
Cycles at f_0	2.5
Angle (°)	±15
Numer of elements	128
N (number of tilts)	1, 3, 5, 7, 9
Ensemble Length	12
Number of firings	12, 36, 60, 84, 108
Effective PRF (Hz)	1700 Hz
Frame rate (fps)	850

As shown in figure 5.2 and figure 5.3, as well as in subsequent sections, the lateral and axial profiles from the reconstructed 2D velocity maps were evaluated separately against the lateral and axial components of the reference Poiseuille flow profile, based on the flow-rate imposed during experimentation. Since the experimental flow was stationary, the velocity was only dependent on depth and

constant in the lateral direction. Thus for each sample in depth, the mean and standard deviation across all the elements was plotted for both lateral and axial components to obtain the velocity profiles. It should be noted that only the velocity components inside the triangulation zone, i.e. the intersection between the positively and negatively oriented images (refer to figure 5.1A for clarification), were considered in this section and those which follow.

Figure 5.1: A. The intersection between positively and negatively oriented images. The black outline indicates the full triangulated region. Measures involving the full zone of triangulation are noted plainly by V_x and V_z. B. A bounded region within the triangulation zone delimiting velocities in the local flow vacinity. Measures involving the local flow region are noted with the addition of an asterisk as V_x* and V_z*.

For each component, V_x and V_z, the normalized root-mean-squared error (NRMSE), defined by (5.1) was also calculated to provide a quantitative measure of residual deviation between the experimental and theoretical velocity profiles.

$$NRMSE = \sqrt{\frac{\sum_{i=1}^{p}\left(V_{theo_i} - V_{\exp_i}\right)^2}{p}} \Bigg/ V_{\exp,\max} \qquad 5.1$$

In the preceding equation, p is the total number of samples in the imaged region, V_{theo_i} and V_{exp_i} are the reference and observed velocities of the ith sample, and $V_{exp,max}$ give the maximum limit of the observed velocity range in the imaged region.

Concerning the lateral velocity profiles shown in figure 5.2A-E, particularly in the vicinity of the pipe flow, the closeness of fit between the estimated and theoretical profiles seems to improve significantly as the number of tilts increase, up to 5 tilts per image and then slowly improves from there. This is consistent with the two decreasing trends shown in the normalized root-mean-squared errors displayed in figure 5.2F. The large approximately zero-velocity background in the velocity

maps effectively lowers the mean residual of normalized root-mean-squared error. Therefore, it was of interest to calculate both the error in the full image (shown in figure 5.1A) and also the error in the local flow region (shown in figure 5.1B).

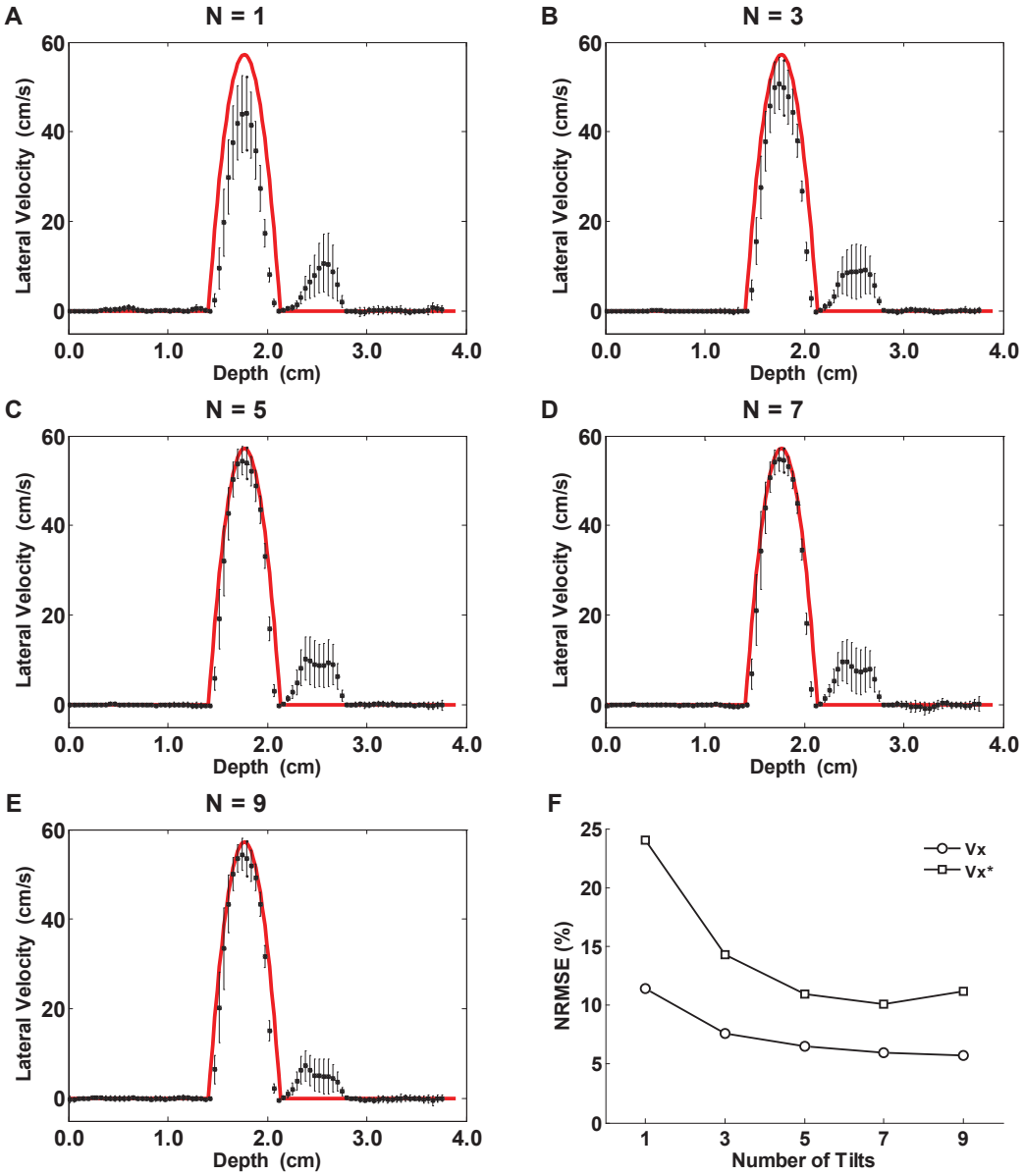

Figure 5.2: Panels A to E show the average lateral velocity profile as a function of depth. Each panel differs in the number of tilted firings used to compose each oriented image. The red curve provides the theoretical profile overlayed with the experimental profile, in black. Each vertical black bar indicates the standard deviation over each row (for all transducer elements) in the image. Panel F expresses the normalized root-mean-squared error (NRMSE) as a function of the number of tilts. V_x indicates that all lateral velocities in the triangulation region were used in the assessment. V_x* indicates that only the lateral velocities in the vicinity of the flow, from a depth of 1.36 cm to 2.16 cm were used.

As expected, the normalized root-mean-squared error over the entire image was less, for each case, compared with error calculated for the region encompassing the flow exclusively.

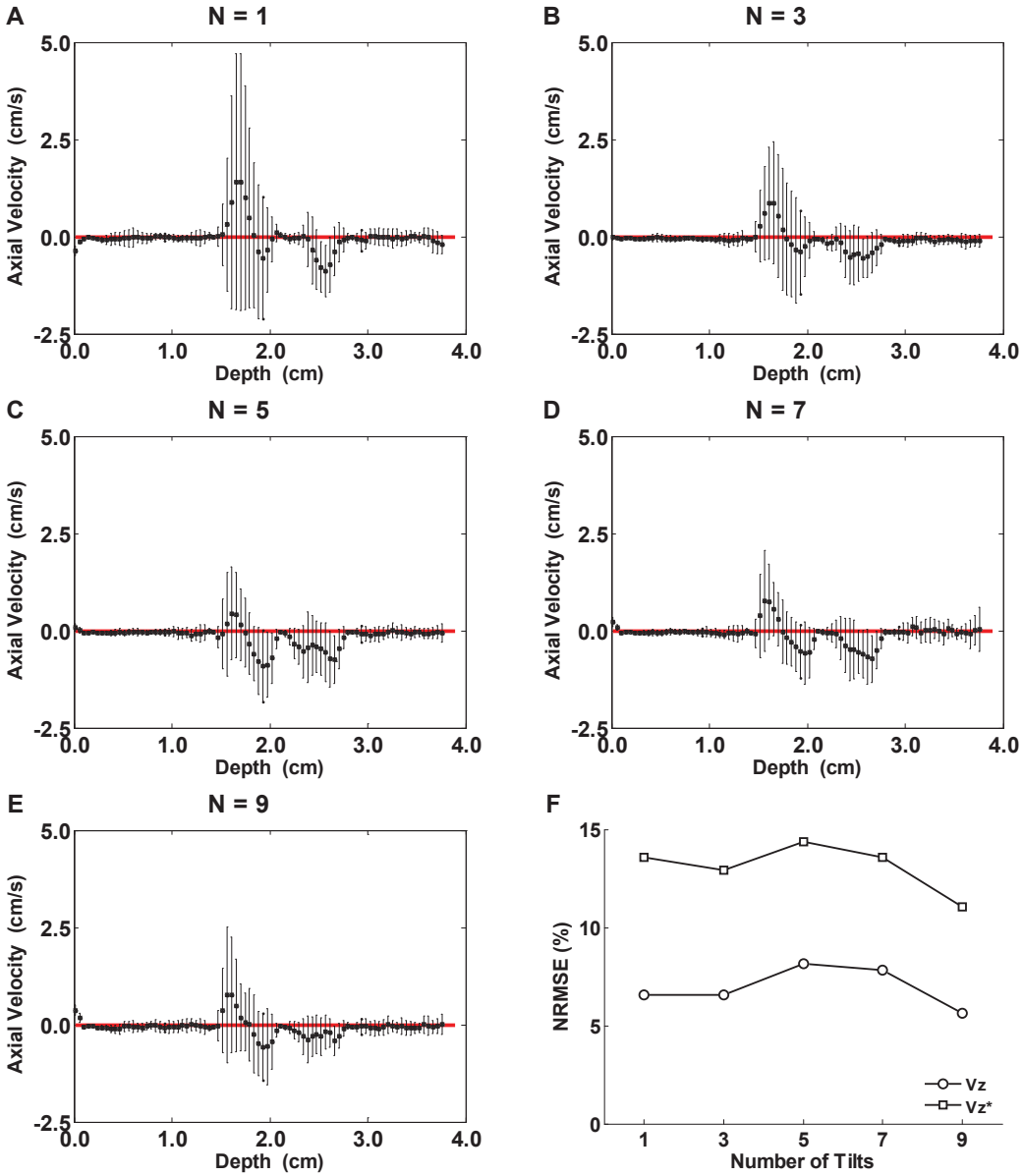

Figure 5.3: Panels A to E show the average axial velocity profile as a function of depth. Each panel differs in the number of tilted firings used to compose each oriented image. The red curve provides the theoretical profile overlayed with the experimental profile, in black. Each vertical black bar indicates the standard deviation over each row (for all transducer elements) in the image. Panel F expresses the normalized root-mean-squared error (NRMSE) as a function of the number of tilts. V_z indicates that all axial velocities in the triangulation region were used in the assessment. V_z* indicates that only the axial velocity components in the vicinity of the flow, from a depth of 1.36 cm to 2.16 cm were used.

When considering the full triangulated region the error ranged from roughly 6% to 11% error, at which the minimum occurred at about 7 to 9 tilts per image. In the local area of the flow, the error ranged from 10% to 24%, with a minimum for 7 tilts per image. A noteworthy remark is the significant drop in error (from roughly 24 to 14%) by simply increasing the number of tilts from 1 to 3 per image.

Additionally, the standard deviation in the estimate across the lateral direction at each depth, indicated by the black vertical bars also seems to decrease with an increasing number of tilts per image. Consistently lower variation is demonstrated outside the region of the pipe. Contrarily, each of the profiles display irregularities between 2 and 3 cm in depth, whereby each of the profiles deviate from the reference by roughly 5 to 10 $cm \cdot s^{-1}$.

With respect to the axial velocity estimates exhibited in figure 5.3A-E, each of the five scenarios show roughly similar tendencies. Inside the region of the flow and the aforementioned anomalous region, higher variations are seen. In figure 5.3F, the normalized root-mean-squared error in the axial component over the full triangulated region varies little and reaches a minimum error of 5.5% for 9 tilts per image. Slightly greater error was found in the local vicinity of the flow which was lowest at 11% error, also for 9 tilts per image.

In figure 5.4, and in upcoming sections, the mean standard deviation and mean bias were plotted for both the lateral and axial components separately. Standard deviation was calculated using the conventional formulation over each row in the image as follows,

$$STD = \sqrt{\frac{\sum_{i=1}^{ne}\left(V_{\exp_i} - \overline{V}_{\exp}\right)^2}{ne-1}} \qquad 5.2$$

where, *ne* is the total number of samples in each row (equivalent to the number of transducer elements), V_{exp_i} is the experimentally determined velocity at the i^{th} sample and $\overline{V}_{exp}$ indicates the mean experimental velocity, of the particular row. The mean standard deviation was computed by taking the mean value over all rows.

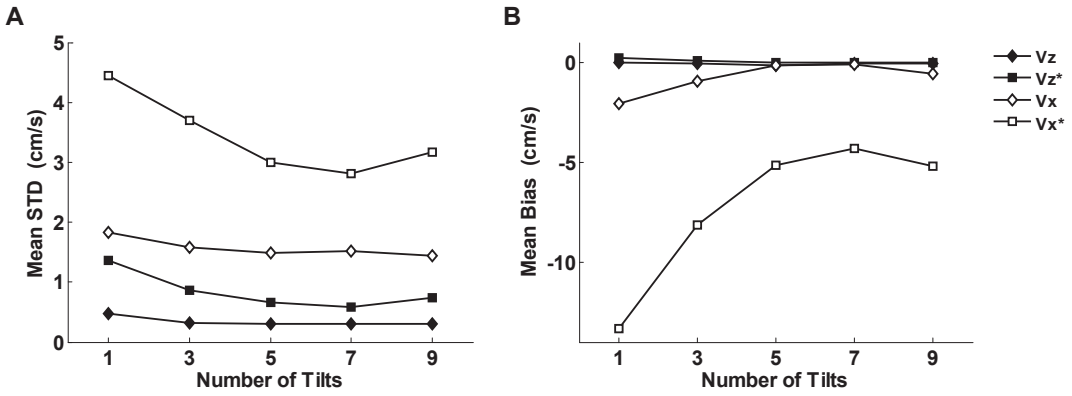

Figure 5.4: Panels A and B demonstrate the mean standard deviation (STD) and mean bias in the velocity estimates of the axial and lateral velocities, for a given number of tilts. V_z and V_x indicate that all velocities in the triangulation zone were used. V_z* and V_x* indicate only velocities in the vicinity of the flow were used, from 1.36 cm to 2.16 cm in depth.

Equation (5.3) was used to calculate the mean bias, again for the lateral and axial velocities independently. The residual difference, between the mean value of the reconstructed velocities, $\overline{V}_{exp_i}$, and the corresponding theoretical velocity, V_{theo_i}, were computed for each of the *nr* rows in the image. The mean bias over all the rows was then determined.

$$\overline{Bias} = \frac{\sum_{i=1}^{nr}\left(\overline{V}_{\exp_i} - V_{theo_i}\right)}{nr} \qquad 5.3$$

Panel A of figure 5.4, shows that the mean standard deviation in the flow locale, for both lateral and axial velocity components, is higher than the values obtained over the full triangulation zone in the image.

The mean lateral standard deviation over the full image ranged between 1.45 and 1.80 cm·s^{-1} compared to 2.80 and 4.45 cm·s^{-1} in the bounded flow region. Likewise, the mean axial standard deviation over the full image ranged from 0.30 to 0.45 cm·s^{-1} compared with 0.58 to 1.45 cm·s^{-1} in the flow-bounded area. Furthermore, with regards to the estimates in the direct vicinity of the flow, both components of velocity show a decrease in standard deviation as the number of tilts increased up to 7 tilts per image, for which a minimum was reached.

With respect to bias, the axial estimate over the entire image and in the localize flow region were roughly equal and in the range of -0.20 and 0.10 cm·s^{-1}. A more telling account of the effect of the number of tilts can be seen in the results of the mean lateral bias curve, especially in the delimited flow zone. By increasing the number of tilts from 1 to 3 the mean bias goes from -13.30 to - 8.10 cm·s^{-1}, and reaches a minimum mean bias of -4.28 cm·s^{-1} when 7 tilts per image are employed. In another light, the mean bias ranges from 23.2% to 7.5% of the maximum lateral velocity. The negative sign on the mean bias points out that indeed the velocity estimate underestimates the theoretical profile, consistent with the lateral velocity profiles plotted in figure 5.2A-E.

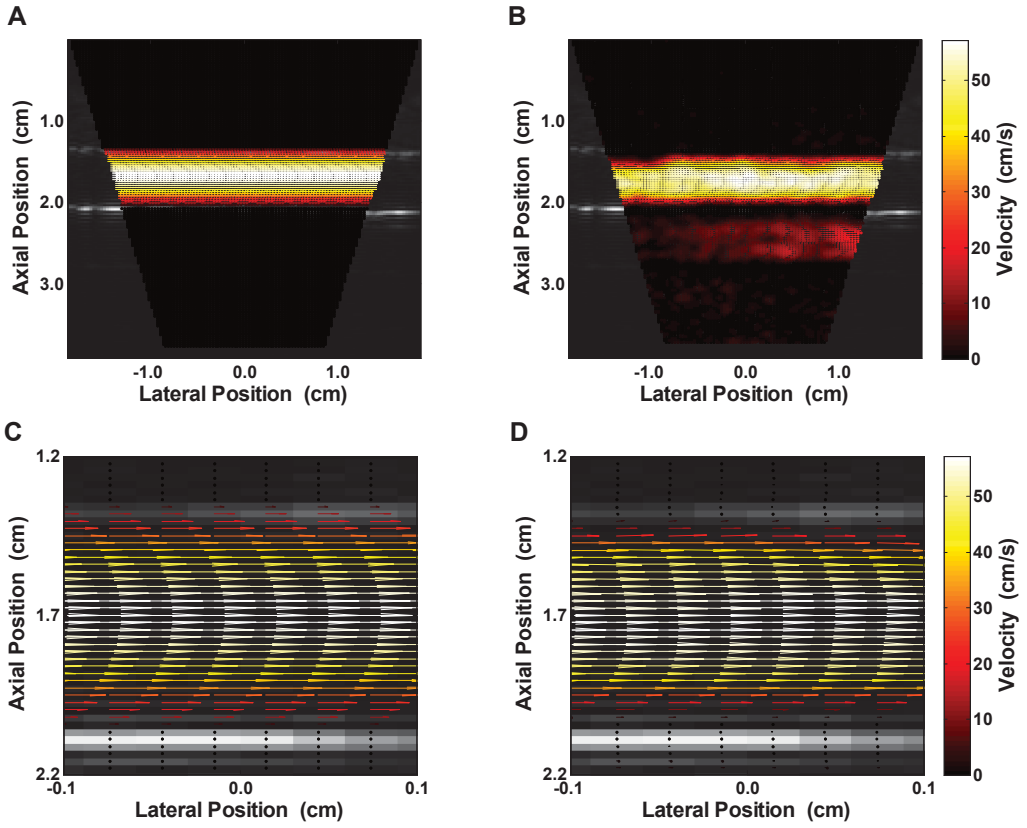

Figure 5.5: Vector flow mapping showing the magnitude and direction of the flow. Panel A shows the full theoretical velocity profile. Panel B shows the experimentally determined flow profile obtained using the parameters in table 5.1 with 7 tilts per image. Panel C and D are zoomed depictions of panels A and B, repectively.

An additional factor which helps account for the significant decrement in the magnitude of the bias, when considering the full image compared with the local vicinity of the flow, is the positive bias contribution of the aberrant vectors located between 2 and 3 cm, in depth.

Overall, by taking into consideration the normalized root-mean-squared error, mean standard deviation and mean bias, the optimal estimate comes from the imaging configuration with 7 tilts per image. Figure 5.5 exhibits the vector flow map of an acquisition with 7 tilts per image. Qualitatively, the experimental profiles in panels B and D are accurate reconstructions of the theoretical profiles shown in panels A and C. The zoomed vector maps clearly show the susceptibility of the estimation method to underestimation bias.

5.2 Variation in the Ensemble Length of Single Tilt Acquisitions

To check another imaging convention, the acquisition protocol depicted in figure 4.4A (without tilted compounding) is used. Reconstructions using ensemble lengths of 10, 15, 20, 25 and 50 images per estimation were tested. The acquisition parameters are summarized in table 5.2.

Table 5.2: Acquisition parameters used to compare the results of velocity vector mapping subject to a variable ensemble length for single tilt reconstructions.

Parameter	Value
Flow-rate (L/min)	0.8
f_0 (MHz)	5
f_s (MHz)	20
c (m/sec)	1540
Cycles at f_0	2.5
Angle (°)	±15
Numer of elements	128
N (number of tilts)	1
Ensemble Length	10, 15, 20, 25, 50
Number of firings	10, 15, 20, 25, 50
Effective PRF (Hz)	1700 Hz
Frame-rate (fps)	850

In figure 5.6A-E, the experimental lateral velocity component was plotted against the theoretical Poiseuille velocity profile, dictated by the experimental flow-rate, for variations in ensemble length. As the ensemble length increased from 10 through to 25, the estimate seems to have improved by approaching closer to the

theoretical profile. From the plots of the normalized root-mean-squared error on the lateral velocities in figure 5.6F, the error for the full image varied from approximately 9.6% to 12.5%, with a minimum for an ensemble length of 25.

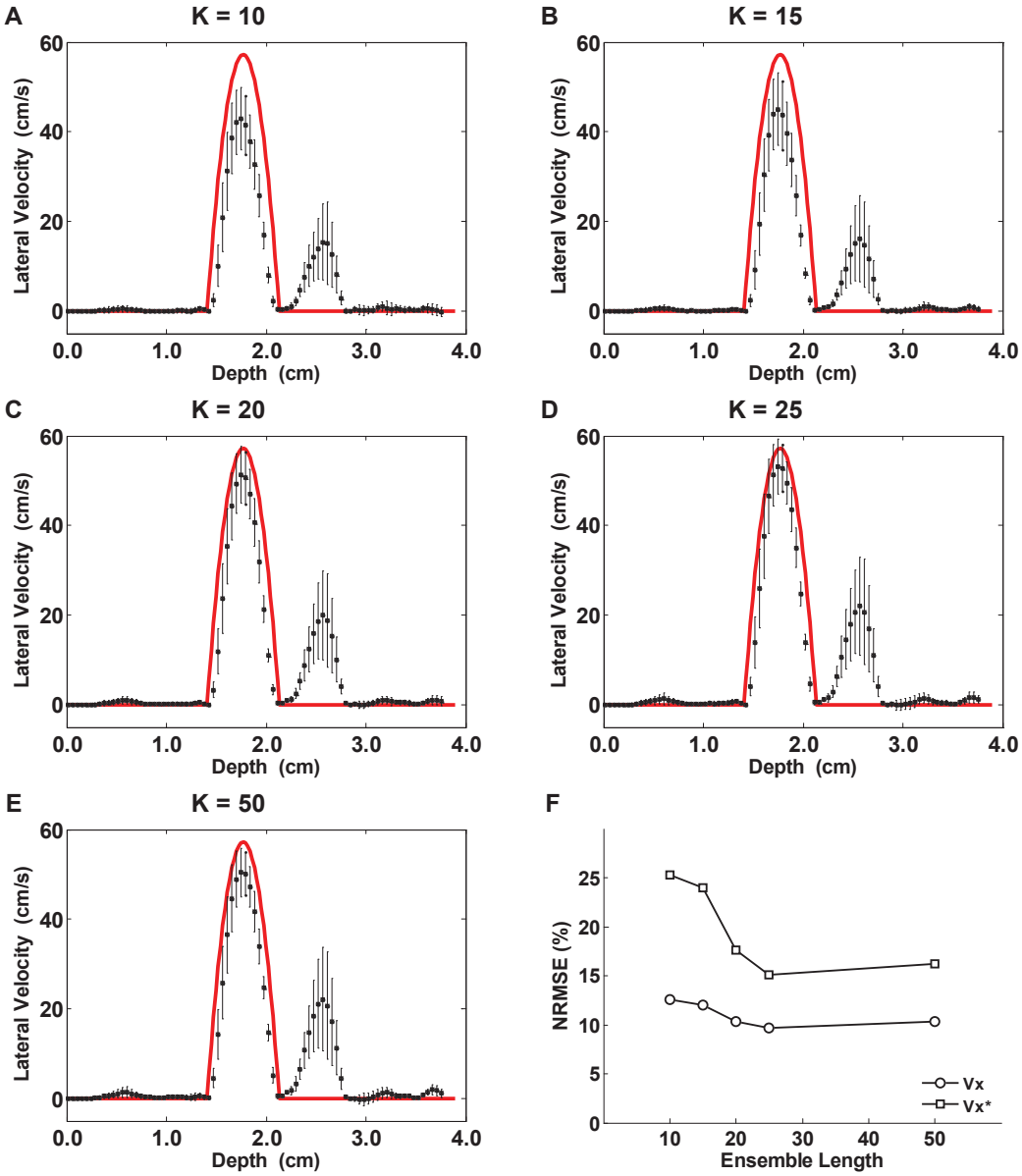

Figure 5.6: Panels A to E show the average lateral velocity profile as a function of depth. Each panel differs in the single tilt ensemble length used for velocity estimation. The red curve provides the theoretical profile overlayed with the experimental profile, in black. Each vertical black bar indicates the standard deviation over each row (for all transducer elements) in the image. Panel F expresses the normalized root-mean-squared error (NRMSE) as a function of the ensemble length. V_x indicates that all lateral velocities in the triangulation region were used in the assessment. V_x* indicates that only the lateral velocity components in the vicinity of the flow, from a depth of 1.36 cm to 2.16 cm were used.

A large contribution to the error is the irregularity in the velocity profile (between 2 and 3 cm), as was seen in the previous section, figure 5.2.

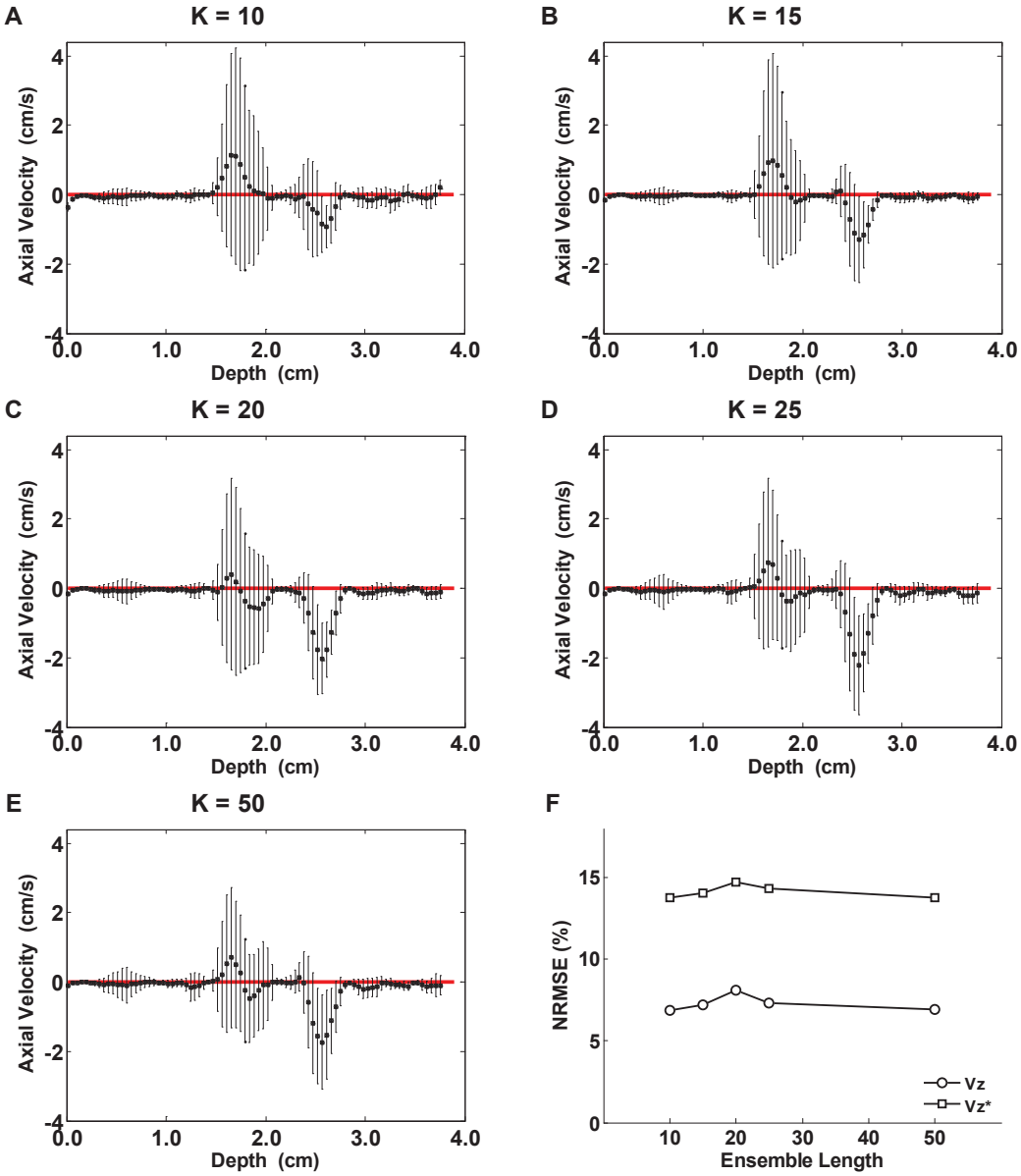

Figure 5.7: Panels A to E show the average axial velocity profile as a function of depth. Each panel differs in the single tilt ensemble length used for velocity estimation. The red curve provides the theoretical profile overlayed with the experimental profile, in black. Each vertical black bar indicates the standard deviation over each row (for all transducer elements) in the image. Panel F expresses the normalized root-mean-squared error (NRMSE) as a function of the ensemble length. V_z indicates that all axial velocities in the triangulation region were used in the assessment. V_z* indicates that only the axial velocity components in the vicinity of the flow, from a depth of 1.36 cm to 2.16 cm were used.

The error in the flow-centric region varied from 15% to 25.3%, again with minimum error for the reconstruction consisting of a 25 image ensemble.

Figure 5.7 shows that the axial velocity profile differs only slightly with increasing ensemble length. All profile plots show relatively larger standard deviation in the region where the flow exists, as well as in the erroneous region between 2 and 3 cm. The normalized root-mean-squared-error remains relatively constant at roughly 7.5% and 14% for the full imaging and the partial flow-bounded region, respectively.

Confirmed in figure 5.8A, the variation in the estimates, measured by the mean standard deviation is greater in the active flow region compared with the full image. However, neither case, for both lateral and axial components, varies significantly with respect to ensemble length. The mean axial standard deviation ranged from 0.45 to 0.5 $cm \cdot s^{-1}$ over the full image and 1.0 to 1.45 $cm \cdot s^{-1}$ in the localized flow region. The mean lateral standard deviation was higher and ranged from 1.8 to 2.1 $cm \cdot s^{-1}$ over the full image and 3.8 to 4.1 $cm \cdot s^{-1}$ in the flow region.

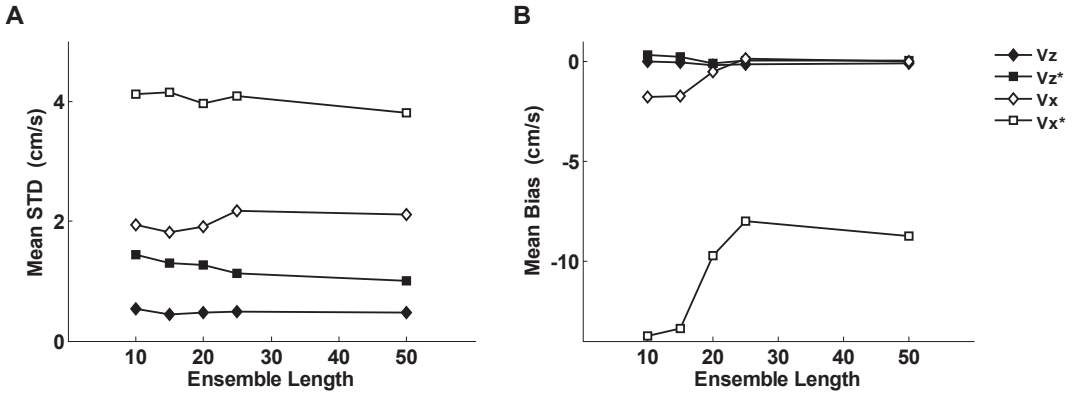

Figure 5.8: Panels A and B demonstrate the mean standard deviation (STD) and mean bias in the velocity estimates of the axial and lateral velocities, for a given ensemble length. V_z and V_x indicate that all velocities in the triangulation zone were used. V_z* and V_x* indicate only velocities in the vicinity of the flow were used, from 1.36 cm to 2.16 cm, in depth.

The mean bias in the axial estimate remained close to zero due to the consistent fluctuation about zero, in both the full triangulated region and the localized flow region. On the other hand, the mean lateral bias displayed a tendency to decrease

(in magnitude) as the ensemble length increased to a minimum at an ensemble length of 25 images.

The bias on the lateral estimate for the full image was very low (from roughly -1.7 to 0 cm·s^{-1}) which could be attributed to the large overestimation accumulated in the erroneous area, between 2 to 3 cm in depth, thwarting the underestimation in the flow region. By looking to the mean bias plot in the flow-bounded region, it is clear that the mean bias in the estimate is larger, ranging from approximately -13.7 to -8.0 cm·s^{-1} (roughly 23% to 13.6% of the maximum lateral velocity). In both imaging areas, the minimum magnitude of mean bias was attained for an ensemble length of 25.

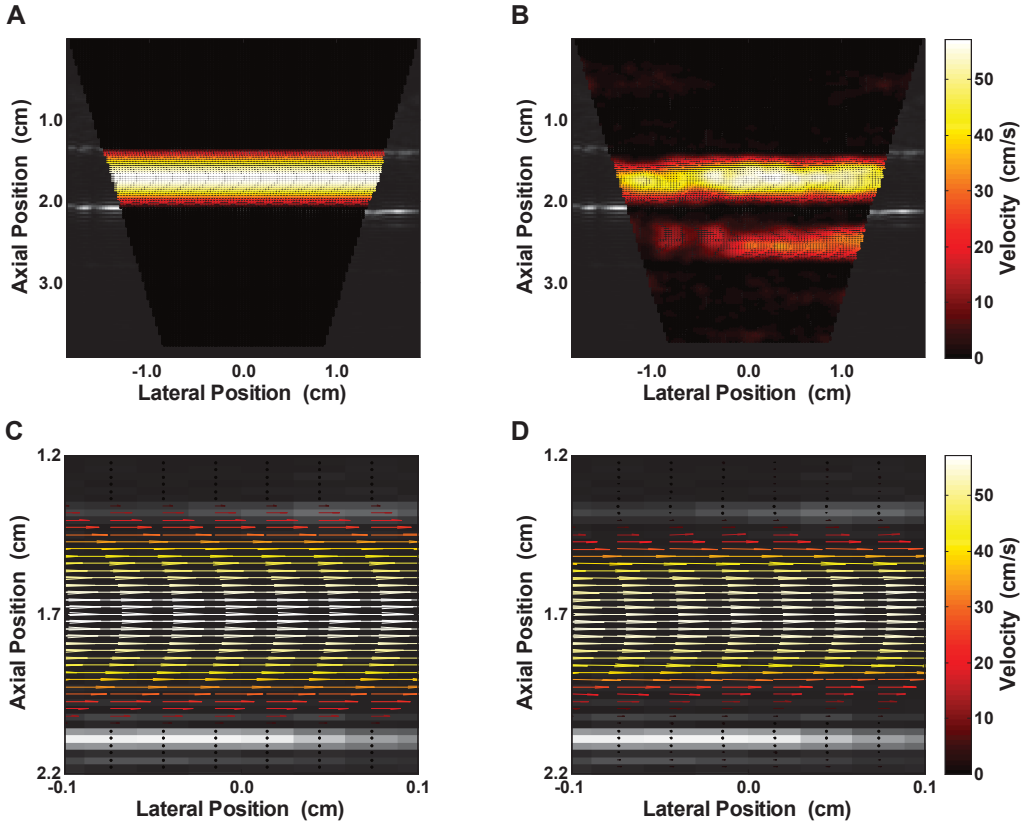

Figure 5.9: Vector flow mapping showing the magnitude and direction of the flow. Panel A shows the full theoretical velocity profile. Panel B shows the experimentally determined flow profile obtained using the parameters in table 5.2 with an ensemble length of 25. Panel C and D are zoomed depictions of panels A and B, repectively.

In view of the results for the normalized root-mean-squared error, mean standard deviation and mean bias, an optimal estimate emerges from an ensemble length of

25. Figure 5.5 displays the vector flow map of an acquisition with an ensemble length of 25. Qualitatively, the experimental profiles, within the confines of the pipe flow, in panels B and D are accurate reconstructions of the theoretical profiles in panel A and C. However, artefacts, which lie deeper than the vessel, are misleading. Akin to the previous vector map in figure 5.5, the zoomed vector map demonstrates the susceptibility of the estimation method to underestimation bias.

5.3 Variation in the Number of Pulse Cycles Per Transmit

Once again, the acquisition protocol depicted in figure 4.4B (with tilted compounding) was used. So far, since the optimal reconstruction was found to exist for 7 tilts per image, this configuration was employed here. The number of cycles per transmit used to acquire each oriented image was varied from 2 to 8, in increments of 2. The acquisition parameters are summarized in table 5.3.

Table 5.3: Acquisition parameters used to compare the results of velocity vector mapping subject to a variable number of pulse cycles per transmit.

Parameter	Value
Flow-rate (L/min)	0.8
f_0 (MHz)	5
f_s (MHz)	20
c (m/sec)	1540
Cycles at f_0	2, 4, 6, 8
Angle (°)	±15
Numer of elements	128
N (number of tilts)	7
Ensemble Length	12
Number of firings	84
Effective PRF (Hz)	1700 Hz
Frame-rate (fps)	850

The outcome of all four lateral velocity profile estimates in figure 5.10A-D present satisfactory agreement with the theoretically derived contour. Concurrent with previous results, low velocity errors which manifest slightly deeper than the flow region, between 2 and 3 cm, still exist. With regards to the normalized root-mean squared error on the lateral velocities (figure 5.10E), a range of 4.6 to 5.8% error was measured over the entire image with a minimum point at 6 cycles per pulsed transmit. In the flow-bounded region, errors from 8.8 to 12.4% were found, also with a minimum at 6 cycles per pulse.

Figure 5.11A-D, delineates the experimental versus theoretical profile of the axial velocity components. All four cases show higher variability within the flow region and the erroneous periphery, at a depth of 2 to 3 cm.

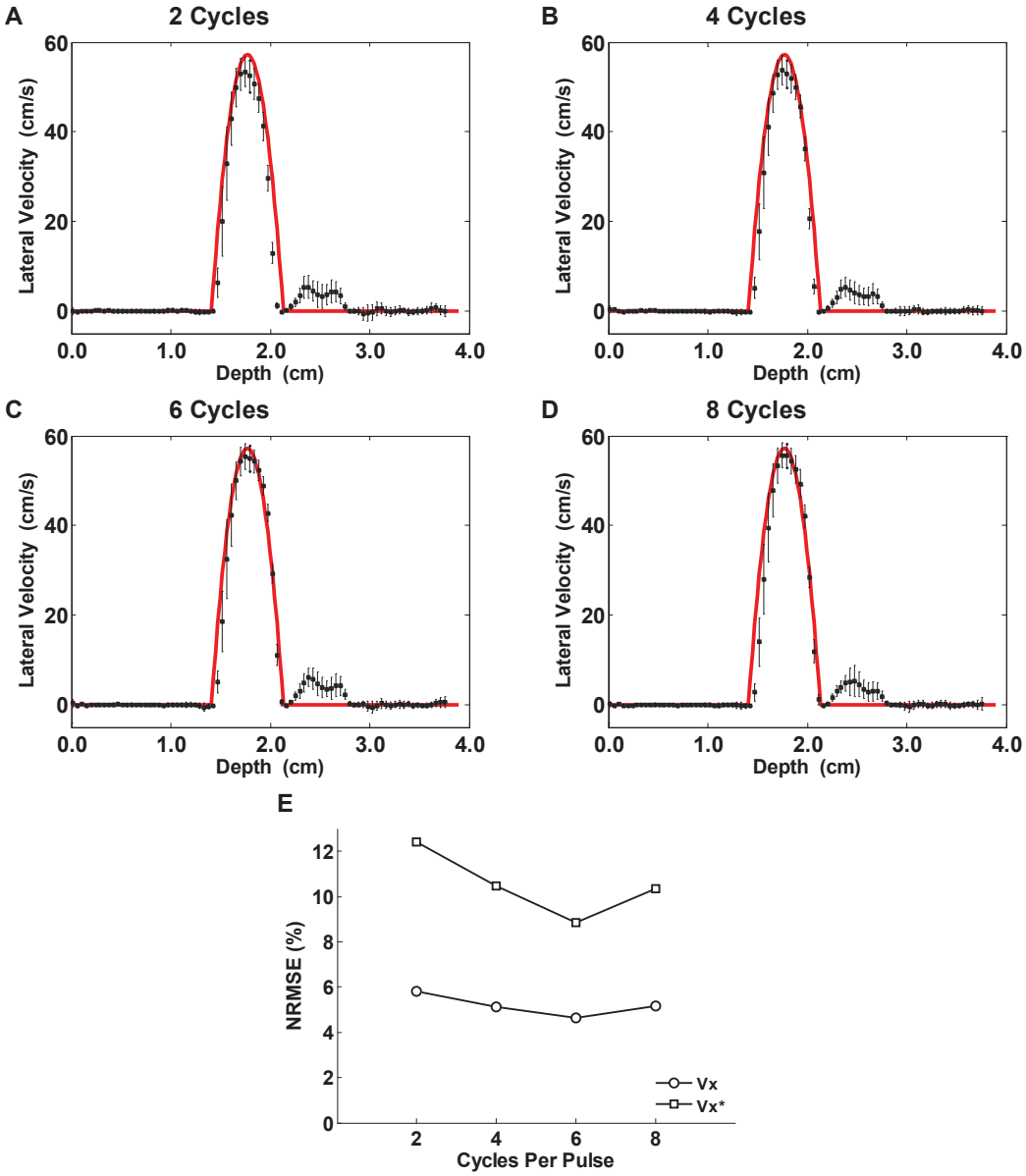

Figure 5.10: Panels A to D show the average lateral velocity profile as a function of depth. Each panel differs in the number of cycles per transmit pulse used to obtain each oriented image. The red curve provides the theoretical profile overlayed with the experimental profile, in black. Each vertical black bar indicates the standard deviation over each row (for all transducer elements) in the image. Panel E expresses the normalized root-mean-squared error (NRMSE) as a function of the pulse length. V_x indicates that all lateral velocities in the triangulation region were used in the assessment. V_x* indicates that only the lateral velocity components in the vicinity of the flow, from a depth of 1.36 cm to 2.16 cm, were used.

Among the four cases there is no significant difference in normalized root-mean-squared error. Over the full image the error remained at approximately 6.0%, and roughly 12.0% in the local flow vicinity.

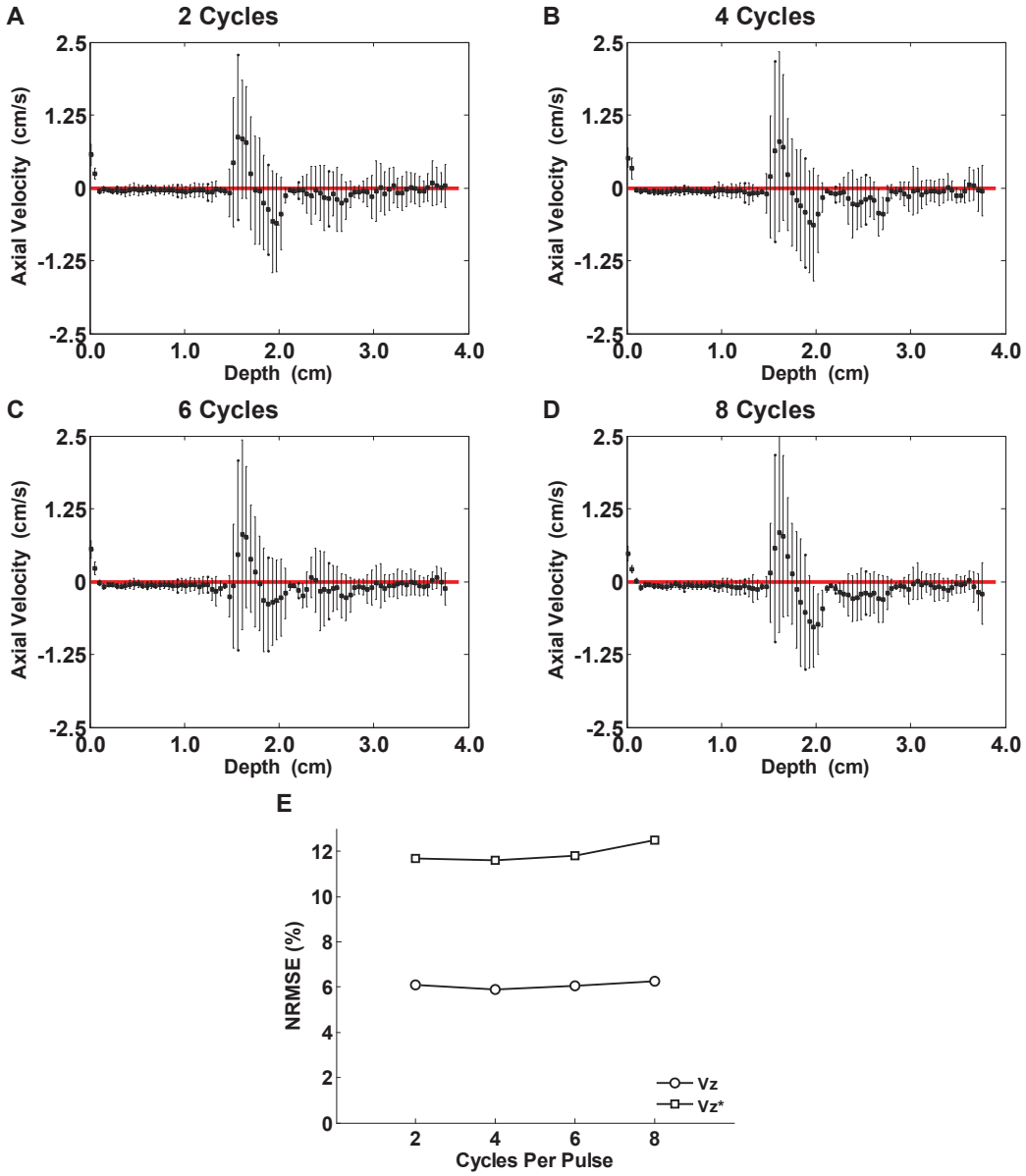

Figure 5.11: Panels A to D show the average axial velocity profile as a function of depth. Each panel differs in the number of cycles per transmit pulse used to obtain each oriented image. The red curve provides the theoretical profile overlayed with the experimental profile, in black. Each vertical black bar indicates the standard deviation over each row (for all transducer elements) in the image. Panel E expresses the normalized root-mean-squared error (NRMSE) as a function of the pulse length. V_z indicates that all axial velocities in the triangulation region were used in the assessment. V_z* indicates that only the axial velocity components in the vicinity of the flow, from a depth of 1.36 cm to 2.16 cm were used.

Panel A of figure 5.12, shows that the mean standard deviations in the localized flow, for both lateral and axial velocity components, were slightly higher than the values obtained over the full image. The mean axial standard deviation over the full triangulated zone remained constant at 0.30 $cm \cdot s^{-1}$ compared with 0.70 $cm \cdot s^{-1}$ in the flow-bounded area. Likewise, the mean lateral standard deviation over the full image stayed roughly constant at 1.30 $cm \cdot s^{-1}$ compared to 3.0 $cm \cdot s^{-1}$ in the bounded flow region.

Regarding the mean bias (figure 5.12B), the axial estimate over the entire image and in the localize flow region were roughly equal resting at about zero, in the range of -0.08 and 0.03 $cm \cdot s^{-1}$. The curves of mean lateral bias in the full triangulation zone also remained relatively constant (between -0.82 and -0.12 $cm \cdot s^{-1}$) with minimum magnitude for 6 cycles per pulse.

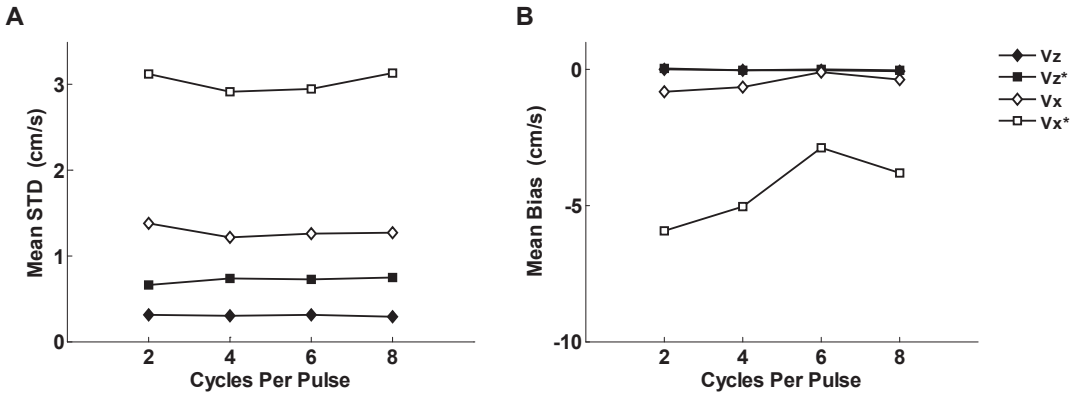

Figure 5.12: Panels A and B demonstrate the mean standard deviation (STD) and mean bias in the velocity estimates of the axial and lateral velocities, for a given pulse length in cycles per pulse. V_z and V_x indicate that all velocities in the triangulation zone were used. V_z* and V_x* indicate only velocities in the vicinity of the flow were used, from 1.36 cm to 2.16 cm, in depth.

In the delimited flow zone, the mean bias ranged from -5.15 to -2.90 $cm \cdot s^{-1}$ (8.7% and 5.0% of the maximum theoretical lateral velocity), with minimum magnitude for 6 cycles per pulse. Again, the negative sign on the mean bias implies that the reconstructions are underestimated.

By considering the axial normalized root-mean-squared error and mean bias, the optimal number of cycles per transmit pulse is decidedly 6. The vector flow map for an acquisition with 6 cycles per pulse is shown in figure 5.13. The

experimental profiles, within the confines of the pipe flow, in panels B and D are satisfactory reconstructions of the theoretical profiles in panel A and C. Certainly, as in previous examples the zoomed vector map demonstrates the susceptibility of the reconstruction method to underestimation.

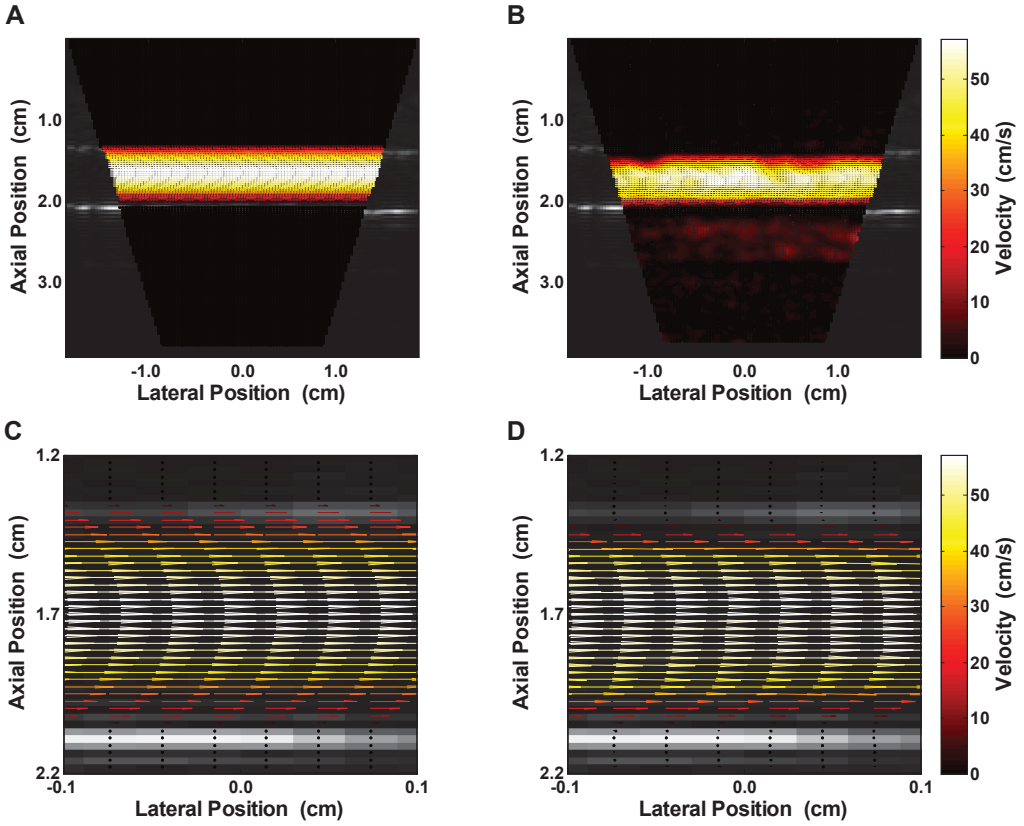

Figure 5.13: Vector flow mapping showing the magnitude and direction of the flow. Panel A shows the full theoretical velocity profile. Panel B shows the experimentally determined flow profile obtained using the parameters in table 5.3 with 6 cycles per transmit pulse. Panel C and D are zoomed depictions of panels A and B, repectively.

5.4 Variation in Angle and Flow-Rate

In this section, the acquisition protocol demonstrated in figure 4.4B (with tilted compounding) was used. The angle of acquisition (β) was varied between ±5° and ±20° in increments of 5°. Additionally, the experiments were repeated for flow at three different flow-rates: 0.55 L·min^{-1}, 0.80 L·min^{-1}, and 1.00 L·min^{-1}. For equitability in capturing the proper range of velocities, adjustments to the pulse repetition frequency were made for each angle and for different flow-rates.

5.4.1 Flow-Rate of 0.55 L·min^{-1}

Table 5.4: Acquisition parameters used to compare the results of velocity vector mapping subject to variable angles of acquisition at a flow-rate of 0.55 L·min^{-1}.

Parameter	Value
Flow-rate (L/min)	0.55
f_0 (MHz)	5
f_s (MHz)	20
c (m/sec)	1540
Cycles at f_0	2.5
Angle (°)	±5, 10, 15, 20
Numer of elements	128
N (number of tilts)	7
Ensemble Length	12
Number of firings	84
Effective PRF (Hz)	400, 750, 1200, 1500
Frame-rate (fps)	200, 375, 600, 750

The first flow-rate tested was 0.55 L·min^{-1}, thus a maximum theoretical velocity of roughly 40.4 cm·s^{-1}. The acquisition parameters are summarized in table 5.4.

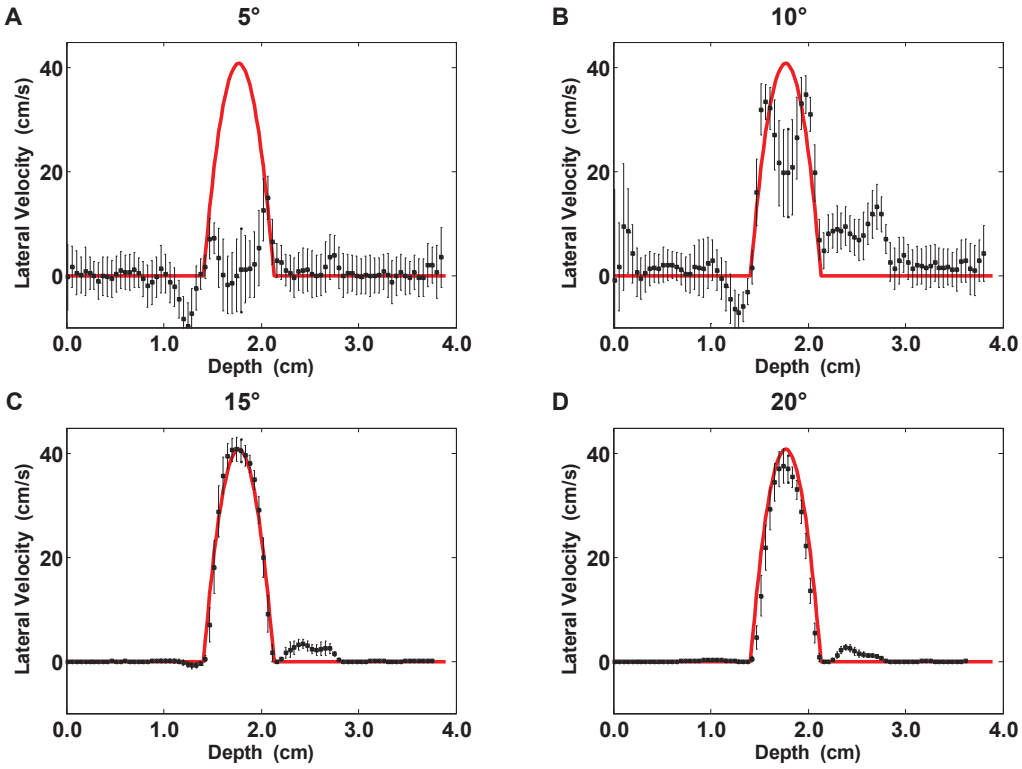

Figure 5.14: Panels A to D show the average lateral velocity profile as a function of depth. Each panel differs in the acquisition angle used to attain each image. The red curve provides the theoretical profile overlayed with the experimental profile, in black. Each vertical black bar indicates the standard deviation over each row (for all transducer elements) in the image.

Through inspection of figure 5.14 it is evident that small angles are not effective when estimating the lateral velocity with the present reconstruction method. At ±5°, the reconstructed flow is incoherent and large variations exist at all depths. At ±10°, the flow begins to present itself within the flow region; however, the experimental profile is not a faithful representation of the theoretical flow.

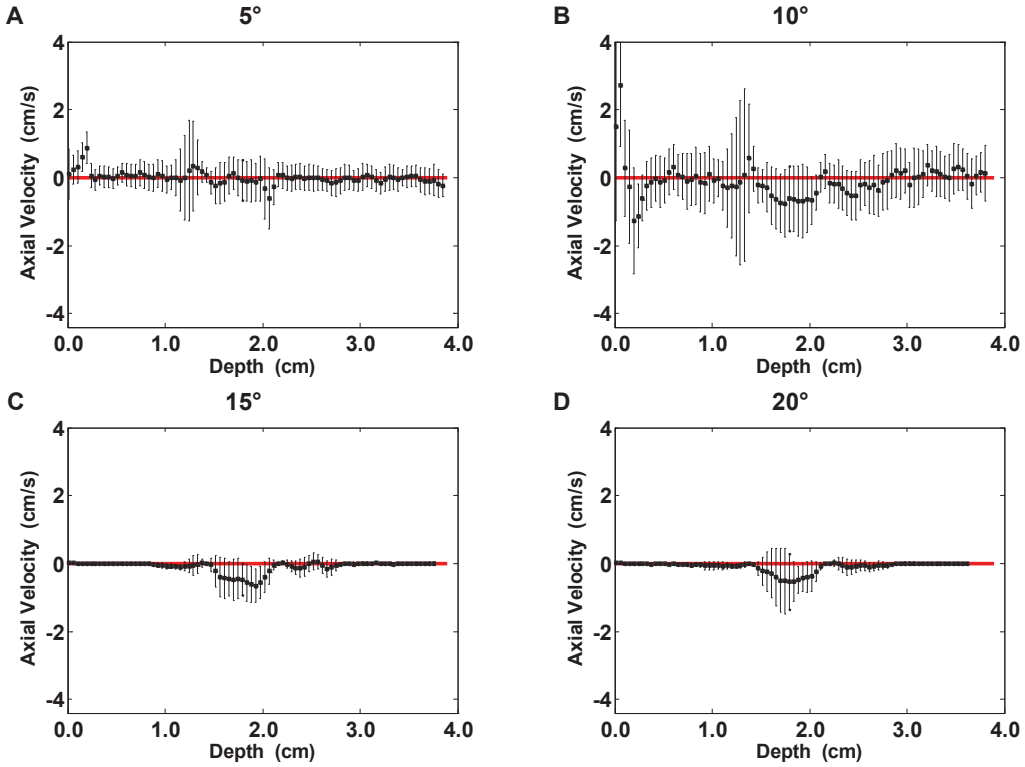

Figure 5.15: Panels A through D show the average axial velocity profile as a function of depth. Each panel differs in the acquisition angle used to attain each oriented image. The red curve provides the theoretical profile overlayed with the experimental profile, in black. Each vertical black bar indicates the standard deviation over each row (for all transducer elements) in the image.

At ±15°, the reconstruction strongly resembles the reference profile with much less variability. Furthermore, the velocity estimates from ±20° are also representative of the true profile with slight variability; however, a larger underestimation is evident. Given the axial profiles in figure 5.15, all panels are consistent, with velocity estimates close to zero. The ±5° and ±10° profiles display large variability at all depths, whereas the profiles at ±15° and ±20° only show fluctuations in the flow region.

5.4.2 Flow-Rate of 0.80 L·min^{-1}

Table 5.5: Acquisition parameters used to compare the results of velocity vector mapping subject to variable angles of acquisition at a flow-rate of 0.80 L·min^{-1}.

Parameter	Value
Flow-rate (L/min)	0.80
f_0 (MHz)	5
f_s (MHz)	20
c (m/sec)	1540
Cycles at f_0	2.5
Angle (°)	±5, 10, 15, 20
Numer of elements	128
N (number of tilts)	7
Ensemble Length	12
Number of firings	84
Effective PRF (Hz)	570, 1200, 1700, 2300
Frame-rate (fps)	285, 600, 850, 1150

The second flow-rate tested was 0.80 L·min^{-1}, thus a maximum theoretical velocity of roughly 58.8 cm·s^{-1}. The acquisition parameters are shown in table 5.5.

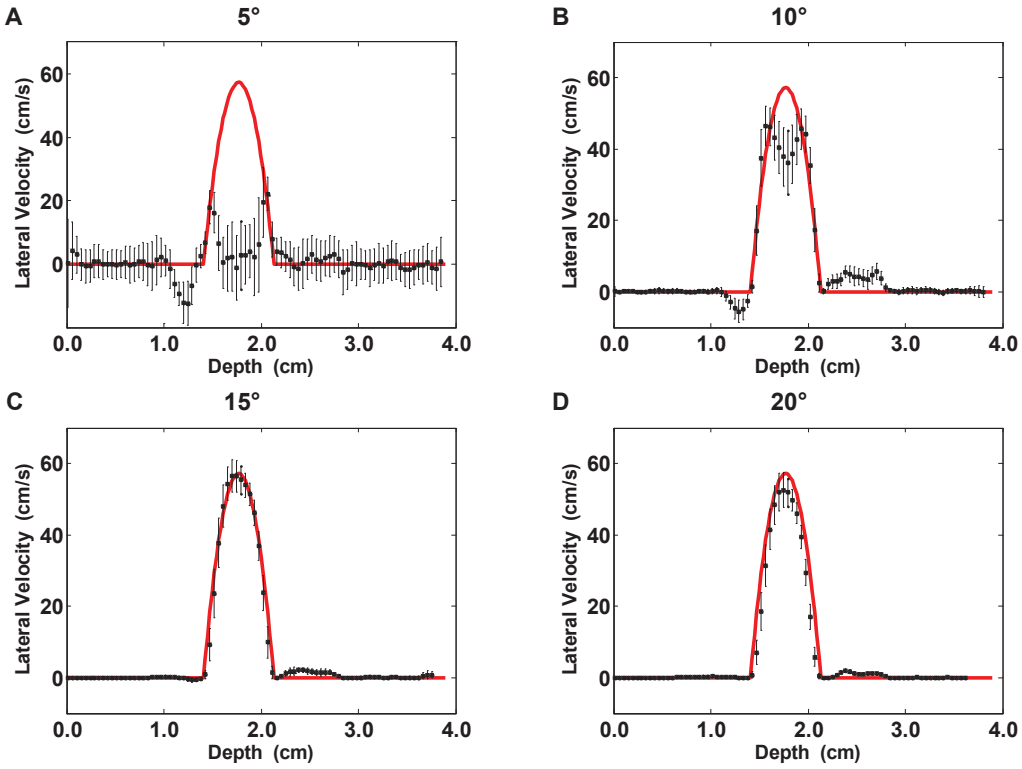

Figure 5.16: Panels A through D show the average lateral velocity profile as a function of depth. Each panel differs in the acquisition angle used to attain each oriented image. The red curve provides the theoretical profile overlayed with the experimental profile, in black. Each vertical black bar indicates the standard deviation over each row (for all transducer elements) in the image.

The outcome of the reconstruction with variable angle for a slightly increased flow-rate is in accordance with the results of the previous sub-section (5.4.1). In figure 5.16, at ±5°, the reconstruction of the lateral component is ineffective. At ±10°, a discernible pattern starts to arise. Nonetheless, it is not until ±15°, that the estimates firmly resemble the theoretical profile. Again, at ±20° the lateral velocities are underestimated.

Additionally, figure 5.17 shows that at ±5° and ±10°, the reconstruction of the axial component has a large amount of variability at all depths, whereas at ±15° and ±20° the variability exists predominantly in the flow region.

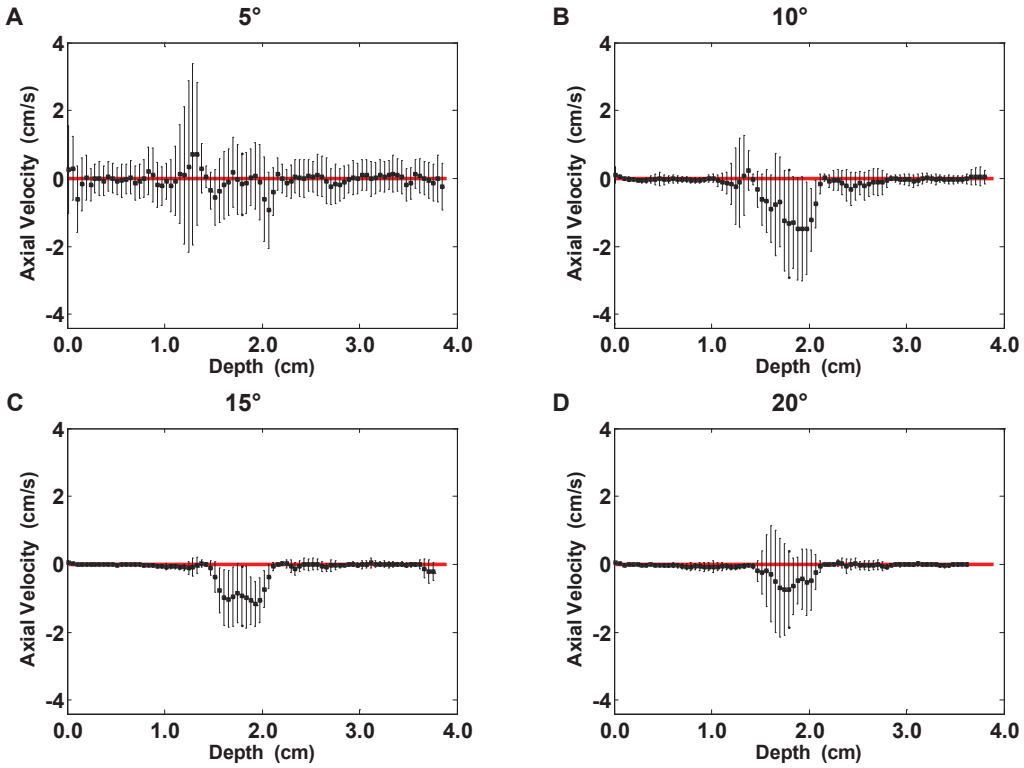

Figure 5.17: Panels A through D show the average axial velocity profile as a function of depth. Each panel differs in the acquisition angle used to attain each oriented image. The red curve provides the theoretical profile overlayed with the experimental profile, in black. Each vertical black bar indicates the standard deviation over each row (for all transducer elements) in the image.

5.4.3 Flow-Rate of 1.00 L·min^{-1}

Table 5.6: Acquisition parameters used to compare the results of velocity vector mapping subject to variable angles of acquisition at a flow-rate of 1.00 L·min^{-1}.

Parameter	Value
Flow-rate (L/min)	1.00
f_0 (MHz)	5
f_s (MHz)	20
c (m/sec)	1540
Cycles at f_0	2.5
Angle (°)	±5, 10, 15, 20
Numer of elements	128
N (number of tilts)	7
Ensemble Length	12
Number of firings	84
Effective PRF (Hz)	750, 1500, 2250, 3000
Frame-rate (fps)	375, 750, 1125, 1500

The final flow-rate tested was 1.00 L·min^{-1}, hence a maximum theoretical velocity of roughly 73.5 cm·s^{-1}. The acquisition parameters are summarized in table 5.6.

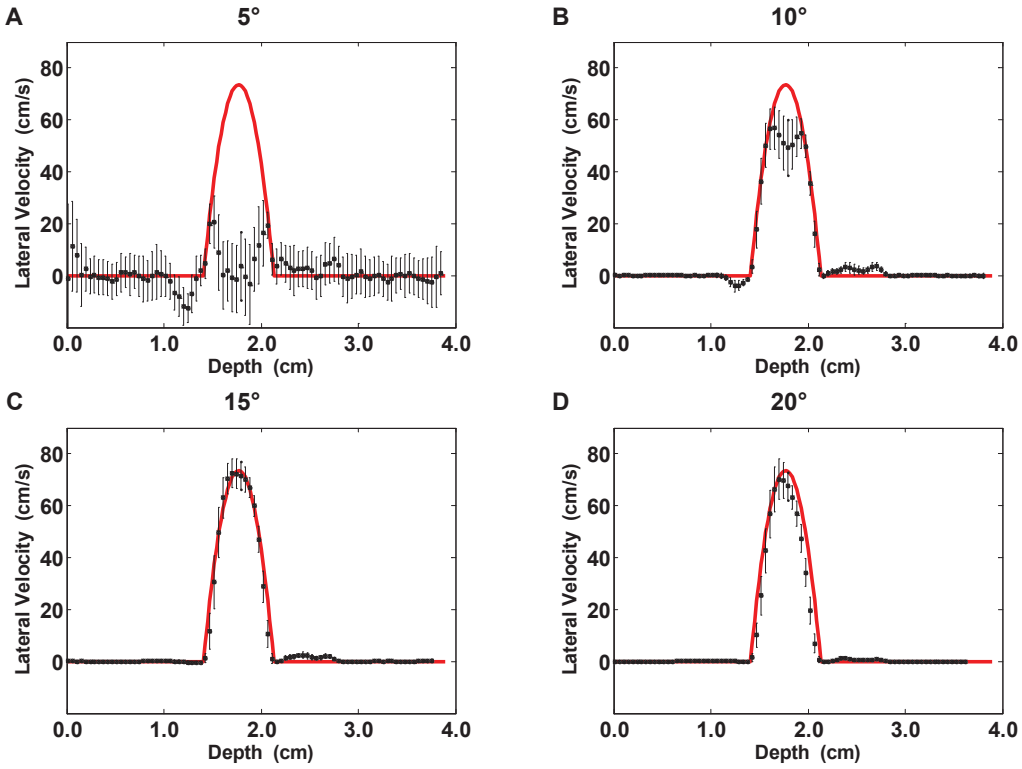

Figure 5.18: Panels A through D show the average lateral velocity profile as a function of depth. Each panel differs in the acquisition angle used to attain each oriented image. The red curve provides the theoretical profile overlayed with the experimental profile, in black. Each vertical black bar indicates the standard deviation over each row (for all transducer elements) in the image.

The reconstruction at a 1.00 L·min^{-1} flow-rate is also congruent with the results of the previous two sub-section (5.4.1 and 5.4.2), at lower flow-rates. Figure 5.18, confirms that at ±5°, the reconstruction of the lateral component is inadequate.

At ±10°, the experimental results begin to resemble the reference flow, and seem to improve slightly with increasing flow. Again, it is not until ±15°, that the estimate becomes convergent with the theoretical profile. Then at ±20° the lateral velocities are fitting but underestimated.

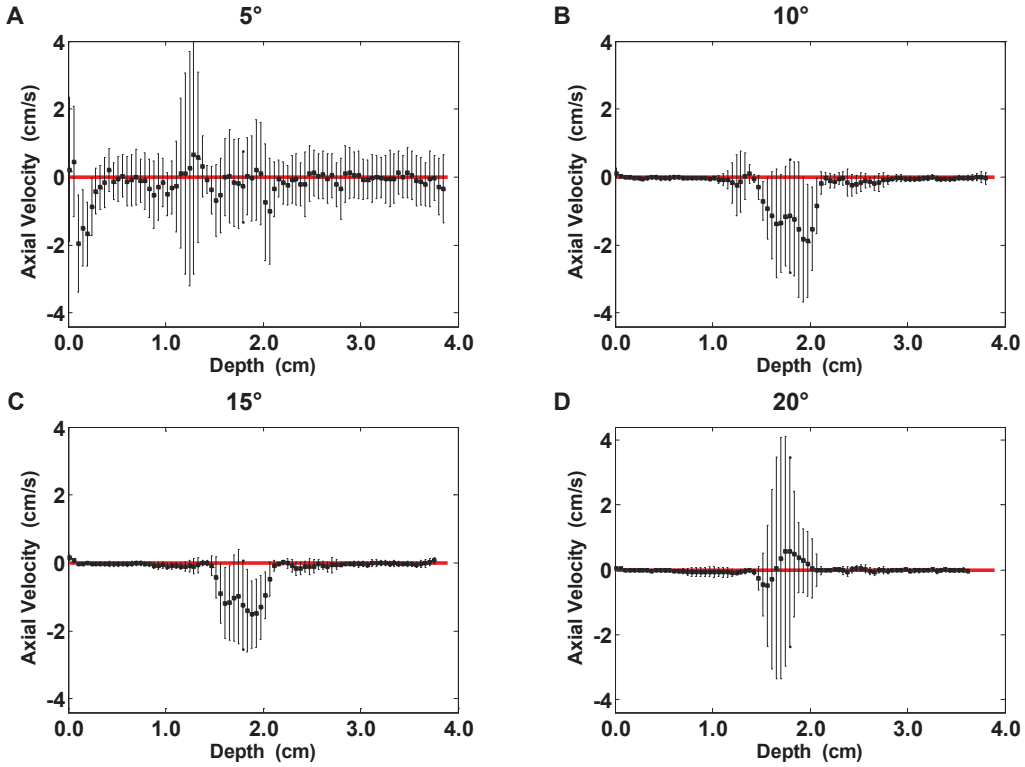

Figure 5.19: Panels A through D show the average axial velocity profile as a function of depth. Each panel differs in the acquisition angle used to attain each oriented image. The red curve provides the theoretical profile overlayed with the experimental profile, in black. Each vertical black bar indicates the standard deviation over each row (for all transducer elements) in the image.

Concerning the axial velocity estimates (figure 5.19), apart from the consistent wide spread variability shown at ±5°, the axial estimates ±10° seem to grow more localized in flow region as the flow-rate increases. For all angles the magnitude of the standard deviation increases slightly with increased flow.

5.4.4 Quantitative Comparison

In this sub-section, the effect of angle on the reconstruction, at the three aforementioned flow-rates (0.55, 0.80 and 1.00 $L \cdot min^{-1}$), are evaluated quantitatively. The normalized root-mean-squared error, mean standard deviation and mean bias are again used as a basis of assessment.

Figure 5.20, allows the visualization of the normalized root-mean-squared error in the lateral and axial velocity components for varying angles of reception. First, to reiterate from prior observations of sections 5.1, 5.2, and 5.3, the errors over the full image are notably lower than the errors in the local flow region, designated by *. This may be attributed to the large approximately zero background in the full triangulation zone which lowers the mean root-mean-squared residual before normalization compared with the higher residuals from underestimation in the local flow region.

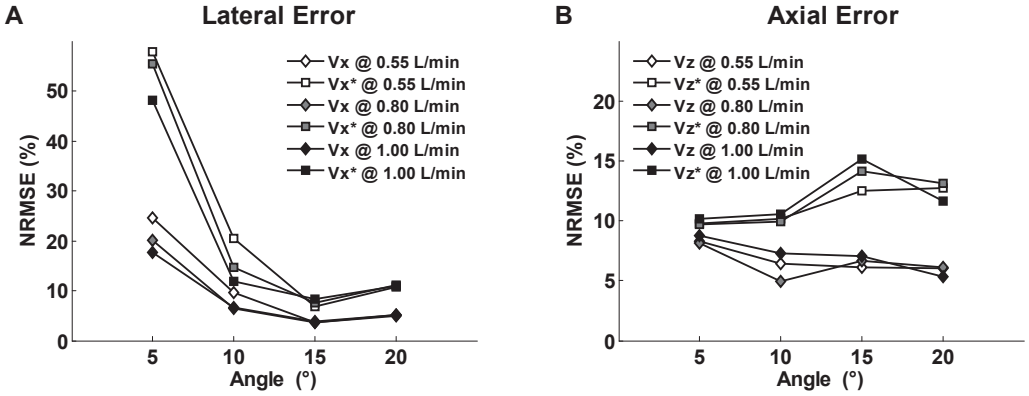

Figure 5.20: Panels A and B express the normalized root-mean-squared error (NRMSE) on the lateral and axial velocity components as a function of angle at different flow-rates. V_x and V_z indicate that all lateral and axial velocities in the triangulation region were used in the assessment. The * indicates that only the components in the vicinity of the flow, from a depth of 1.36 cm to 2.16 cm were used.

Panel A of figure 5.20 shows the error in the lateral estimates. The first pronounced observation is the appreciable decrement in error with increasing angle until 15°. For instance, by increasing from 5° to 10°, the normalized root-mean-squared error (over the flow-localized region at 0.55 $L \cdot min^{-1}$) decreases from roughly 58% to 20% error, reaching a minimum of 7.5% error at 15° before

ascending slightly to 11% at 20°. For all flow conditions we see the same declivitous trend.

Respecting the different flow conditions, a remark can be made to point out that at low angles, low flow conditions appear to be less favourable. For example, at 10° the error in the local flow vicinity at 0.55, 0.80 and 1.00 $L \cdot min^{-1}$ was roughly 20%, 15% and 12%, respectively. At larger angles, the errors in the velocity estimates seem to converge over all the flow conditions tested.

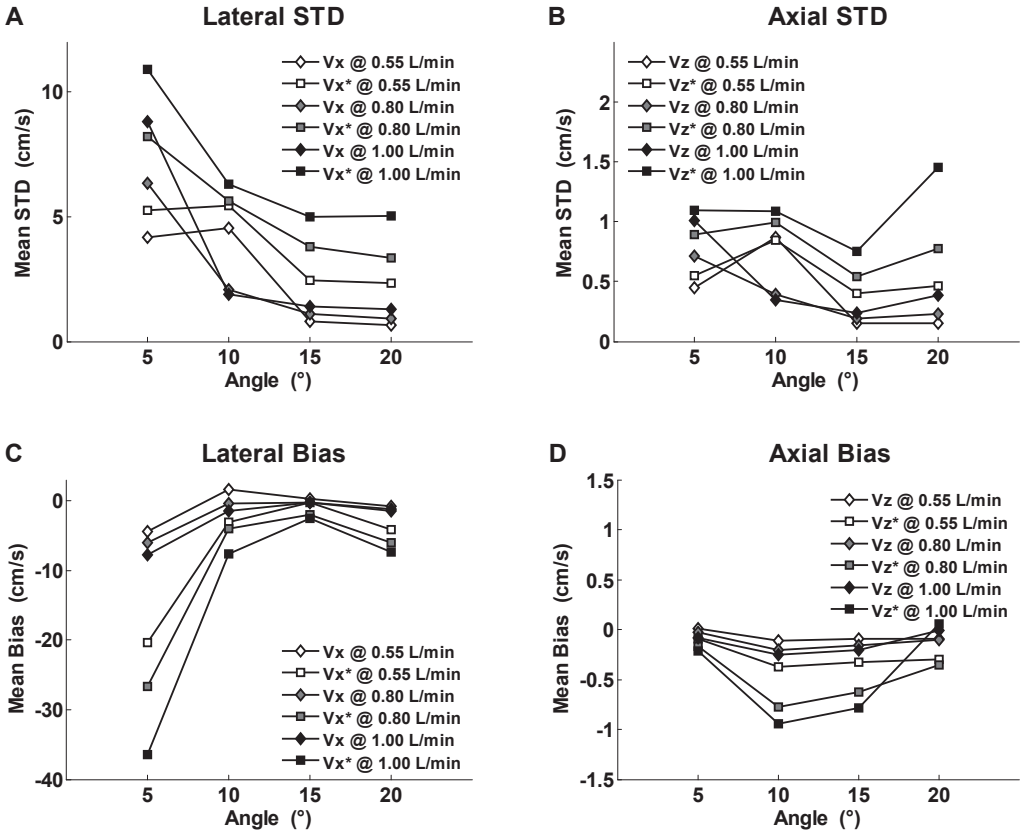

Figure 5.21: Panels A and B demonstrate the mean standard deviation (STD) in the estimates of the lateral and axial velocities, V_x and V_z, for a given angle at different flow-rates. Panels C and D depict the mean bias in the estimates of the lateral and axial velocities, V_x and V_z, for a given angle at different flow-rates. V_x and V_z indicate that all lateral and axial velocities in the triangulation region were used in the assessment. The * indicates that only the components in the vicinity of the flow, from a depth of 1.36 cm to 2.16 cm were used.

Panel B of figure 5.20 shows the error in the axial estimates, which are more elusive. No distinct trend is evident. Over the full zone of triangulation the percent error decreases with increasing angle, ranging between roughly 8.5 and 5.0%. In

the direct environs of the flow the error increases with increasing angle, indicating the highest errors of 15%, 14% and 12.5% (for 0.55, 0.80 and 1.00 $L \cdot min^{-1}$) at 15°.

Figure 5.21 shows the mean standard deviation (in $cm \cdot s^{-1}$) in the lateral (panel A) and axial (panel B) velocity estimates for a given angle and flow-rate. The global trend shows that the standard deviation decreases as angle increases and as flow-rate decreases, i.e. larger variations in the data for small angles and faster flows, with the exception of the two measures found for an angle of 10° at 0.55 $L \cdot min^{-1}$ which seem unfitting. Again, the full triangulation zone has lower mean standard deviation compared with the bounded flow region.

In another view, the mean lateral standard deviation is re-plotted as a percentage of the maximum lateral velocity, for each angle at each flow-rate (see figure 5.22A). As such, the effect of angle becomes more apparent, in that the mean standard deviations are normalized and agree well for the three flow-rates tested, again, with the exception of the two measures found for and angle of 10° at 0.55 $L \cdot min^{-1}$. The minimum mean percent standard deviation (normalized by the maximum lateral velocity) was roughly 2% and 6.5% in the full triangulation zone and local flow vicinity, respectively, and was found around 15° to 20°.

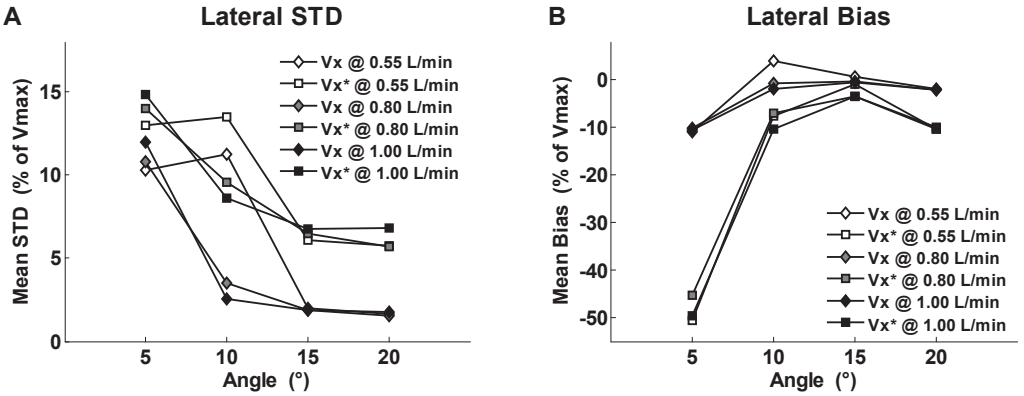

Figure 5.22: Panels A and B demonstrate the mean standard deviation (STD) and mean bias in the estimates of the lateral velocities, V_x and V_x*, as a percentage of the maximum lateral velocity, for a given angle at different flow-rates. The * indicates that only the components in the vicinity of the flow, from a depth of 1.36 cm to 2.16 cm were used.

Regarding the mean bias in the lateral velocity estimates for variable angle and flow-rate (panel C of figure 5.21), it is obvious that the reconstructed components

are underestimated, which is indicated by the negative sign. Furthermore, as the angle of reception increases, the magnitude of the mean bias decreases toward zero, reaching a minimum at 15°. Anew, the measured mean bias in the localized flow region is worse than the full triangulated region. As well, the underestimation worsens with increasing flow-rate.

By plotting the mean lateral bias as a percentage of the maximum lateral velocity (see figure 5.22 panel B), the effect of angle once again becomes more evident. The minimum mean percent bias of roughly -0.3% and 4.0% of the maximum lateral velocity in the full triangulation zone and local flow vicinity, respectively, and was found at 15°.

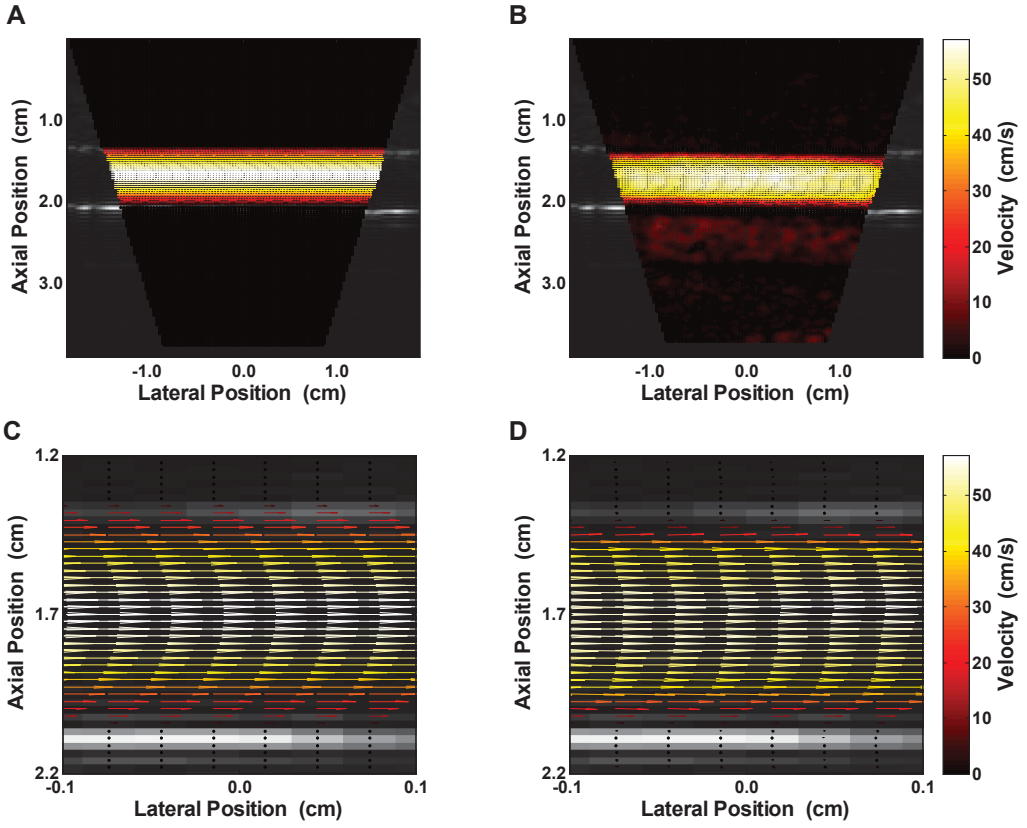

Figure 5.23: Vector flow mapping showing the magnitude and direction of the flow. Panel A shows the full theoretical velocity profile. Panel B shows the experimentally determined flow profile obtained using the parameters in table 5.5 at an angle of 15°. Panel C and D are zoomed depictions of panels A and B, repectively.

Finally, the mean bias values in the axial velocity estimates, for variable angle and flow-rate (panel D of figure 5.21), show no marked tendency. The mean bias at higher flow-rates was slightly higher in magnitude than at low flow-rates. Also the bounded flow region was subject to more bias than the full triangulation zone.

By considering the normalized root-mean-squared error, mean bias and mean standard deviation, the optimal angle of reception was 15°. The vector flow map for an acquisition defined by table 5.5 with a 15° angle of reception (β) is shown in Figure 5.23. The experimental profiles, within the confines of the pipe flow, in panels B and D are satisfactory reconstructions of the theoretical profiles in panels A and C. However, the susceptibility of the estimation method to a slight underestimation is evident when comparing the zoomed vector maps.

Chapter 6 : Discussion

The previous experimental examples demonstrate the effectiveness of plane-wave imaging, post-processed with the delay-and-sum method, autocorrelation method and triangulation, to provide two-dimensional vector flow mapping, *in vitro*. It can be conceded that plane-wave imaging, when compared with conventional focused imaging, suffers from decreased penetration depth, higher side lobe levels and poorer resolution [19]. Therefore, the autocorrelation velocity estimation method and triangulation were selected here because they have been proven robust at increasing depths and to perform well under worse signal-to-noise-ratios [39]. Additionally, this approach has been shown to be less computationally complex than other methods.

With simple Poiseuille flow experimentation using the theoretical profile as a reference, the effects of different acquisition parameters on the estimation accuracy were tested. This allowed us to focus our attention to the optimal conditions under which the reconstruction would ideally be implemented, the normalized root-mean-squared error, mean standard deviation and mean bias for each of the selected cases are summarized in table 6.1, table 6.2 and table 6.3, respectively.

Table 6.1: Normalized root-mean-squared error (NRMSE) on the lateral and axial components of velocity for each optimal case found through comparison in sections 5.1 to 5.4. The * indicates that the calculation was done on a flow bound region rather than the full triangulation zone.

			NRMSE (%)			
Parameter	**Optimal Case**		**Vx**	**Vx***	**Vz**	**Vz***
Number of tilts (*N*)	N = 7 tilts		5.94	10.09	7.83	13.56
Ensemble Length (*K*)	K = 25 ensemble length		9.64	15.06	7.33	14.33
Cycles per pulse	6 cycles per pulse		4.64	8.85	6.05	11.79
		0.55 L/min	3.62	6.91	6.14	12.49
Angle (°)	±15	0.80 L/min	3.58	7.61	6.65	14.13
		1.00 L/min	3.82	8.25	7.07	15.16

This study acknowledges that not one but several scanning and reconstruction permutations will yield reliable and accurate results. Again, the aim here was to

investigate the influence of important parameters involved for a better understanding of the influence each parameter has on the mapping accuracy.

Two lines of plane-wave Doppler imaging have been disclosed. In a study by Bercoff *et al*. [18], the compounded scanning convention shown in figure 4.4B was used. They obtained single orientation ($\beta = 0°$) ensembles, that is to say with no 2D vector mapping, with a variable number of tilted acquisitions (N), which they then compared qualitatively with conventional focused Doppler imaging to substantiate their method. In another study by Ekroll *et al*. [19], the scheme given in figure 4.4A was used. They obtained dual oriented ensembles with no compounding. Each firing corresponded to one image in the Doppler ensemble (K) for which they varied the length of the Doppler ensemble. These two studies provided the grounds for the first two investigations.

The results of section 5.1 demonstrate that by increasing the number of tilts per oriented image (holding all other parameters constant), the velocity estimates improve. It was found that 7 tilts per orientation is the optimal case. This scenario provided an effective pulse repetition frequency of 1700 images per second, providing a continual frame-rate of roughly 850 frames per second (for dual angle triangulation), with an interval between packets (K_L) equal to one (refer back to equation 3.3 and figure 3.3 for clarification). With this marked increase in frame-rate, the normalized root-mean-squared error, mean standard deviation and mean bias were on par with published literature obtained using conventional focused velocity vector mapping [39].

Table 6.2: Mean standard deviation (STD) on the lateral and axial components of velocity for each optimal case found through comparison in sections 5.1 to 5.4. The * indicates that the calculation was done on a flow bound region rather than the full triangulation zone.

			Mean STD (cm/s)			
Parameter	**Optimal Case**		**Vx**	**Vx***	**Vz**	**Vz***
Number of tilts (N)	N = 7 tilts		1.52	2.81	0.30	0.59
Ensemble Length (K)	K = 25 ensemble length		2.17	4.10	0.49	1.13
Cycles per pulse	6 cycles per pulse		1.26	2.95	0.31	0.73
		0.55 L/min	0.80	2.45	0.15	0.40
Angle (°)	±15	0.80 L/min	1.11	3.80	0.19	0.54
		1.00 L/min	1.40	4.98	0.24	0.75

The second experimental inquiry (results of section 5.2) was to determine which ensemble length yields the best velocity estimate based on the single zero-tilted compounded method proposed by Ekroll *et al*. [19]. They state that a single plane-wave provides ample resolution and contrast to provide Doppler velocity measurements and by increasing the ensemble length the estimates may be improved. The present results are in agreement. There is a considerable decrease in normalized root-mean-squared error and magnitude of mean bias by increasing the ensemble length, especially in the lateral estimates. This configuration also provides sufficient accuracy when compared to conventional vector-Doppler results [39]; however, the tilted compound imaging protocol [18, 67] previously discussed seems to provide a slightly more robust estimate when imaged with the same frame-rate.

Contrarily, one major advantage of the single tilted convention is the potential maximum flexibility in the velocity range, due to the ability to attain the highest effective pulse repetition frequency since it involves no compounding of multiple tilted images. By acquiring larger ensembles with the highest possible frame-rates, higher velocity components are achievable [19]. The pulse repetition frequency may be elevated to a higher extent, within reasonable limits (defined in section 2.3.1.a); however, this does not come at a compromise to the lower velocity limit due to the ability to proportionally increasing the ensemble length (see section 2.3.2.b) and/or perform the autocorrelation with a longer lag between frames. Rather than computing the estimation on consecutively received signals, intervals may be used to insure a better estimate [19] while maintaining the same ultrafast frame-rate.

From the aforementioned results, we see that the acquisition time for velocity vector mapping can be greatly improved by more than 10 to 20 times depending on the configuration, i.e. the number of compounded tilts used per image or the length of the Doppler ensemble. These velocity vector mapping methods provide the possibility of imaging faster flows than conventional methods due to the

improved temporal resolution of plane-wave imaging, opening the door to better quantification of transient or turbulent flows.

Here, the acquisition rate was approximately 850 vector maps per second. All post-processing was done offline. One particular constraint to this frame-rate is the ability to manipulate and post-process such large plane-wave datasets efficiently for a real-time application. Emergent technology, easily implemented on ultrasound systems, can enable rapid transfer of large datasets as well as high speed computation with parallel processing.

Table 6.3: Mean bias on the lateral and axial components of velocity for each optimal case found through comparison in sections 5.1 to 5.4. The * indicates that the calculation was done on a flow bound region rather than the full triangulation zone.

			Mean Bias (cm/s)			
Parameter	**Optimal Case**		**Vx**	**Vx***	**Vz**	**Vz***
Number of tilts (*N*)	N = 7 tilts		-0.09	-4.29	-0.07	0.01
Ensemble Length (*K*)	K = 25 ensemble length		0.12	-7.98	-0.15	0.05
Cycles per pulse	6 cycles per pulse		-0.12	-2.90	-0.05	0.01
		0.55 L/min	0.24	-0.34	-0.09	-0.33
Angle (°)	±15	0.80 L/min	-0.23	-2.06	-0.16	-0.63
		1.00 L/min	-0.33	-2.59	-0.21	-0.79

Next in succession, is the importance of the emitted pulse length (mentioned in section 1.2.3.b) to the phase-shift autocorrelation estimation method, used in this study. The autocorrelation method is a narrowband estimator; therefore, it works optimally for comparably longer pulse lengths than B-mode imaging or cross-correlation based velocity estimators. Consequently this also means that Doppler imaging has relatively lower axial resolution compared with other broadband estimators such as the time-shift cross-correlation technique (see section 2.3.3). Conventional Doppler imaging makes use of a pulse with 5 to 20 cycles (typically 8) at the central frequency [22, 69].

Contrary to preference given to longer pulses when employing the autocorrelation technique, studies have used 2.5 [19] and 3 [18] cycles per transmit pulse for velocity estimation without warrant. In the above results, it has been shown that varying the number of cycles per transmit pulse, between two and eight, does not show a striking impact on the reconstruction accuracy of the present plane-wave

method. However, apparent from the normalized root-mean-squared error and mean bias curves (particularly figure 5.10E and figure 5.12B), 6 cycles per pulse transmission was the optimal beam setting for the protocol defined back in table 5.3 of section 5.3.

The influence of angle had the most profound effect on velocity vector map accuracy. Increasing the angle to ±15° shows a drastic declivity in normalized root-mean-squared error and in the magnitude of the underestimation bias, specifically on the lateral velocity component. This is exactly as expected. Since the flow lies parallel to the scanning surface, more acute angles means the beam-to-flow angle is roughly at 90°. The more the angle increases away from orthogonal the better the velocity estimate.

Due to the infeasibility of physically lining up the transducer with the flow, angle steering was done through beam-forming. As mentioned in section 1.2.1.b, side lobes referred to as grating lobes, which affect the velocity estimate, worsen with increasing Doppler angle. This may provide an explanation as to why the results of the reconstruction at ±20° demonstrate a slight decrement in accuracy compared with the results at ±15°, despite improving the beam-to-flow angle. The postulation may be made that increasing the angles passed ±20° would lead to an increasing decrement in reconstruction accuracy. For future studies, varying the an vessel angle using the same acquisition protocol may be of interest to investigate larger beam to flow angles, without the effect of large angles in beam-steering.

Further involving angle, since the experimental flow used here was stationary parabolic flow, the alternating dual angle scanning sequence, used to acquire the radio-frequency data (refer to figure 4.5), conducted by firing an ensemble of K negatively angled beams before switching to acquire K positively angled beams, had no significant effect on the reconstruction. However, studying the velocity vector map reconstruction accuracy on pulsatile flow may require a slightly altered sequence to avoid temporal misalignment between the velocities at positive and negative angles. This scanning sequence would simply involve alternating between angles after each firing.

Concerning the variation in flow-rate, the normalized root-mean-squared error was higher for lower flow-rates at more acute angles; however, this is not the case for larger angles. One deduction would be that the Doppler frequencies are too low and suffer from interference by the clutter signal and clutter filter. Therefore, clutter filtering has severe repercussions to the blood flow signal. Hence, we see a decrease in error with increasing angle and a decrease in error for increasing flow-rate.

Additionally, when considering flow-rate, the mean bias and mean standard deviation (in $cm \cdot s^{-1}$) on the lateral component increase with increasing flow. By normalizing these values by the maximum lateral velocity for each flow-rate (refer to figure 5.22), we see that, indeed, the increase represents the same percentage of the maximum velocity, i.e. the variability in the flow is proportional to the maximum velocity.

Due to the limits of the variable speed pump used for experimentation, lower flow-rates, below 0.350 $L \cdot min^{-1}$, were unattainable. Measurements from the low-flow magnetic flow-meter showed inconsistencies and fluctuations when the variable speed pump was set lower than the mentioned threshold. Therefore, three flow-rate levels were chosen above this minimum level, yet within the range of physiological flow-rates in the carotid arteries.

Similarly, the axial velocities, which should be zero, show higher standard deviation and bias for higher flows. A likely cause for such an effect is also due to the increase in maximum velocity; if there exists a larger discrepancy between positive and negative Doppler angled measures at a certain position, the axial component (V_z) will in turn have larger variability.

As a side note, experimental considerations were made to create a fully developed parabolic flow profile. In prospective studies, it would beneficial to test the sensitivity of the estimation procedure by varying the entrance length of the tube before the area of interrogation to examine different flow profiles.

To help decrease the large potential variability in the data, standard post-processing of conventional colour-Doppler data includes spatial and temporal averaging to improve the images by dealing with signal drop out and rapid fluctuations [81]. Hence, applying a robust, efficient and user-independent method of regularization [80], which is extendable to deal with multi-dimensional data for the case of both spatial and temporal smoothing, we improved the estimate by reducing the effect of noise and outlying values which can adversely affect the outcome. Furthermore, although regularization subdues the majority of the small non-zero vectors in the presumed zero-velocity background, a statement should be made to attribute some of the small deviations to spectral broadening (discussed in section 2.2.2).

Since the autocorrelation method of estimation [33], provides the mean velocity at each gated position, clutter signals may have a large effect in reducing the velocity estimate. This may be a major factor contributing to the consistent underestimation bias seen on the lateral velocity profile, indicated by the negative sign and typically most visible at the peak of the velocity profile. By increasing the clutter cut-off frequency the higher velocity components should improve. However, increasing the clutter frequency also compromises the integrity of the lower velocity estimates because important low frequency information starts to be removed from the signal [81]. This point was mentioned prior, for lower flow-rates and beam-to-flow angles closer to 90°.

Perhaps another subtle factor contributing to the underestimation in the velocity profile is due to the use of the emitted central frequency, rather than the true received central frequency, during down-mixing (see section 2.2.3). The autocorrelation estimation method requires that the frequency spectrum be shifted to baseband, which is conventionally done using the emitted central frequency. However, the emitted central frequency is only an approximation of the receive central frequency due to the effects of scattering and frequency dependent attenuation (considered in section 1.1.2), which affect the higher frequency content preeminently, implicitly lowering the received central frequency [81]. Therefore,

down-mixing by the emitted frequency may shift the spectrum marginally too far in the negative direction. If attention is paid to the profiles of the axial estimates on either side of the flow region where the velocity should be zero, the mean estimate is lightly biased in the negative direction.

A confounding effect due to experimentation, apparent in each of the acquisitions, is the degree of overestimation in the lateral velocity component between 2 and 3 cm in depth outside the flow region. These erroneous vector components may be caused by artefactual echoes occurring during experimentation which vary between sets of results. The data collected to compare the effect of the number of tilts per image (N) and the ensemble length (K), were acquired together (within a brief period of time with consistent experimental conditions). The data collected to compare the number of cycles per pulse were collected all at once; however, independently of the previous data.

Lastly, the data concerning variations in acquisition angle (β) and flow-rate were also acquired as a group in a brief period of time with identical experimental conditions. Accountability for the discrepancy in the degree of overestimation in the aberrant region, between but not among comparisons, may be related to the physical position of the ultrasound probe over the scanning medium. Accordingly, further investigation should be made to determine the extent and susceptibility of this method to such errors.

Some additional limitations to this study exist; primarily, due to the decreased penetration depth of plane-wave imaging compared with the conventional focused approach, imaging deep vasculature is not ideal. As previously stated, this method is relevant when applied to more superficial vessels such as the carotid arteries. Moreover, the use of a 128 element linear array transducer makes imaging flow in the heart infeasible due to geometric considerations, as the imaging window is limited to the intercostal region.

A final consideration is the major limitation that the low beam-to-flow angle poses on the reconstruction, demonstrated in section 5.3. Since the vessel orientation

may vary unpredictably, one solution would be to use more than two imaging angles to ensure that at least two emissions capture non-orthogonal components. However, this comes at the expense of decreased frame-rate and adding higher computational cost.

Future perspective of this project involves implementing the methodology on pulsatile flow conditions *in vitro*. Using controlled conditions to mimic physiological blood dynamics over the cardiac cycle, the accuracy of the vector flow mapping can be evaluated on more complex flow.

Conclusion

Plane-wave imaging presents a promising new direction for blood flow analysis. By applying conventional colour-Doppler post-processing to plane-wave acquisitions, the temporal resolution can be improved by frame-rates roughly 10 to 20 times faster, allowing more flexibility in the imaging protocol, without compromising the measurement accuracy.

Decreasing the time between frames, by eliminating the focused beam approach, enables the opportunity to capture fast transitory events which may be missed with conventional frame-rates. Additionally, increasing the pulse repetition frequency increases the maximum/minimum velocity limits, and prevents aliasing in faster flow areas. As a result, the acquisition time is reduced for a given ensemble length, which may better accommodate the short cardiac cycle.

On the other hand, to avoid Doppler signal truncation which limits the minimum attainable velocities, the ensemble length may also be increased to allow for better velocity estimates over the full range. Increasing the frame-rate also allows more time for two-dimensional imaging using vector-Doppler without sacrificing the temporal resolution, while maintaining the same estimation performance demonstrated for conventional ultrasound imaging.

Contrary to conventional Doppler, which displays colour coded velocity projections in-line with the beam direction, vector mapping provides a two-dimensional representation in a Cartesian coordinate system. The ability to visualize two-dimensional magnitudes and directions is much more intuitive and easier to comprehend. Moreover, being able to work with the lateral and axial velocity components at each spatial location permits one to calculate other important characteristics of the flow, such as vorticity and circulation, which may indicate the progression of cardiovascular disease.

References

[1] S. Mendis, Puska, P., Norrving, B. , *Global Atlas on Cardiovascular Disease Prevention and Control*: World Health Organization, 2011.

[2] S. C. Smith*, et al.*, "Principles for National and Regional Guidelines on Cardiovascular Disease Prevention: a scientific statement from the World Heart and Stroke Forum," *Circulation Journal of the American Heart Association,* vol. 109, pp. 3112-3121, 2004.

[3] "Mortality, Summary List of Causes", 2009. Statistics Canada, Health Statistics Division, Government of Canada. Released in 2012.

[4] "Tracking heart disease and stroke in Canada", 2009. Public Health Agency of Canada. Released in June 2009.

[5] "The Canadian Heart Health Strategy: Risk Factors and Future Cost Implications", 2010. Conference Board of Canada. Released in February 2010.

[6] A. M. Malek, S. L. Alper, and S. Izumo, "Hemodynamic shear stress and its role in atherosclerosis," *The Journal of the American Medical Association,* vol. 282, p. 2035, 1999.

[7] D. N. Ku, D. P. Giddens, C. K. Zarins, and S. Glagov, "Pulsatile flow and atherosclerosis in the human carotid bifurcation. Positive correlation between plaque locations and low oscillating shear stress," *Arteriosclerosis, Thrombosis, and Vascular Biology,* vol. 5, pp. 293-302, 1985.

[8] K. T. Nguyen, C. D. Clark, T. J. Chancellor, and D. V. Papavassiliou, "Carotid geometry effects on blood flow and on risk for vascular disease," *Journal of Biomechanics,* vol. 41, pp. 11-19, 2008.

[9] F. Forsberg, Z. Morvay, N. M. Rawool, C. R. Deane, and L. Needleman, "Shear rate estimation using a clinical ultrasound scanner," *Journal of Ultrasound in Medicine,* vol. 19, pp. 323-327, 2000.

[10] P. J. Brands, A. Hoeks, L. Hofstra, and R. S. Reneman, "A non-invasive method to estimate wall shear rate using ultrasound," *Ultrasound in Medicine & Biology,* vol. 21, p. 171, 1995.

[11] L. Bohs, B. Geiman, M. Anderson, S. Gebhart, and G. Trahey, "Speckle tracking for multi-dimensional flow estimation," *Ultrasonics,* vol. 38, pp. 369-375, 2000.

[12] J. A. Jensen, "A new estimator for vector velocity estimation," *IEEE Transactions on Ultrasonics Ferroelectrics, and Frequency Control,* vol. 48, pp. 886-894, 2001.

[13] M. Scabia, M. Calzolai, L. Capineri, L. Masotti, and A. Fort, "A real-time two-dimensional pulsed-wave Doppler system," *Ultrasound in Medicine & Biology,* vol. 26, pp. 121-131, 2000.

[14] M. Arigovindan, M. Suhling, C. Jansen, P. Hunziker, and M. Unser, "Full motion and flow field recovery from echo Doppler data," *IEEE Transactions on Medical Imaging,* vol. 26, pp. 31-45, 2007.

[15] J. A. Jensen, *Estimation of blood velocities using ultrasound: a signal processing approach*. Cambridge: University Press, 1996.

[16] D. H. Evans, W. N. McDickens, R. Skidmore, and J. P. Woodcock, *Doppler ultrasound: physics, instrumentation, and clinical applications*: John Wiley & Sons, 1991.

[17] J. Udesen*, et al.*, "High frame-rate blood vector velocity imaging using plane waves: simulations and preliminary experiments," *IEEE Transactions on Ultrasonics Ferroelectrics, and Frequency Control,* vol. 55, pp. 1729-1743, 2008.

[18] J. Bercoff*, et al.*, "Ultrafast compound Doppler imaging: providing full blood flow characterization," *IEEE Transactions on Ultrasonics Ferroelectrics, and Frequency Control,* vol. 58, pp. 134-147, 2011.

[19] I. K. Ekroll*, et al.*, "Simultaneous quantification of flow and tissue velocities based on multi-angle plane wave imaging," *IEEE Transactions on Ultrasonics Ferroelectrics, and Frequency Control,* vol. 60, pp. 727-738, 2013.

[20] Vault. (2012). *Educational Resources: Principles of Sound*. Virginia Ultrasound. Available: http://www.vaultrasound.com/educational-resources/ultrasound-physics/sound-basics/

[21] K. K. Shung, *Diagnostic Ultrasound*: CRC Press, Taylor Francis Group, 2006.

[22] D. H. Evans and W. N. McDickens, *Doppler ultrasound: physics, instrumentation and signal processing*, Second ed. New York: John Wiley & Sons, 2000.

[23] J. T. Bushberg, J. A. Seibert, E. M. Leidholdt, and J. M. Boone, "Ultrasound," in *The Essential Physics of Medical Imaging*, Lippincott Williams & Wilkins, Ed., 2nd ed, 2001, pp. 469-553.

[24] W. R. Hendee and E. R. Ritenour, "Ultrasound Transducers," in *Medical Imaging Physics*, Fourth ed: John Wiley & Sons, Inc., 2003, pp. 317-330.

[25] A. Swillens, "A Multiphysics Model for Improving the Ultrasonic Assessment of Large Arteries," Doctoral Thesis, University of Gent, Belgium, 2010.

[26] L. Løvstakken, "Signal Processing in Diagnostic Ultrasound: Algorithms for Real-time Estimation and Visualization of Blood Flow Velocity," Doctoral Thesis, Norwegian University of Science and Technology, Norway, 2007.

[27] D. Lines and J. Wharrie. (2011). *Using NI FlexRIO for Ultrasound Array Imaging for Nondestructive Testing*. Quality Digest Magazine. Available: http://www.qualitydigest.com/inside/metrology-article/using-ni-flexrio-ultrasound-array-imaging-nondestructive-testing.html#

[28] (2013). *Carotid Ultrasound Imaging*. Radiological Society of North America, Inc. Available: http://www.radiologyinfo.org/en/photocat/gallery3.cfm?image=carotid-dopus3.jpg&pg=us-carotid

[29] V. Newhouse, W. Varner, and P. Bendick, "Geometrical spectrum broadening in ultrasonic Doppler systems," *IEEE Transactions on Biomedical Engineering,* vol. 24, pp. 478-480, 1977.

[30] J. Kirkhorn. (1999). *Introduction to IQ-Demodulation of RF-Data*. Available: http://folk.ntnu.no/htorp/Undervisning/TTK4165/notater/IQdemodulation.pdf

[31] J.-J. Ding, "Time-frequency analysis for Doppler ultrasound signals," unpublished. Available: http://djj.ee.ntu.edu.tw/

[32] J. A. Jensen and P. Munk, "A new method for estimation of velocity vectors," *IEEE Transactions on Ultrasonics, Ferroelectrics, and Frequency Control,* vol. 45, pp. 837-851, 1998.

[33] C. Kasai, K. Namekawa, A. Koyano, and R. Omoto, "Real-time two-dimensional blood flow imaging using an autocorrelation technique," *IEEE Transactions on Sonics and Ultrasonics,* vol. 32, pp. 458-464, 1985.

[34] R. S. C. Cobbold, *Foundations of Biomedical Ultrasound*. New York: Oxford University Press, Inc., 2007.

[35] S. Bjaerum, H. Torp, and K. Kristoffersen, "Clutter filter design for ultrasound color flow imaging," *IEEE Transactions on Ultrasonics Ferroelectrics, and Frequency Control,* vol. 49, pp. 204-216, 2002.

[36] C. Deane. (2002). *Doppler ultrasound: principles and practice*. Available: http://www.centrus.com.br/DiplomaFMF/SeriesFMF/doppler/capitulos-html/chapter_01.htm

[37] A. Stoylen. (2013). *Basic ultrasound, echocardiography and Doppler for clinicians*. Available: http://folk.ntnu.no/stoylen/strainrate/Ultrasound/

[38] C. B. Burckhardt, "Speckle in ultrasound B-mode scans," *IEEE Transactions on Sonics and Ultrasonics,* vol. SU-25, pp. 1-6, 1978.

[39] A. Swillens, P. Segers, H. Torp, and L. Lovstakken, "Two-dimensional blood velocity estimation with ultrasound: speckle tracking versus crossed-beam vector Doppler based on flow simulations in a carotid bifurcation model," *IEEE Transactions on Ultrasonics, Ferroelectrics, and Frequency Control,* vol. 57, pp. 327-339, 2010.

[40] L. N. Bohs, B. J. Geiman, M. E. Anderson, S. C. Gebhart, and G. E. Trahey, "Speckle tracking for multi-dimensional flow estimation," *Ultrasonics* vol. 38, pp. 369-375, 2000.

[41] K. L. Hansen, J. Udesen, F. Gran, J. A. Jensen, and M. B. Nielsen, "Fast blood vector velocity imaging using ultrasound: *In-vivo* examples of complex blood flow in the vascular system," in *IEEE International Ultrasonics Symposium*, 2008.

[42] M. Tanter, J. Bercoff, L. Sandrin, and M. Fink, "Ultrafast compound imaging for 2-D motion vector estimation: application to transient elastography," *IEEE Transactions on Ultrasonics Ferroelectrics, and Frequency Control,* vol. 49, pp. 1363-1374, 2002.

[43] G. E. Trahey, S. M. Hubbard, and O. T. vonRamm, "Angle independent ultrasonic blood flow detection by frame-to-frame correlation of B-mode images," *Ultrasonics,* vol. 26, pp. 271-276, 1988.

[44] L. N. Bohs and G. E. Trahey, "A novel method for angle independent ultrasonic imaging of blood flow and tissue motion," *IEEE Transactions on Biomedical Engineering,* vol. 38, pp. 280-286, 1991.

[45] J. Udesen and J. A. Jensen, "Investigation of transverse oscillation method," *IEEE Transactions on Ultrasonics Ferroelectrics, and Frequency Control,* vol. 53, pp. 959-971, 2006.

[46] M. J. Pihl, "3D vector flow imaging," Doctoral Thesis, Department of Electrical Engineering, Technical University of Denmark, Denmark, 2012.

[47] J. Udesen and J. Arendt Jensen, "Experimental investigation of transverse flow estimation using transverse oscillation," in *Ultrasonics, 2003 IEEE Symposium on*, 2003, pp. 1586-1589.

[48] K. L. Hansen, J. Udesen, C. Thomsen, J. A. Jensen, and M. B. Nielsen, "*In vivo* validation of a blood vector velocity estimator with MR Angiography," *IEEE Transactions on Ultrasonics Ferroelectrics, and Frequency Control,* vol. 56, pp. 91-100, 2009.

[49] E. Schrank, D. J. Phillips, W. E. Moritz, and D. E. Strandness, "A triangulation method for the quantitative measurement of arterial blood velocity magnitude and direction in humans," *Ultrasound in Medicine & Biology,* vol. 16, pp. 499-509, 1990.

[50] P. A. Picot, R. Daniel W. RickeyMitchell, R. N. Rankin, and A. Fenster, "Three-dimensional colour Doppler imaging," *Ultrasound in Medicine & Biology,* vol. 19, pp. 95-104, 1993.

[51] S. Xu, H. Ermert, and R. Hammentgen, "Phased array pulse Doppler tomography," in *IEEE Ultrasonics Symposium*, 1991, pp. 1273-1276.

[52] B. Dunmire, K. W. Beach, L.-H. Labs, M. Plett, and D. E. Strandness, "Cross-beam vector Doppler ultrasound for angle-independent velocity measurements," *Ultrasound in Medicine & Biology,* vol. 26, pp. 1213-1235, 2000.

[53] T. Tamura, R. S. C. Cobbold, and K. W. Johnston, "Determination of 2-D velocity vectors using color Doppler ultrasound," in *IEEE Ultrasonics Symposium*, 1990, pp. 1537-1540.

[54] P. J. Phillips, A. P. Kadi, and O. T. v. Ramm, "Feasibility study for a two-dimensional diagnostic ultrasound velocity mapping system," *Ultrasound in Medicine & Biology,* vol. 21, pp. 217-229, 1995.

[55] S. Dort, J. Hamel-Nunes, G. Soulez, S. Lerouge, and D. Garcia, "Vector field reconstruction from echo-Doppler data using a DCT-based penalized least squares method," in *World Congress on Medical Physics and Biomedical Engineering*, Munich, Germany, September 2009.

[56] J. A. Jensen and I. R. Lacasa, "Estimation of blood velocity vectors using transverse ultrasound beam focusing and cross-correlation," in *IEEE Ultrasonics Symposium* 1999, pp. 1493-1497.

[57] J. A. Jensen, "Field: A Program for Simulating Ultrasound Systems," *Paper presented at the 10th Nordic-Baltic Conference on Biomedical Imaging Published in Medical & Biological Engineering & Computing,* vol. 34, pp. 351-353, 1996.

[58] O. D. Kripfgans, J. M. Rubin, A. L. Hall, and J. B. Fowlkes, "Vector Doppler imaging of a spinning disc ultrasound Doppler phantom," *Ultrasound in Medicine & Biology,* vol. 32, pp. 1037-1046, 2006.

[59] R. Z. Azar, A. Baghani, S. E. Salcudean, and R. Rohling, "2-D high-frame-rate dynamic elastography using delay compensated and angularly compounded motion vectors: preliminary results," *IEEE Transactions on Ultrasonics, Ferroelectrics, and Frequency Control,* vol. 57, pp. 2421-2436, 2010.

[60] T. G. Bjastad, "High frame rate ultrasound imaging using parallel beamforming," Doctoral Thesis, Department of Circulation and Medical Imaging, Norwegian University of Science and Technology, Trondheim, Norway, 2009.

[61] D. P. Shattuck, M. D. Weinshenker, S. W. Smith, and O. T. v. Ramm, "Explososcan: A parallel processing technique for high speed ultrasound imaging with linear phased arrays," in *Medical Imaging Conferences*, 1985, pp. 247-260.

[62] L. N. Bohs, B. J. Geiman, M. E. Anderson, S. M. Breit, and G. E. Trahey, "Ensemble tracking for 2D vector velocity measurement: experimental and initial clinical results," *Ultrasonics, Ferroelectrics and Frequency Control, IEEE Transactions on,* vol. 45, pp. 912-924, 1998.

[63] L. N. Bohs, S. C. Gebhart, M. E. Anderson, B. J. Geiman, and G. E. Trahey, "2-D motion estimation using two parallel receive beams," *Ultrasonics, Ferroelectrics and Frequency Control, IEEE Transactions on,* vol. 48, pp. 392-408, 2001.

[64] D. Garcia*, et al.*, "Stolt's *f-k* migration for plane wave ultrasound imaging," *IEEE Transactions on Ultrasonics Ferroelectrics, and Frequency Control,* vol. 60, pp. 1853-1867, 2013.

[65] G. F. Margrave, "Elementary Migration Methods," in *Numerical Methods of Exploration Seismology with Algorithms in MATLAB*, The University of Calgary Department of Geology and Geophysics, Ed., ed, 2001.

[66] J. Y. Lu, "2D and 3D high frame rate imaging with limited diffraction beams," *IEEE Transactions on Ultrasonics Ferroelectrics, and Frequency Control,* vol. 44, pp. 839-856, 1997.

[67] G. Montaldo, M. Tanter, J. Bercoff, N. Benech, and M. Fink, "Coherent plane-wave compounding for very high frame rate ultrasonography and transient elastography," *IEEE Transactions on Ultrasonics Ferroelectrics, and Frequency Control,* vol. 56, pp. 489-506, 2009.

[68] I. K. Holfort, F. Gran, and J. A. Jensen, "Plane wave medical ultrasound imaging using adaptive beamforming," in *IEEE Sensor Array and Multichannel Signal Processing*, 2008.

[69] K. Ferrara and G. DeAngelis, "Color flow mapping," *Ultrasound in Medicine & Biology,* vol. 23, pp. 321-345, 1997.

[70] A. M. Shaaban and A. J. Duerinckx, "Wall shear stress and early artherosclerosis: A review," *American Journal of Radiology,* vol. 174, 2000.

[71] S. I. Rabben*, et al.*, "An ultrasound-based method for determining pulse wave velocity in superficial arteries," *Journal of Biomechanics,* vol. 37, pp. 1615-1622, 2004.

[72] A. Swillens, T. D. Schryver, L. Lovstakken, H. Torp, and P. Segers, "Assessment of numerical simulation strategies for ultrasonic color blood flow imaging, based on a computer and experimental model of the carotid artery," *Annals of Biomedical Engineering* vol. 37, pp. 2188-2199, 2009.

[73] B. M. Eicke*, et al.*, "Lack of association between carotid artery volume blood flow and cardiac output," *Journal of Ultrasound in Medicine,* vol. 20, pp. 1293-1298, 2001.

[74] P. Bendel, E. Buonocore, A. Bockisch, and M. C. Besozzi, "Blood flow in the carotid arteries: quantification by using phase-sensitive MR imaging," *American Journal of Radiology,* vol. 152, pp. 1307-1310, 1989.

[75] H. G. Bogren, M. H. Buonocore, and W. Z. Gu, "Carotid and vertebral artery blood flow in left-and right-handed healthy subjects measured with MR velocity mapping," *Journal of Magnetic Resonance Imaging,* vol. 4, pp. 37-42, 1994.

[76] R. L. Levine, P. A. Turski, K. A. Holmes, and T. M. Grist, "Comparison of magnetic resonance volume flow rates, angiography, and carotid Dopplers. Preliminary results," *Stroke,* vol. 25, pp. 413-417, 1994.

[77] T. Loupas, R. B. Peterson, and R. W. Gill, "Experimental evaluation of velocity and power estimation for ultrasound blood flow imaging, by means of a two-dimensional autocorrelation approach," *IEEE Transactions on Ultrasonics, Ferroelectrics, and Frequency Control,* vol. 42, pp. 689-699, 1995.

[78] B. Beulen, N. Bijnens, M. Rutten, P. Brands, and F. v. d. Vosse, "Perpendicular ultrasound velocity measurement by 2D cross correlation of RF data. Part B: volume flow estimation in curved vessels," *Experiments in Fluids,* vol. 49, pp. 1219-1229, 2010.

[79] E. Mace*, et al.*, "Functional ultrasound imaging of the brain," *Nature Methods,* vol. 8, pp. 662-666, 2011.

[80] D. Garcia, "Robust smoothing of gridded data in one and higher dimensions with missing values," *Computational Statistics & Data Analysis,* vol. 54, pp. 1167-1178, 2010.

[81] D. H. Evans, J. A. Jensen, and M. B. Nielsen, "Ultrasonic colour Doppler imaging," *Interface Focus,* vol. 1, pp. 490-502, 2011.

Appendix 1

Delay-and-Sum Method (DAS): rectifying plane-wave hyperbolas

The DAS method makes use of calculated travel times to correct the hyperbolic diffraction patterns of raw plane-wave data. In order to extract the correct location and amplitude of the scatterers in the medium for visualization, the contributions of all elements to an echo arising from a particular point (x', z') are summed. The travel-times, in transmit and receive, correspond to the time taken for the plane-wave wave-front to reach a scatterer and for the spherical echo to return to the transducer. As a visual aid, the delays in transmit and reception are displayed in figures A.1 and A.2.

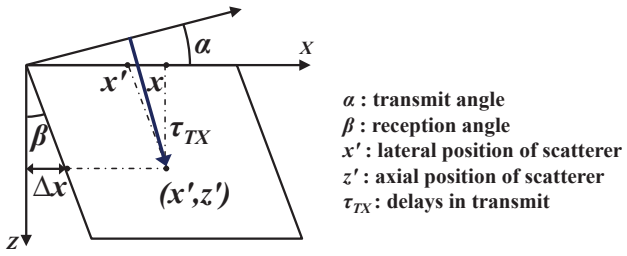

Figure A.1: The travel times in transmit for plane-wave imaging in an oriented coordinate system. The blue arrow represents the travel time required in transmission, τ_{TX}, to reach a particular point (x', z') for a given transmit angle, α, in an oriented basis defined by the receive angle β . Modified from Montaldo et al. (2009).

From figure A.1, the following trigonometric relationships (A.1-A.3) can be established,

$$z = z' \cdot \cos\beta \qquad \text{A.1}$$

$$\Delta x = z' \cdot \sin\beta \qquad \text{A.2}$$

$$x = x' + z' \cdot \sin\beta \qquad \text{A.3}$$

where x and z give the lateral and axial location in a regular Cartesian base, x' and z' give the lateral and axial location in an oriented coordinate system, and Δx is the axial distance between x and x' which varies with axial position and angle of reception. The transmit angle is α and the angle of reception, denoted by β, defines the orientation of the coordinate system.

The travel-time in transmit, τ_{TX}, can be calculated by,

$$\tau_{TX} = \frac{z \cdot \cos\alpha + x \cdot \sin\alpha}{c} \quad , \qquad \text{A.4}$$

where α is the transmit angle and c is the acoustic speed. Using the former three trigonometric relations the transmit travel-time becomes,

$$\tau_{TX} = \frac{z' \cdot \cos\alpha \cdot \cos\beta + x' \cdot \sin\alpha + z' \sin\alpha \cdot \sin\beta}{c} \quad . \qquad \text{A.5}$$

By simplifying (A.5) using the *product-to-sum* trigonometric identities $\cos\varphi \cdot \cos\gamma = \frac{1}{2}\cos(\phi - \gamma) + \cos(\phi + \gamma)$ and $\sin\varphi \cdot \sin\gamma = \frac{1}{2}\cos(\phi - \gamma) - \cos(\phi + \gamma)$, the final form of the transmit travel-times can be written as

$$\tau_{TX} = \frac{z' \cdot \cos(\alpha - \beta) + x' \cdot \sin\alpha}{c} \quad . \qquad \text{A.6}$$

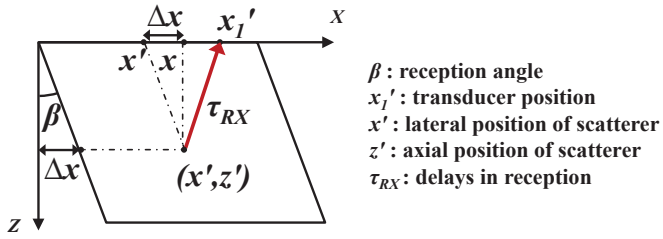

Figure A.2: The travel times in reception for plane-wave imaging in an oriented coordinate system. The red arrow represents the travel time required in reception, τ_{RX}, to return from a particular point (x', z') in an oriented basis defined by the receive angle β. Modified from Montaldo et al. (2009).

From figure A.2, the travel-times in reception τ_{RX} can be expressed as

$$\tau_{RX} = \frac{\sqrt{(x_1' - x)^2 + z^2}}{c} \quad , \qquad \text{A.7}$$

where x_1' defines the lateral location of a particular receiving element. Again using (A.1), (A.2), and (A.3), the travel-time in reception can be written as a function of the oriented coordinates and receive angle as follows,

$$\tau_{RX} = \frac{\sqrt{\left((x_1' - x') - z' \cdot \sin\beta\right)^2 + \left(z' \cdot \cos\beta\right)^2}}{c} \quad . \qquad \text{A.8}$$

By simplifying, we arrive at the expression

$$\tau_{RX} = \frac{\sqrt{z'^2 + (x_1' - x')^2 - z' \cdot (x_1' - x') \cdot 2\sin\beta}}{c} \quad . \qquad \text{A.9}$$

The total travel-time τ in transmission and reception is given by $\tau = \tau_{TX} + \tau_{RX}$.

Appendix 2

Vector-Doppler: axial and lateral velocity components

A dual angle cross-beam acquisition scheme is shown below, figure A.3 panel A. The unit vector components $\vec{e}_p$ and $\vec{e}_n$ in panel B show the orientation of the 1D positional velocity vectors projections V_p and V_n, in line with the transducer beam, for positively and negatively oriented images. The orientation of the acquisitions makes an angle β with the vertical axis.

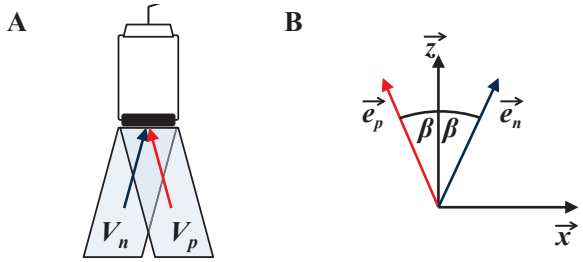

Figure A.3: Panel A shows the convention of the dual angle VD acquisitions. The components of the negatively and positively oriented scans are marked in blue and red. Panel B gives the unit vector components in transducer based coordinates represented in a common Cartesian coordinate system.

The goal is to define the velocity vectors in a common Cartesian coordinate system x-z, to allow a 2D perspective of the flow for each position in the velocity field. The vectors $\vec{e}_p$ and $\vec{e}_n$ can be broken down into $\vec{x}$ and $\vec{z}$ vector components as shown using the following two equations,

$$\vec{e}_n = \sin\beta \cdot \vec{x} + \cos\beta \cdot \vec{z} \qquad \text{A.10}$$

$$\vec{e}_p = -\sin\beta \cdot \vec{x} + \cos\beta \cdot \vec{z} \qquad \text{A.11}$$

Next the total velocity, V, is the vector sum of the x and z-velocities,

$$V = V_x\vec{x} + V_z\vec{z} \qquad \text{A.12}$$

Using (A.10), (A.11) and (A.12), the transducer based velocity components can be represented in terms of V_x and V_z for both negative (A.13) and positive (A.14) angled images.

$$V_n = \left[V_x \vec{x} + V_z \vec{z}\right] \cdot \left[\sin\beta \cdot \vec{x} + \cos\beta \cdot \vec{z}\right] \quad \text{A.13}$$

$$V_p = \left[V_x \vec{x} + V_z \vec{z}\right] \cdot \left[-\sin\beta \cdot \vec{x} + \cos\beta \cdot \vec{z}\right] \quad \text{A.14}$$

By simplifying (A.13) and (A.14) we have,

$$V_n = V_x \cdot \sin\beta + V_z \cdot \cos\beta \quad \text{A.15}$$

$$V_p = -V_x \cdot \sin\beta + V_z \cdot \cos\beta \quad \text{A.16}$$

which can be reformulated in matrix form as follows,

$$\begin{bmatrix} V_n \\ V_p \end{bmatrix} = \begin{bmatrix} \sin\beta & \cos\beta \\ -\sin\beta & \cos\beta \end{bmatrix} \cdot \begin{bmatrix} V_x \\ V_z \end{bmatrix} \quad \text{A.17}$$

Knowing that $A^{-1}A = I$, we can solve for V_x and V_z,

$$\begin{bmatrix} V_x \\ V_z \end{bmatrix} = \frac{1}{2\sin\beta\cos\beta} \begin{bmatrix} \cos\beta & -\cos\beta \\ \sin\beta & \sin\beta \end{bmatrix} \cdot \begin{bmatrix} V_n \\ V_p \end{bmatrix} \quad \text{A.18}$$

and simplify, yet again, to obtain,

$$\begin{bmatrix} V_x \\ V_z \end{bmatrix} = \frac{1}{2} \begin{bmatrix} 1/\sin\beta & -1/\sin\beta \\ 1/\cos\beta & 1/\cos\beta \end{bmatrix} \begin{bmatrix} V_n \\ V_p \end{bmatrix} \quad \text{A.19}$$

The final result is shown here, in (A.20) and (A.21),

$$V_x = \frac{V_n - V_p}{2\sin\beta} \quad \text{A.20}$$

$$V_z = \frac{V_n + V_p}{2\cos\beta} \quad \text{A.21}$$

which provide the 2D velocity components in a common X-Z coordinate system.